5-2014

Understanding the Plasmonic Properties of Metallic Nanostructures with Correlated Photon- and Electron-Driven Excitations

Vighter Ozezinimize Iberi
University of Tennessee - Knoxville, viberi@utk.edu

To the Graduate Council:

I am submitting herewith a dissertation written by Vighter Ozezinimize Iberi entitled "Understanding the Plasmonic Properties of Metallic Nanostructures with Correlated Photon- and Electron-Driven Excitations." I have examined the final electronic copy of this dissertation for form and content and recommend that it be accepted in partial fulfillment of the requirements for the degree of Doctor of Philosophy, with a major in Chemistry.

Jon P. Camden, Major Professor

We have read this dissertation and recommend its acceptance:

Michael D. Best, Robert N. Compton, David C. Joy

Accepted for the Council:

Carolyn R. Hodges

Vice Provost and Dean of the Graduate School

(Original signatures are on file with official student records.)

Understanding the Plasmonic Properties of Metallic Nanostructures with Correlated Photon- and Electron-Driven Excitations

A Dissertation Presented for the

Doctor of Philosophy

Degree

The University of Tennessee, Knoxville

Vighter Ozezinimize Iberi

May 2014

DEDICATION

This dissertation is dedicated to God, the origin of all wisdom and knowledge. It is dedicated also to my parents, Mr. Vighter Iberi Snr. and Mrs. Florence Iberi, my brothers, Chuks and Kiyinne, and my sisters, Faith and Blessing.

In loving memory of Mrs. Bernadine Mbata, may perpetual light continue to shine upon you and all the faithful departed.

ACKNOWLEDGEMENTS

My deepest gratitude goes to my advisor, Prof. Jon Camden, for his invaluable support throughout the course of my graduate studies. Special thanks also go to the following people: Dr. Stephen Pennycook, Prof. Beth Guiton, Prof. Robert Compton, Prof. Michael Best and Prof. David Joy for all their academic guidance and support. Many thanks to Prof. David Masiello, Nicholas Bigelow, Alex Vaschillo, Prof. Shuzhou Li, and Prof. George Schatz for all their significant theoretical contributions. To my colleagues in the Camden Group, both former and current, thank you for your tremendous support and encouragement. I wish to thankfully acknowledge the financial support of the U.S. Department of Energy (DOE), Office of Basic Energy Sciences (BES) under award numbers DE-SC0004792 and DE-SC0010536.

I remain eternally grateful to Angela Kuzma, Ann Brown, Rev. Fr. James Bromwich, Rev. Fr. Thomas McDermott, O.P., Dr. and Mrs. Adcock, “Grandma” Theo Stearns and other members of the Dominican Community in New Hope KY, for their unwavering support throughout my academic career in the USA. Also, a special appreciation goes to *Ihunanyam*, Ihunanya Mbata, for all her love and support.

ABSTRACT

The collective oscillation of the conduction band electrons in metal nanostructures, known as *plasmons*, can be used to manipulate light on length scales that are smaller than the diffraction limit of visible light. In this dissertation, a correlated approach is used to probe localized surface plasmon resonances (LSPRs) in metallic nanostructures, and their application to surface-enhanced spectroscopy. This correlated approach involves the measurement of LSPRs with dark-field optical microscopy (resonance-Rayleigh scattering), and electron energy-loss spectroscopy (EELS) in a scanning transmission electron microscope (STEM). Structural parameters of the exact same nanostructures obtained from the STEM are subsequently used in performing fully three-dimensional continuum electrodynamics simulations to support the experimental observables.

The first part of this work utilizes the correlated approach with theoretically calculated near-electric field enhancements, in exploring the LSPRs of silver nanorods with varying aspect-ratios. Multivariate statistical analysis (MVSA) is used to extract the experimentally measured plasmon modes obtained from STEM/EELS, with a spatial resolution on the length scale of the plasmon itself. These results demonstrate the ability of the correlated approach to yield complementary information not accessible from either technique on its own. In the second study, the *electromagnetic hot spots* responsible for single-molecule surface-enhanced Raman scattering (SMSERS) are investigated with the correlated approach and theoretical simulations. The results suggest the possibility of exciting a hot spot with an electron beam, and inducing

Raman scattering from a single molecule when the beam is positioned antisymmetrically with respect to the hot spot. The third and final part of this work investigates Fano resonances in silver nanocubes with STEM/EELS, and the changes that occur in the LSPR spectra of nanocubes after exposure to the electron beam. The results from this study suggest that the hybridized modes responsible for Fano interference in STEM/EELS are the same as those present in optical spectroscopy.

TABLE OF CONTENTS

LIST OF FIGURES

INTRODUCTION

Statement of Purpose

The emergence of STEM/EELS as an unprecedented technique capable of mapping the plasmonic properties in metallic nanostructures on length scales 100 times smaller than optical wavelengths (~1 nm) has revolutionized the field of fundamental and applied plasmonics. Despite the great potential that is associated with using this technique, the connection between electron-driven plasmons, encountered in EELS, and optically-driven plasmons, encountered in plasmonic devices, is still not well understood. Moreover, the direct and routine imaging of optically-driven plasmons still remains a significant challenge.

The work presented here focuses on correlating optical spectroscopy (resonance-Rayleigh scattering) and electron microscopy from the exact same nanostructures. The approach is twofold: (1) Imaging plasmon modes in single nanoparticle structures as well as nanoparticle aggregates, and correlating these measurements with resonance-Rayleigh scattering measurements and fully three-dimensional electrodynamics simulations. (2) Directly imaging the plasmons that give rise to surface-enhanced Raman scattering in molecules and establishing the location of the molecule relative to the plasmons which underlie these optical scattering spectroscopies.

Literature Background

Localized Surface Plasmon Resonance (LSPR)

The phenomenon of localized surface plasmon resonance (LSPR) in nature can be traced as far back as the advent of stained glass windows that were used in churches. The bright colors that were observed came as a result of the interaction of light with the silver and gold nanoparticles embedded in the glass. In the 19th century, Michael Faraday conducted some experiments to investigate how light interacted with gold particles of various sizes,[1] while in the 1950s, Ritchie laid the foundations for the application of surface plasmons to the field of surface science in his pioneering work. Localized surface plasmon resonances result from the collective oscillations of the conduction band electrons in small metallic nanoparticles. Figure 1 gives a schematic representation of the oscillation induced by the interaction of a time-varying electric with metal sphere.

In 1908, Mie solved the Maxwell's equations that describe the absorption and scattering of spherical particles of arbitrary sizes.[2] In metallic nanoparticles, LSPRs are responsible for the observed extinction (absorption plus scattering) spectra. Numerous studies have shown that the positions of the LSPR spectra are dependent on the size, shape and local dielectric environment of the nanoparticle.[3] These metallic nanoparticles are usually of the order $d << \lambda$ where d is the size of the nanoparticle and λ is the wavelength of the incident radiation. The criterion, $d << \lambda$, enhances the use of local surface plasmon resonance to concentrate light in metallic nanoparticles and it stems from the different (relative) permittivities, ε, of the metal and the surrounding

dielectric media. When light is concentrated in this manner, there is an enhancement in the electric field which can be used to manipulate spectroscopy and other non-linear phenomena. This criterion is also responsible for the intense signal enhancement observed in surface-enhanced Raman spectroscopy (SERS),[4] more recently, single-molecule surface-enhanced Raman spectroscopy (SMSERS),[5-6] which will be discussed in greater detail. Other applications of LSPRs include optical chemical sensing,[7] plasmonic solar cells,[8] biomedicine,[9] and plasmonic waveguiding.[10-11]

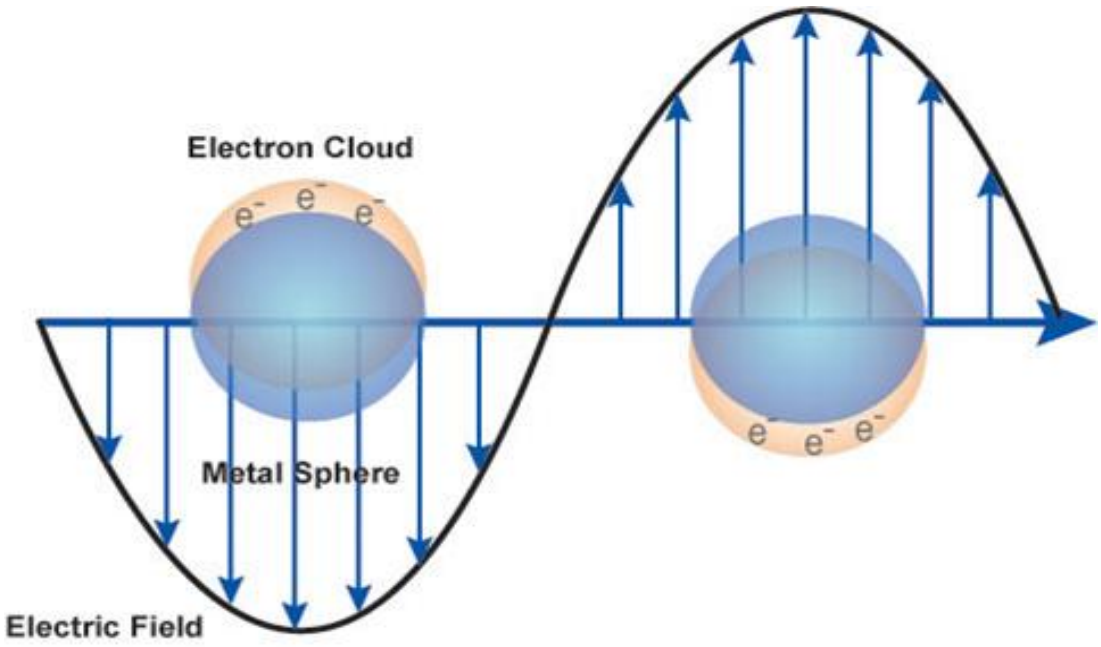

Figure 1. Schematic diagram of the plasmon excitation for a sphere showing the displacement of the conduction electron charge relative to the nuclei.

Plasmon Imaging Techniques

In the last ten years, the number of methods available for manufacturing metallic nanoparticles has greatly expanded. Nonspherical particles have been developed using wet chemistry techniques and have yielded particles such as rods,[12] triangles,[13] and cubes.[14] Other methods such as nanosphere lithography (NSL)[15] and e-beam lithography (EBL)[16] have also been developed. The optical properties of these metallic nanoparticles are usually characterized using spectroscopic methods such as near-field scanning optical microscopy (NSOM),[17-20] photon scanning tunneling microscopy (PSTM),[21] photoemission,[22] and dark-field illumination.[23] However, these spectroscopic methods are diffraction-limited and are not capable of providing the desired nanoscale spatial resolution of LSPR modes within a single nanoparticle. Plasmon imaging in NSOM is limited to spatial resolutions of about 10 nm which is too large for imaging very confined LSPRs. State-of-the-art NSOM experiments have demonstrated spatial resolutions on the order of 15 nm[24] but require the fabrication of very sharp tips[25] which can be very difficult.

The limitations in imaging plasmon modes in metallic nanoparticles can be easily overcome with electron energy-loss spectroscopy (EELS) in a scanning transmission electron microscope (STEM). For many years, the study of bulk plasmon losses in thin metallic films[26] and clusters[27] has been done using this method but it was only fairly recently that the extraction of information from the low energy region of the spectrum became possible. The advent of monochromated electron beams and improved energy resolution has enabled the characterization of LSPRs in metallic nanostructures with

energies as low as 1 eV.[28] In EELS, a monoenergetic beam of electrons is exposed to a material and analyzed after the material has interacted with the electron beam. The electric field associated with a swift electron interacting with the metallic nanostructure leads to the displacement of the conduction electrons in the material. These conduction electrons undergo collective oscillations at their natural plasmon frequency while the fast-moving electron loses energy which corresponds to the plasmon energy.[29] The scattered electron beam is then collected and analyzed with a spectrometer which displays the energy distribution corresponding to the exchange of energy between the incident electron beam and the metallic nanostructure.

Surface-Enhanced Raman Spectroscopy (SERS) and Single-Molecule SERS

The phenomenon of surface-enhanced Raman spectroscopy (SERS) was first observed by Fleischman et al. in 1974,[30] and discovered independently by Jeanmaire and Van Duyne[4] and Albrecht and Creighton[31] in 1977. When it was first observed for pyridine adsorbed on an electrochemically roughed silver electrode, the unusual intensity of the Raman signals was attributed to the increased surface area of the roughened substrate. In 1978, Moskovits attributed the huge increase in the Raman cross-section to the excitation of surface plasmons[32] and it now provides the framework for understanding the bulk of the SERS effect. Two mechanisms of enhancement are usually ascribed to SERS; an electromagnetic enhancement and a chemical enhancement. These two mechanisms are related to the induced dipole moment by the equation:

$$\boldsymbol{\mu} = \alpha \mathbf{E}$$

where $\boldsymbol{\mu}$ is the dipole moment of the molecule, α the molecular polarizability, and $\mathbf{E}$ is the applied electric field. The chemical enhancement is usually governed by the modification of the molecular polarizability α, while the electromagnetic mechanism is governed by the adjustment of the applied electric field $\mathbf{E}$. However, it has been predicted that the chemical enhancement contributes about 3-4 orders of magnitude to the Raman signal of molecules on some metallic surfaces[33] while the electromagnetic enhancement contributes as large as 10^{13}.[34] The electromagnetic enhancement factor E, is usually given by:

$$\mathrm{E} = \mathbf{E}\ \omega\ ^2\ \mathbf{E}\ \omega'\ ^2$$

where $\mathbf{E}\ \omega$ is the local electric field enhancement factor at the incident frequency ω and $\mathbf{E}\ \omega'$ is the electric field enhancement factor at the Stokes-shifted frequency ω'.

In 1997, Nie and co-workers,[6] and Kneipp and co-workers[5] simultaneously and independently discovered the phenomenon of single-molecule SERS (SMSERS). This technique can be used for detecting and identifying a single molecule without labeling, a method used in fluorescence spectroscopy.[5] The huge enhancement observed in SMSERS is facilitated by the strong surface plasmon-related electromagnetic fields within and around metallic nanostructures[35] although a resonance-Raman enhancement also contributes to the overall enhancement observed (~$10^{5\text{-}6}$).[36] Brus and co-workers[37-38] showed that the hot spots formed at the junction of two nanoparticles likely play a major role in SMSERS and this was supported by using atomic force microscopy (AFM) to show that the SMSERS-active structures were aggregates of Ag nanoparticles. Also, electrodynamics calculations have shown that anisotropic

nanoparticle dimers such as prisms can be a source of hot spots which would further increase the electromagnetic enhancement factor.[39-40] Advancement in the area of SMSERS has been hampered by the insufficient understanding of the nature of the hot spots that are responsible for the observed electromagnetic enhancements.[41]

Chapter Summaries

In this dissertation, the plasmonic properties of metallic nanostructures are investigated using resonance-Rayleigh scattering and STEM/EELS. Chapter I uses this approach in examining individual silver nanorods with varying aspect-ratios. Chapter II elucidates the nature of electromagnetic hot spots responsible for SMSERS, and the mechanism of this excitation in STEM/EELS. Finally, Chapter III investigates the properties of Fano interferences in silver nanocubes on a substrate, and the effect of raster-scanning the electron beam on the optical LSPR of the exact same nanocube. The studies published here demonstrate the complementarity of photon- and electron-driven plasmonic excitations.

Introduction References

(1) Faraday, M., The Bakerian Lecture: Experimental Relations of Gold (and Other Metals) to Light. *Philosophical Transactions of the Royal Society of London* **1857,** *147* (0), 145-181.

(2) Mie, G., Articles on the Optical Characteristics of Turbid Tubes, Especially Colloidal Metal Solutions. *Ann. Phys.-Berlin* **1908,** *25* (3), 377-445.

(3) Kelly, K. L.; Coronado, E.; Zhao, L. L.; Schatz, G. C., The Optical Properties of Metal Nanoparticles: The Influence of Size, Shape, and Dielectric Environment. *J. Phys. Chem. B* **2003,** *107* (3), 668-677.

(4) Jeanmaire, D. L.; Van Duyne, R. P., Surface Raman Spectroelectrochemistry .1. Heterocyclic, Aromatic, and Aliphatic-Amines Adsorbed on Anodized Silver Electrode. *J. Electroanal. Chem.* **1977,** *84* (1), 1-20.

(5) Kneipp, K.; Wang, Y.; Kneipp, H.; Perelman, L. T.; Itzkan, I.; Dasari, R.; Feld, M. S., Single Molecule Detection Using Surface-Enhanced Raman Scattering (Sers). *Phys. Rev. Lett.* **1997,** *78* (9), 1667-1670.

(6) Nie, S. M.; Emery, S. R., Probing Single Molecules and Single Nanoparticles by Surface-Enhanced Raman Scattering. *Science* **1997,** *275* (5303), 1102-1106.

(7) Homola, J.; Yee, S. S.; Gauglitz, G., Surface Plasmon Resonance Sensors: Review. *Sensors and Actuators B-Chemical* **1999,** *54* (1-2), 3-15.

(8) Catchpole, K. R.; Polman, A., Design Principles for Particle Plasmon Enhanced Solar Cells. *Appl. Phys. Lett.* **2008,** *93* (19), 191113.

(9) Garcia, M., Surface Plasmons in Metallic Nanoparticles: Fundamentals and Applications. *J. Phys. D: Appl. Phys.* **2011,** *44* (28), 283001.

(10) Oulton, R. F.; Sorger, V. J.; Genov, D.; Pile, D.; Zhang, X., A Hybrid Plasmonic Waveguide for Subwavelength Confinement and Long-Range Propagation. *Nature Photonics* **2008,** *2* (8), 496-500.

(11) Stockman, M. I., Nanofocusing of Optical Energy in Tapered Plasmonic Waveguides. *Phys. Rev. Lett.* **2004,** *93*, 137404-137404.

(12) Petroski, J. M.; Wang, Z. L.; Green, T. C.; El-Sayed, M. A., Kinetically Controlled Growth and Shape Formation Mechanism of Platinum Nanoparticles. *J. Phys. Chem. B* **1998,** *102* (18), 3316-3320.

(13) Jin, R. C.; Cao, Y. C.; Hao, E. C.; Metraux, G. S.; Schatz, G. C.; Mirkin, C. A., Controlling Anisotropic Nanoparticle Growth through Plasmon Excitation. *Nature* **2003,** *425* (6957), 487-490.

(14) Wiley, B.; Sun, Y. G.; Xia, Y. N., Polyol Synthesis of Silver Nanostructures: Control of Product Morphology with Fe(Ii) or Fe(Iii) Species. *Langmuir* **2005,** *21* (18), 8077-8080.

(15) Haynes, C. L.; Van Duyne, R. P., Nanosphere Lithography: A Versatile Nanofabrication Tool for Studies of Size-Dependent Nanoparticle Optics. *J. Phys. Chem. B* **2001,** *105* (24), 5599-5611.

(16) Kahl, M.; Voges, E.; Kostrewa, S.; Viets, C.; Hill, W., Periodically Structured Metallic Substrates for Sers. *Sensors and Actuators B: Chemical* **1998,** *51* (1), 285-291.

(17) Kim, D.-S.; Kim, Z. H., Role of in-Plane Polarizability of the Tip in Scattering near-Field Microscopy of a Plasmonic Nanoparticle. *Opt. Express* **2012,** *20* (8), 8689-8699.

(18) Neacsu, C. C.; Steudle, G. A.; Raschko, M. B., Plasmonic Light Scattering from Nanoscopic Metal Tips. *Appl. Phys. B-Lasers Opt.* **2005,** *80* (3), 295-300.

(19) Rang, M.; Jones, A. C.; Zhou, F.; Li, Z. Y.; Wiley, B. J.; Xia, Y. N.; Raschke, M. B., Optical near-Field Mapping of Plasmonic Nanoprisms. *Nano Lett.* **2008,** *8* (10), 3357-3363.

(20) Raschke, M. B.; Molina, L.; Elsaesser, T.; Kim, D. H.; Knoll, W.; Hinrichs, K., Apertureless near-Field Vibrational Imaging of Block-Copolymer Nanostructures with Ultrahigh Spatial Resolution. *ChemPhysChem* **2005,** *6* (10), 2197-2203.

(21) Weeber, J. C.; Krenn, J. R.; Dereux, A.; Lamprecht, B.; Lacroute, Y.; Goudonnet, J. P., Near-Field Observation of Surface Plasmon Polariton Propagation on Thin Metal Stripes. *Phys. Rev. B* **2001,** *64* (4).

(22) Nakayama, R.; Watanabe, R.; Namba, K.; Takeda, K.; Yomamoto, K.; Katsuragawa, S.; Doi, K., An Improved Computer-Aided Diagnosis Scheme Using the Nearest Neighbor Criterion for Determining Histological Classification of Clustered Microcalcifications. *Methods of Information in Medicine* **2007,** *46* (6), 716-722.

(23) Sonnichsen, C.; Franzl, T.; Wilk, T.; von Plessen, G.; Feldmann, J.; Wilson, O.; Mulvaney, P., Drastic Reduction of Plasmon Damping in Gold Nanorods. *Phys. Rev. Lett.* **2002,** *88* (7).

(24) Hartschuh, A.; Qian, H. H.; Meixner, A. J.; Anderson, N.; Novotny, L., Nanoscale Optical Imaging of Excitons in Single-Walled Carbon Nanotubes. *Nano Lett.* **2005,** *5*, 2310-2313.

(25) Chaturvedi, P.; Hsu, K. H.; Kumar, A.; Fung, K. H.; Mabon, J. C.; Fang, N. X., Imaging of Plasmonic Modes of Silver Nanoparticles Using High-Resolution Cathodoluminescence Spectroscopy. *ACS Nano* **2009,** *3* (10), 2965-2974.

(26) Ritchie, R. H., Plasmon Losses by Fast Electrons in Thin Films. *Phys. Rev.* **1957,** *106* (5), 874-881.

(27) Batson, P. E., A New Surface-Plasmon Resonance in Clusters of Small Aluminum Spheres. *Ultramicroscopy* **1982,** *9* (3), 277-282.

(28) Koh, A. L.; Bao, K.; Khan, I.; Smith, W. E.; Kothleitner, G.; Nordlander, P.; Maier, S. A.; McComb, D. W., Electron Energy-Loss Spectroscopy (Eels) of Surface Plasmons in Single Silver Nanoparticles and Dimers: Influence of Beam Damage and Mapping of Dark Modes. *ACS Nano* **2009,** *3* (10), 3015-3022.

(29) N'Gom, M.; Li, S. Z.; Schatz, G.; Erni, R.; Agarwal, A.; Kotov, N.; Norris, T. B., Electron-Beam Mapping of Plasmon Resonances in Electromagnetically Interacting Gold Nanorods. *Phys. Rev. B* **2009,** *80* (11).

(30) Fleischman.M; Hendra, P. J.; McQuilla.Aj, Raman-Spectra of Pyridine Adsorbed at a Silver Electrode. *Chemical Physics Letters* **1974,** *26* (2), 163-166.

(31) Albrecht, M. G.; Creighton, J. A., Anomalously Intense Raman-Spectra of Pyridine at a Silver Electrode. *J. Am. Chem. Soc.* **1977,** *99* (15), 5215-5217.

(32) Moskovits, M., Surface-Roughness and Enhanced Intensity of Raman-Scattering by Molecules Adsorbed on Metals. *J. Chem. Phys.* **1978,** *69* (9), 4159-4161.

(33) Haran, G., Single-Molecule Raman Spectroscopy: A Probe of Surface Dynamics and Plasmonic Fields. *Accounts of Chemical Research* **2010,** *43* (8), 1135-1143.

(34) Schatz, G. C.; Van Duyne, R. P., Electromagnetic Mechanism of Surface-Enhanced Spectroscopy. In *Handbook of Vibrational Spectroscopy*, Chalmers, J. M.; Griffiths, P. R., Eds. John Wiley & Sons Ltd: 2002.

(35) Moskovits, M., Surface-Ehanced Spectroscopy. *Rev. Mod. Phys.* **1985,** *57* (3), 783-826.

(36) Camden, J. P.; Dieringer, J. A.; Wang, Y. M.; Masiello, D. J.; Marks, L. D.; Schatz, G. C.; Van Duyne, R. P., Probing the Structure of Single-Molecule Surface-Enhanced Raman Scattering Hot Spots. *J. Am. Chem. Soc.* **2008,** *130* (38), 12616-12617.

(37) Michaels, A. M.; Jiang, J.; Brus, L., Ag Nanocrystal Junctions as the Site for Surface-Enhanced Raman Scattering of Single Rhodamine 6g Molecules. *J. Phys. Chem. B* **2000,** *104* (50), 11965-11971.

(38) Michaels, A. M.; Nirmal, M.; Brus, L. E., Surface Enhanced Raman Spectroscopy of Individual Rhodamine 6g Molecules on Large Ag Nanocrystals. *J. Am. Chem. Soc.* **1999,** *121* (43), 9932-9939.

(39) Hao, E.; Schatz, G. C., Electromagnetic Fields around Silver Nanoparticles and Dimers. *J. Chem. Phys.* **2004,** *120* (1), 357-366.

(40) Wells, S. M.; Retterer, S. D.; Oran, J. M.; Sepaniak, M. J., Controllable Nanotabrication of Aggregate-Like Nanoparticle Substrates and Evaluation for Surface-Enhanced Raman Spectroscopy. *ACS Nano* **2009,** *3* (12), 3845-3853.

(41) Hohenester, U.; Ditlbacher, H.; Krenn, J. R., Electron-Energy-Loss Spectra of Plasmonic Nanoparticles. *Phys. Rev. Lett.* **2009,** *103* (10).

CHAPTER I

CORRELATED OPTICAL MEASUREMENTS AND PLASMON MAPPING OF SILVER NANORODS

A version of this chapter was originally published by Beth S. Guiton, Vighter Iberi, Shuzhou Li, Donovan N. Leonard, Chad M. Parish, Paul G. Kotula, Maria Varela, George C. Schatz, Stephen J. Pennycook, and Jon P. Camden:

Guiton, B. S., Iberi, V., Li, S., Leonard, D. N., Parish, C. M., Kotula, P. G., Varela, M., Schatz, G. C., Pennycook, S. J. and Camden, J. P. **Correlated Optical Measurements and Plasmon Mapping of Silver Nanorods.** *Nano Letters* (2011), 11, 3482-3488.

The article is represented in the published form, with the exception that the following Nano Letters required sections have been removed: Associated Content, Author Information and Acknowledgements. The Supporting Information section of the manuscript has been added as an appendix. The dissertation author conducted all the experiments, analyzed all the data, prepared all the figures and wrote the experimental section of the manuscript. Multivariate statistical analysis (MVSA) was performed by CM Parish, PG Kotula and BS Guiton while S Li and GC Schatz performed the theoretical simulations. All authors participated in the discussion of the results and approved the final manuscript.

Abstract

Plasmonics is a rapidly growing field, yet imaging of the plasmonic modes in complex nanoscale architectures is extremely challenging. Here we obtain spatial maps of the localized surface plasmon modes of high-aspect-ratio silver nanorods using

electron energy loss spectroscopy (EELS) and correlated to optical data and classical electrodynamics calculations from the exact same particles. EELS mapping is thus demonstrated to be an invaluable technique for elucidating complex and overlapping plasmon modes.

Published Work

The collective oscillation of the conduction electrons in a metallic nanostructure, commonly excited by coupling to an electromagnetic field, is known as a localized surface plasmon (LSP).[1] These oscillations have frequencies and intensities which are highly sensitive to the shape, size, and dielectric environment of the nanostructure,[2] leading to a plethora of related applications such as photonic circuits,[3] wave-guiding on subdiffraction limit length scales,[4] and chemical and biological sensing;[5] plasmon excitation also leads to local enhancements of incident electromagnetic fields of several orders of magnitude, enabling the spectroscopic detection of single molecules.[6-8] Utilizing such materials requires intimate understanding of the relationship between the structure and the optical response of the material, which requires a characterization technique capable of elucidating the structure and functionality of the particle on the nanometer and subnanometer length scale. With the recent proliferation of aberration-corrected and monochromated transmission electron microscopes (TEMs), electron microscopy techniques - specifically electron energy loss spectroscopy (EELS) in the scanning transmission electron microscope (STEM), and energy filtered TEM (EFTEM) - have re-emerged as unique tools to map the energy and spatial distribution of metallic

nanoparticle plasmon modes on length scales relevant to the application of the LSP oscillation.[9-22]

While it is clear that LSPRs can be excited by both far-field optical excitation and fast moving electrons, the detailed connection between resonance-Rayleigh scattering, EELS mapping, and electrodynamics remains unexplored at the single particle level. Studies correlating these measurements are especially important, therefore, if the fundamental connection between EELS derived data and optically driven plasmons is to be elucidated. Theoretical studies have shown that the photonic density of states is related to the EELS intensity,[13] although it has been cautioned that a quantitative description of this coupling may not be possible.[23] The complexity of the experiment is increased further for high-aspect-ratio nanostructures, where data interpretation becomes challenging due to the many LSP components - both longitudinal and transverse.[24] Moreover, the “dark” modes of these particles are of fundamental interest for applications such as subdiffraction limit wave-guiding without radiative loss; a method to extract the rich and complex data from these systems is therefore urgently needed.

Here we present EELS mapping of plasmon modes for a series of silver nanorods, correlated for the first time to optical data taken from the exact same particles, and electrodynamics simulations utilizing the experimental geometries. Remarkably, we find that the many plasmon modes characteristic of high aspect-ratio particles can be reliably extracted using multivariate statistical analysis (MVSA). Further, the modes so identified are in excellent agreement with local field maps

obtained using plane wave excitation and classical electrodynamics modeling. Moreover, the main features of the resonance-Rayleigh scattering spectra from the correlated nanostructures are captured by the electrodynamics simulations, reinforcing the powerful connection between electron and optical excitation of plasmon modes. Similar components are resolved using both conducting (C) and insulating (SiN_x) substrates.

Samples were prepared by depositing commercially available solutions of silver nanoparticles directly onto TEM support films. Silver nanoparticles were obtained from nanoComposix and used without further purification. Our experiments utilized two types of TEM grids: (1) a copper grid coated with 2-3 nm of amorphous carbon on formvar (Ted Pella, Inc. #01822) and (2) 20 nm supported SiN_x membrane (SPI Supplies #4105SN). Prior to use the carbon grid was cleaned with HPLC grade chloroform to remove the formvar. These grids were chosen to allow comparison of STEM/EELS measurements on both conducting and non-conducting substrates. The SiN_x support produced superior results, due to a more even dispersion of the nanoparticles on this surface, and a higher signal-to-noise ratio in the optical scattering measurements. A 2 μL aliquot of the colloidal sample was drop-coated directly onto the TEM support, and the solvent was allowed to evaporate. Once the silver nanoparticles had been deposited, the sample was placed on a coverslip, mounted in a custom designed sample holder, and purged with dry nitrogen in order to remove water on the nanoparticles and grid.

First, resonance-Rayleigh scattering measurements were performed on a series of individual particles, and wide-field images were collected to serve as maps to enable the location of the same nanoparticles during subsequent STEM measurements. Scattering measurements were performed using an inverted microscope (Nikon, T*i*-U) equipped with a dark field condenser (Nikon,NA = 0.95-0.80). The excitation source was the unpolarized output of a tungsten halogen lamp. Scattered light from an individual nanoparticle was collected with a 100x (Nikon, 0.7<NA<1.4, oil immersion) objective and coupled into a dispersive imaging spectrometer (Acton Research, *f* = 0.3 m) using a *f* = 5.0 cm lens. Light was detected on a liquid nitrogen cooled back-illuminated charge couple detector (CCD) (Princeton Instruments, PIXIS 100). The dark-field scattering spectrum of each individual nanoparticle was obtained using a 150 grooves/mm grating with a 500 nm blaze. Similar to a procedure described by Wang et al.,[25] a wide-field image of the silver nanoparticles on the TEM grid was also recorded to serve as a map for subsequent location in the STEM. This method enabled correlated optical and STEM measurements from the same nanostructures.

After particles of interest had been identified from the optical characterization, the sample was inserted into a dedicated aberration-corrected, cold-field-emission STEM. Using the optical maps, each nanoparticle was found in turn and an EEL spectrum imaging (SI) map collected from the zero loss peak-containing region. In each case the rod in question was found by comparison of the optical map to the pattern of particles imaged in the STEM at very low resolution; after identification, a higher resolution annular dark field (ADF) image was collected (Figures 2a, 3a, and 4a), followed by the

SI. The STEM/EELS spectrum imaging measurement was performed on a VG Microscopes HB501UX STEM with Nion aberration corrector and Gatan Enfina EEL spectrometer. The spectrometer dispersion was set to 0.05 eV per channel with an exposure time of 0.05 s per spectrum. The pixel size/density was chosen to give a total acquisition time of around 15 mins for a single SI. The energy resolution (as measured by the fwhm of the zero loss peak) was ~0.45-0.50 eV. The data presented in this paper come from particles identified unambiguously as the same particles from which optical data were collected.

Next, we simulated the optical response and local field enhancements using the discrete dipole approximation (DDA),[19, 26-28] by the DDSCAT7.0 program.[29] In the DDA, silver rods are represented as a cubic array of polarizable elements whose polarizability is determined from the nanoparticle dielectric function.[26, 30] The silver rods discussed in this report were modeled as cylinders with a hemispherical cap at each end. Dipoles are induced as a result of the interaction of the polarizable elements with an incident plane wave field and with fields arising from the other polarizable elements. The fields outside the nanoparticle are determined from the superposition of the incident plane wave and the fields of the induced dipoles. These fields are calculated half a grid spacing from the surface, instead of right on the surface, in order to avoid numerical instabilities that arise at the surface. The grid spacing used was 1 nm and the dielectric constants of silver were from Palik.[31] The refractive index of the surrounding medium was fixed at a value of 1.35 to include the substrate effect implicitly. It is known that the optical scattering spectra of nanoparticles can depend on the solid angle of collection;

this effect is not modeled in our electrodynamics simulations. In our current measurements the use of a high numerical aperture objective should minimize these effects, although studies exploring the dependence of the scattering spectra on the polarization and solid angle of collection are an interesting avenue of future research.

Data analysis for high aspect-ratio particles is especially challenging due to the large number of overlapping (both spatially and spectrally) LSP modes.[24] To extract the experimentally measured modes from our data, we employed MVSA, using the Automated eXpert Spectral Image Analysis (AXSIA) program developed by Keenan and co-workers.[32-34] This software uses a combination of principal component analysis (PCA) with matrix rotation to maximize spectral contrast,[32] thus improving the interpretability of the individual components.[35] The resulting decomposed data comprised spatial maps of the individual LSP component spectra, which we were able to compare with the simulated field plots.

To perform the data analysis, first the zero loss peak (ZLP) was fit to a Gaussian plus Lorentzian using Gatan Digital Micrograph software; peak centering at zero electron volts was performed to align the individual spectra, and a ZLP subtraction was performed. Examination of the spectrum image before deconvolution reveals a progression of overlapping modes - energy slices of these data for Rod 1 are given in Figure 6 (Appendix for Chapter I). Noise reduction is achieved using MVSA methods, which extract the experimentally-measured modes using a PCA followed by matrix rotations, using AXSIA.[32-33] MVSA methods decompose SI data into spatial and spectral-component matrices. The procedure applied by AXSIA first scales the data for

non-Gaussian noise.[36-37] This so-called optimal-scaling normalization or Poisson-scaling method was used to account for the nature of the noise in the data,[36] whereby higher signal levels are contaminated by noise in proportion to the signal and therefore need to be down-weighted prior to MVSA (lest such algorithms fit noise at the expense of weaker but relevant spectral information). An eigenanalysis was then performed on the scaled data in order to determine the pseudo- or chemical-rank of the decomposed spectral and spatial matrices. Normally, the sorted eigenvalues are interrogated manually but AXSIA employs an automated routine to discriminate noise from non-noise components (the so-called breakpoint in the aforementioned plot). In principle, this reduced rank approximation of the data provides a succinct description of the signal and suppresses the experimental noise. PCA is then performed on the scaled data with the previously determined pseudo-rank prescribing the number of retained components. The AXSIA software allows additional manipulation of the data in the form of matrix rotations, which in the case of the data presented here maximizes the spectral components' mutual simplicity (or contrast) and is used to improve the interpretability of the individual components. The resulting decomposed data comprised two matrices which include spatial components and respective spectral components, each displaying one well-defined peak, which we took to represent the plasmon mode and its corresponding spectrum or energy. Before AXSIA was run, the centered and ZLP-subtracted data were truncated to the region of interest (a wide energy range of 0.45-8.45 eV was chosen, to avoid deleting relevant information), and the noise normalization,[36-37] PCA decomposition, rotation of the spectral components via the

Varimax procedure[32] and related inverse rotation of the spatial components, and inverse noise normalization to return to real counts from scaled counts were performed. Specifically, the operations performed by AXSIA are, in the following order: (1) a Poisson scaling;[36-37] (2) a PCA, resulting in orthogonal spatial components and orthonormal spectral components; (3) a rotation of the orthonormal spectral basis using Varimax[32] and an inverse rotation of the spatial components which as a result are no longer orthogonal; (4) an inverse Poisson scaling to return to physical count space from Poisson space, resulting in spectral and spatial components which are now both oblique. These resultant matrices nonetheless retain the relevant and interpretable spectral and spatial information. It should be noted for clarity that while the title of Keenan et al.[32] is concerned with "spatial-domain simplicity", the paper is more general and discusses the method underlying "spectral-domain simplicity" as applied here.

Figures 2-4 compare experimental and theoretical plasmon maps for three nanorods analyzed in this way. In the case of all three rods four or more components are resolved in the 0.5 - 4.0 eV region (Figures 2-4, panels b and c). Where individual rotated PCA components appeared to display the same symmetry and were separated in energy by less than the spectral resolution of the measurement (~0.45 eV) we superimposed them into a single component; this is noted in the figure caption where it applies, and all of the uncombined modes are displayed in the Supporting Information (Figures 7-9). Figures 2-4 represent the first demonstration of an experimental mapping of plasmon modes at this level of complexity. In each case dipolar modes are observed below 1 eV, followed by a series of quadrupolar and higher multipolar modes with

increasing numbers of nodes for increasing energy, with transverse modes emerging above 3 eV. Our approach is shown to be general by the consistency of the results between the different rods. As expected, additional multipolar modes emerge as the rod aspect-ratio increases (e.g., Figure 2 versus Figures 3 and 4), and the mode energy increases with decreasing aspect-ratio. The EEL spectra displayed in each figure (Figures 2e, 3e, and 4e) are the sum of all the spectra from the centered, ZLP-removed SI, *before* MVSA.

The calculated field-enhancement plots obtained from plane wave excitation, given as $|E_{loc}|^2/|E_0|^2$, are in excellent agreement with both the energy and spatial distribution of the MVSA extracted plasmon maps. This agreement is quite striking given the simplicity of our theoretical approach and suggests a more general applicability of EELS to the mapping of optically driven plasmons. In some cases the nodes in the experimentally determined plasmon maps are not as clearly demarcated as in the theoretical plots and we attribute this to the finite energy resolution of the experiment (e.g., the E = 2.2 eV mode in panels b and d of Figure 3). In the electrodynamics calculations, excitation of all experimentally observed plasmon modes is not possible with the polarization parallel to the rod axis; the inactive modes, however, are active when the laser polarization is rotated 45° with respect to the rod axis. The slight asymmetry of the field plots in these cases, resulting from retardation effects,[38] has been reduced by taking an average of the +45° and -45° polarization directions. The polarization direction in each case is indicated in the figure inset.

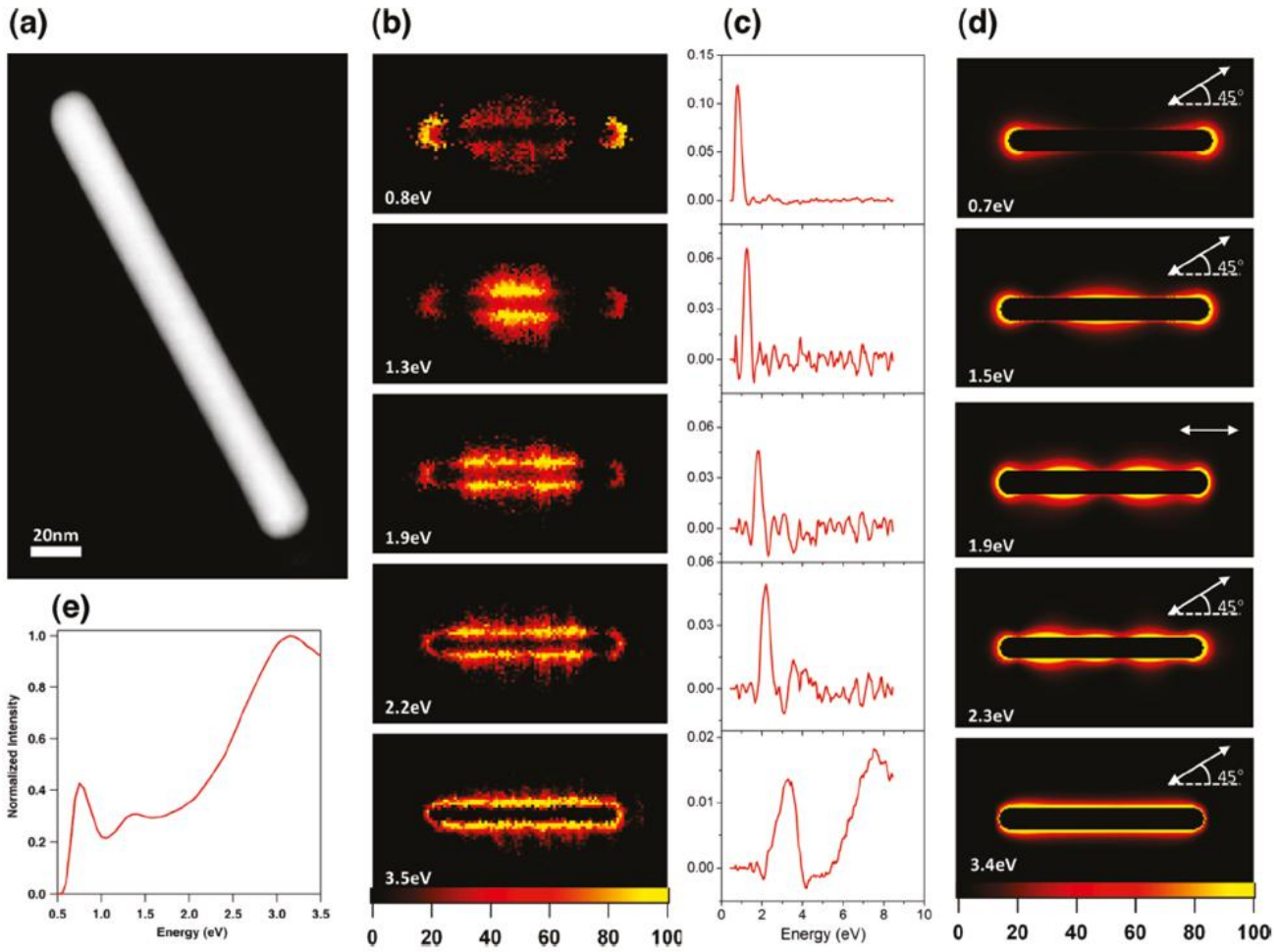

Figure 2. EELS data and electrodynamics calculations for Rod 1. (a) ADF image of the rod: length = 192 nm, diameter = 20 nm, aspect-ratio = 9.6. (b) MVSA score images, and (c) loading spectra, for each component, interpreted as plasmon maps and energies, respectively. From a total of 12 components found by MVSA, four components were considered overlapping and combined to form the E = 0.8 eV mode, two were combined to form the E = 3.5 eV mode, and three are displayed as found. (d) DDA calculated electric field plots displaying the field generated by a plane wave optical excitation at the energies and polarizations given on each panel. (e) Summed EEL spectrum.

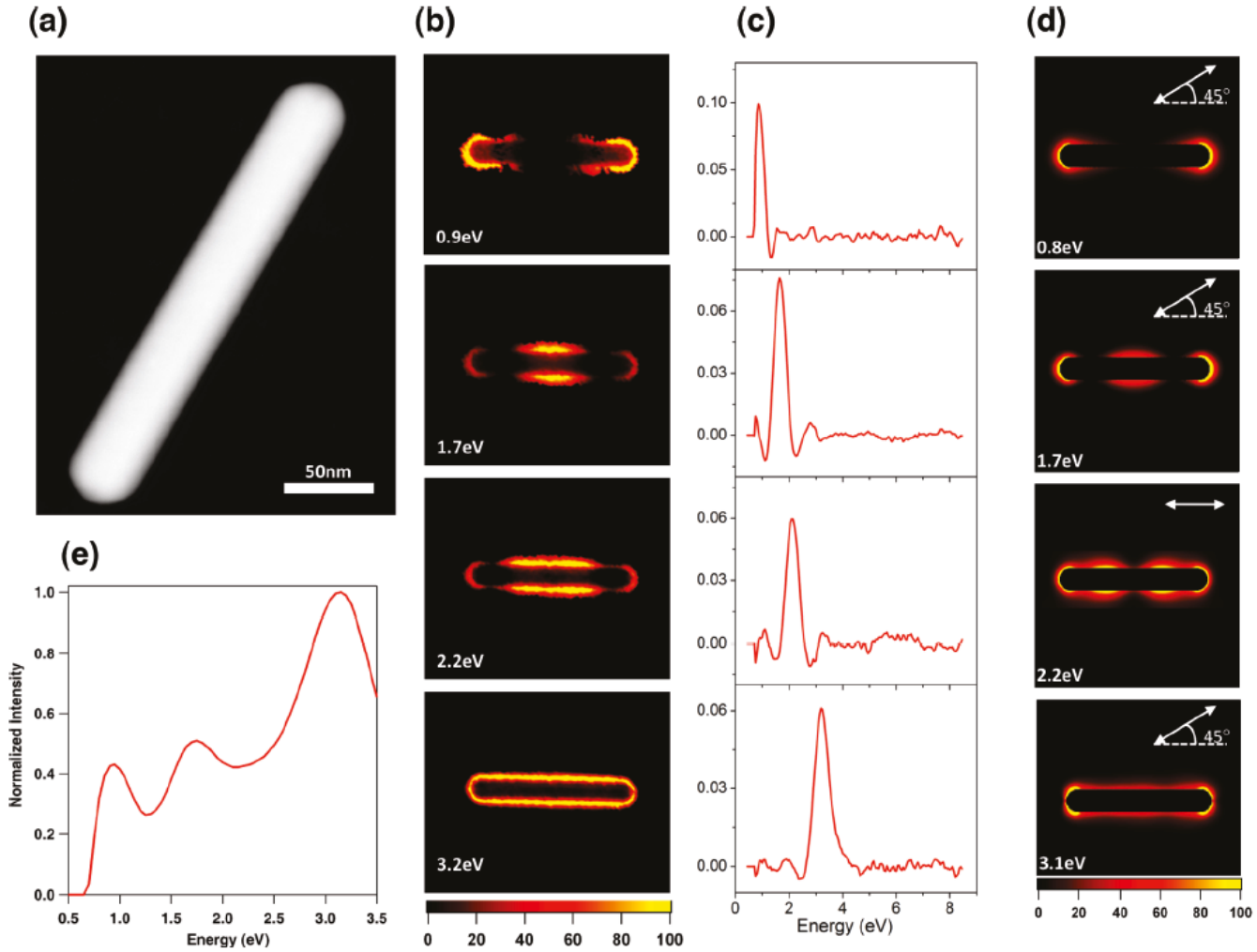

Figure 3. EELS data and electrodynamics calculations for Rod 2. (a) ADF image of the rod: length = 267 nm, diameter = 42 nm, aspect-ratio = 6.4. (b) MVSA score images, and (c) loading spectra, for each component, interpreted as plasmon maps and energies, respectively. From a total of 11 components found by MVSA, four components were considered overlapping and combined to form the E = 0.9 eV mode, two were combined to form the E = 3.2 eV mode, and three are displayed as found. (d) DDA calculated electric field plots displaying the field generated by a plane wave optical excitation at the energies and polarizations given on each panel. (e) Summed EEL spectrum.

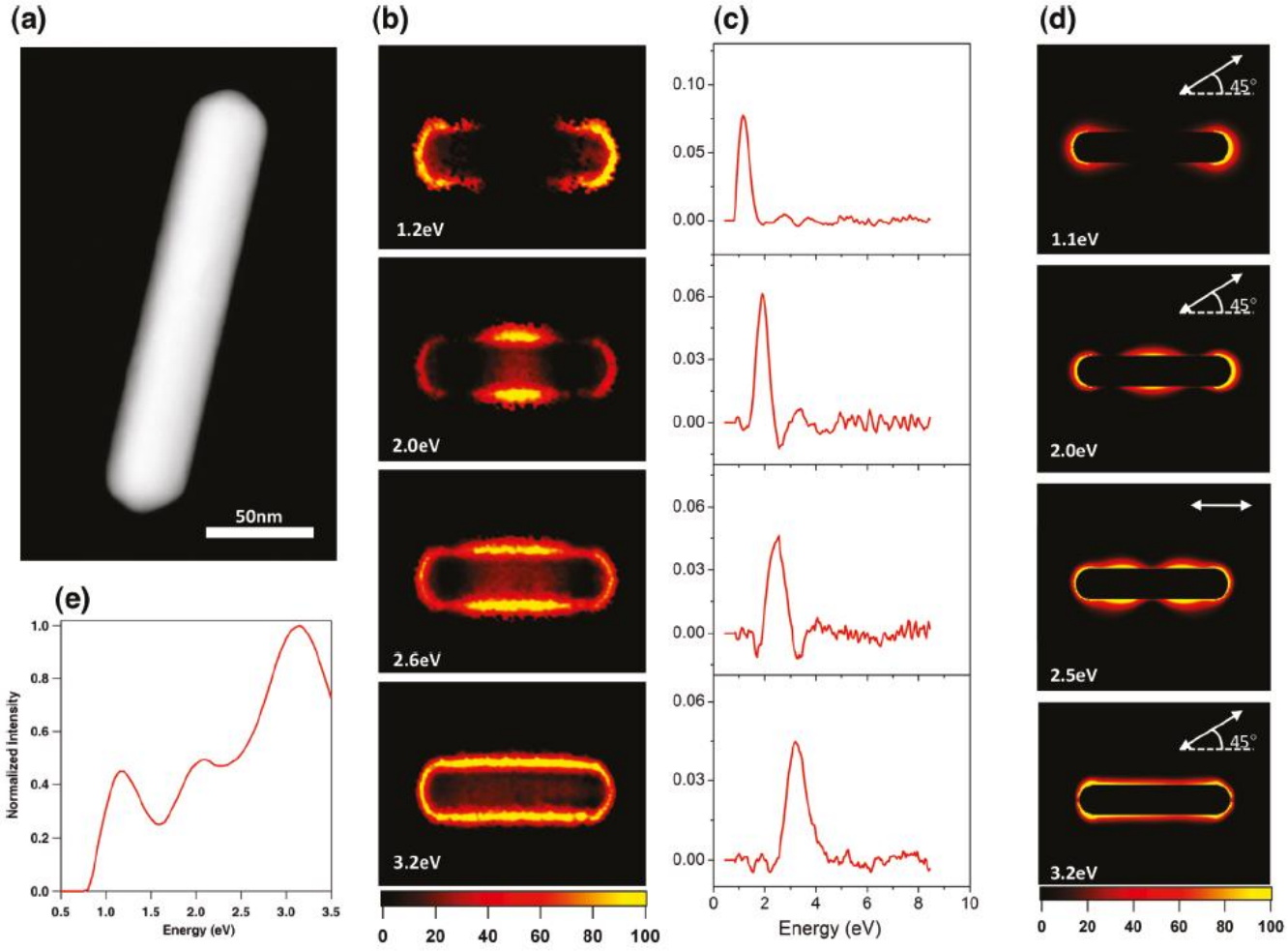

Figure 4. EELS data and electrodynamics calculations for Rod 3. (a) ADF image of the rod: length = 202 nm, diameter = 40 nm, aspect-ratio = 5.1. (b) MVSA score images, and (c) loading spectra, for each component, interpreted as plasmon maps and energies, respectively. From a total of 12 components found by MVSA, two components were considered overlapping and combined to form the E = 1.2 eV mode, two were combined to form the E = 3.2 eV mode, and two are displayed as found. (d) DDA calculated electric field plots displaying the field generated by a plane wave optical excitation at the energies and polarizations given on each panel. (e) Summed EEL spectrum.

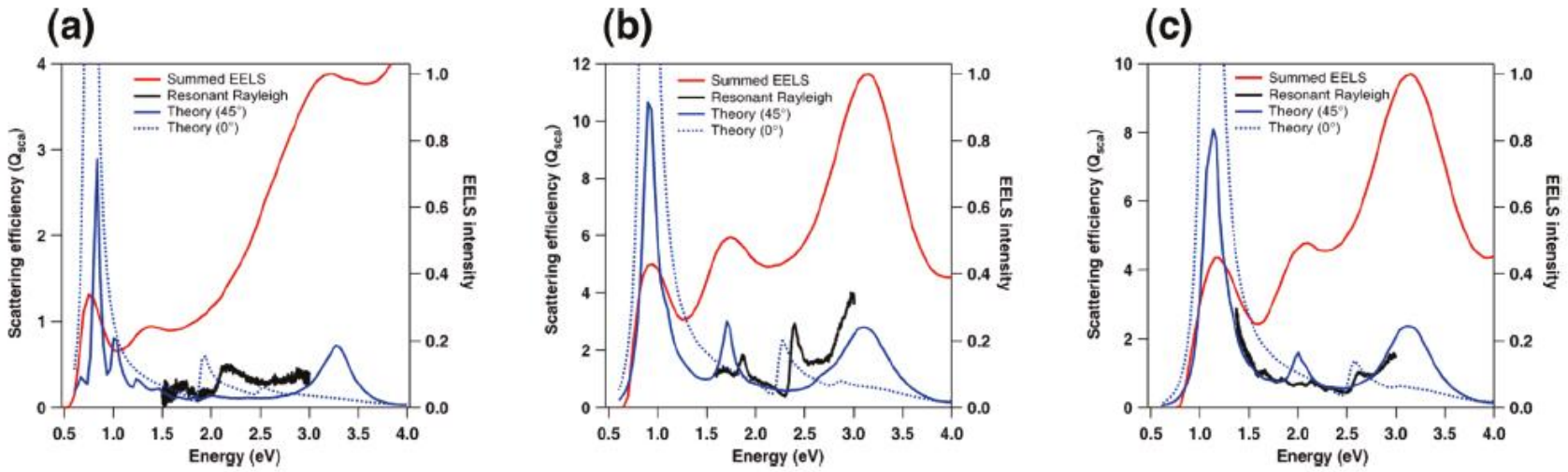

Figure 5. Comparison of spectra collected/simulated for each rod: (a) Rod 1; (b) Rod 2; (c) Rod 3. The EEL spectrum in each case (shown in red) is the sum of all spectra from the SI after zero-loss-peak centering and removal: black, experimental resonance-Rayleigh scattering spectra; blue, theoretical calculations of the scattering spectra for polarizations at 0° and 45° with respect to the rod axis (dotted and solid lines, respectively). The experimental spectra for Rod 1 (a) was obtained on a C support film whereas Rods 2 and 3 ((b) and (c)) were supported on a SiN_x membrane.

Figure 5 presents a comparison of the summed EELS spectra with the experimentally measured resonance-Rayleigh spectra and the theoretically calculated nanorod scattering spectra. In each case, the total EEL spectrum exhibits three broad peaks which we attribute to collections of plasmon components in order of increasing energy: dipolar, multipolar, and transverse. The peak positions of the longitudinal (dipole <1 eV) and transverse (>3 eV) modes in the theoretically calculated optical scattering spectra correlate well with peaks in the EEL spectra. There are differences in intensity as might be expected since the excitation mechanism in each case is different, i.e., plane wave versus electron beam. Figure 5 also compares the experimental resonance-Rayleigh spectra with simulated scattering spectra. The modes with the strongest optical activity are the dipolar modes (<1 eV) and the bulk plasmon modes (>3 eV); however, the optical data are limited to the visible region of the spectrum (1.5-3.0 eV) and does not encompass these modes. In the measured energy range the scattering features, e.g., the 1.8 and 2.4 eV experimental modes in Figure 5b, are estimated to be an order of magnitude smaller than the dipolar scattering peak. Despite this fact, we still find that the main features in the experimental scattering spectra are reproduced in the theoretical scattering spectra. The small shifts between the theoretical and experimental peak positions result because these weak modes are particularly sensitive to the dielectric environment. While the agreement between our electrodynamics simulations and the experimental scattering spectra is not quantitative, the agreement between the calculated electric field enhancement plots and EELS maps is striking (Figures 2-4). These data taken together suggest that correlated studies such

as these will ultimately provide a unified picture of optical and electron beam excited plasmons. Further, it reinforces the notion that plasmon maps derived from EELS excitation have direct relevance for the plethora of processes relying on optical excitation of plasmons.

A comparison of optical scattering measurements or individual EEL spectra (Figure 5), with that obtained from a MVSA of the EEL SI (Figures 2-4) reveals that vastly more information is available by utilizing EELS mapping. Where the optical spectrum measures only specific allowed transitions within a limited energy range, and the summed EEL spectrum shows overlapping collections of modes, MVSA reveals all of the symmetries and energies predicted by simulation – including both bright and dark modes, with spatial resolution on the length scale of the plasmon itself. It is clear from comparison of the summed EEL spectra with the MVSA deconvoluted EELS plasmon maps that the relatively low energy resolution of the electron microscope leads to such great spectral overlap of modes that they cannot be identified without spatial mapping combined with deconvolution. For complex or high aspect-ratio nanostructures, it is insufficient to take individual spectra, even from a series of points on an image, nor will energy slices (such as produced by EFTEM imaging) properly separate modes with close spectral overlap. We also believe that correlated optical and EELS measurements from the exact same nanostructure are necessary to understand the connection between photon and electron excited plasmons. Low-energy-loss EEL SI mapping with MVSA analysis, when combined with correlated optical scattering data and electrodynamics modeling, therefore provides an invaluable method for the

characterization of plasmonic nanostructures whose complexity will only continue to increase in the future.

References for Chapter I

(1) Maier, S. A., *Plasmonics: Fundamentals and Applications*. 1st ed.; Springer-Verlag: New York, 2007.

(2) Kelly, K. L.; Coronado, E.; Zhao, L. L.; Schatz, G. C., The Optical Properties of Metal Nanoparticles: The Influence of Size, Shape, and Dielectric Environment. *J. Phys. Chem. B* **2003,** *107* (3), 668-677.

(3) Maier, S. A., Plasmonics: The Promise of Highly Integrated Optical Devices. *Ieee Journal of Selected Topics in Quantum Electronics* **2006,** *12* (6), 1671-1677.

(4) Maier, S. A.; Kik, P. G.; Atwater, H. A.; Meltzer, S.; Harel, E.; Koel, B. E.; Requicha, A. A. G., Local Detection of Electromagnetic Energy Transport Below the Diffraction Limit in Metal Nanoparticle Plasmon Waveguides. *Nat. Mater.* **2003,** *2* (4), 229-232.

(5) Sannomiya, T.; Hafner, C.; Voros, J., In Situ Sensing of Single Binding Events by Localized Surface Plasmon Resonance. *Nano Lett.* **2008,** *8* (10), 3450-3455.

(6) Haran, G., Single-Molecule Raman Spectroscopy: A Probe of Surface Dynamics and Plasmonic Fields. *Accounts of Chemical Research* **2010,** *43* (8), 1135-1143.

(7) Kneipp, K.; Wang, Y.; Kneipp, H.; Perelman, L. T.; Itzkan, I.; Dasari, R.; Feld, M. S., Single Molecule Detection Using Surface-Enhanced Raman Scattering (Sers). *Phys. Rev. Lett.* **1997,** *78* (9), 1667-1670.

(8) Nie, S. M.; Emery, S. R., Probing Single Molecules and Single Nanoparticles by Surface-Enhanced Raman Scattering. *Science* **1997,** *275* (5303), 1102-1106.

(9) Arslan, I.; Hyun, J. K.; Erni, R.; Fairchild, M. N.; Hersee, S. D.; Muller, D. A., Using Electrons as a High-Resolution Probe of Optical Modes in Individual Nanowires. *Nano Lett.* **2009,** *9* (12), 4073-4077.

(10) Batson, P. E., Surface-Plasmon Coupling in Clusters of Small Spheres. *Phys. Rev. Lett.* **1982,** *49* (13), 936-940.

(11) Bosman, M.; Keast, V. J.; Watanabe, M.; Maaroof, A. I.; Cortie, M. B., Mapping Surface Plasmons at the Nanometre Scale with an Electron Beam. *Nanotechnology* **2007,** *18* (16), 165505.

(12) Chu, M. W.; Myroshnychenko, V.; Chen, C. H.; Deng, J. P.; Mou, C. Y.; de Abajo, F. J. G., Probing Bright and Dark Surface-Plasmon Modes in Individual and Coupled Noble Metal Nanoparticles Using an Electron Beam. *Nano Lett.* **2009,** *9* (1), 399-404.

(13) Garcia de Abajo, F. J., Optical Excitations in Electron Microscopy. *Rev. Mod. Phys.* **2010,** *82* (1), 209-275.

(14) Gu, L.; Sigle, W.; Koch, C. T.; Nelayah, J.; Srot, V.; van Aken, P. A., Mapping of Valence Energy Losses Via Energy-Filtered Annular Dark-Field Scanning Transmission Electron Microscopy. *Ultramicroscopy* **2009,** *109* (9), 1164-1170.

(15) Keast, V.; Bosman, M., Applications and Theoretical Simulation of Low-Loss Electron Energy-Loss Spectra. *Materials Science and Technology* **2008,** *24* (6), 651-659.

(16) Koh, A. L.; Fernandez-Dominguez, A. I.; McComb, D. W.; Maier, S. A.; Yang, J. K. W., High-Resolution Mapping of Electron-Beam-Excited Plasmon Modes in Lithographically Defined Gold Nanostructures. *Nano Lett.* **2011,** *11* (3), 1323-1330.

(17) Nelayah, J.; Gu, J.; Sigle, W.; Koch, C. T.; Pastoriza-Santos, I.; Liz-Marzan, L. M.; van Aken, P. A., Direct Imaging of Surface Plasmon Resonances on Single Triangular Silver Nanoprisms at Optical Wavelength Using Low-Loss Eftem Imaging. *Opt. Lett.* **2009,** *34* (7), 1003-1005.

(18) Nelayah, J.; Kociak, M.; Stephan, O.; de Abajo, F. J. G.; Tence, M.; Henrard, L.; Taverna, D.; Pastoriza-Santos, I.; Liz-Marzan, L. M.; Colliex, C., Mapping Surface Plasmons on a Single Metallic Nanoparticle. *Nat. Phys.* **2007,** *3* (5), 348-353.

(19) N'Gom, M.; Li, S. Z.; Schatz, G.; Erni, R.; Agarwal, A.; Kotov, N.; Norris, T. B., Electron-Beam Mapping of Plasmon Resonances in Electromagnetically Interacting Gold Nanorods. *Phys. Rev. B* **2009,** *80* (11).

(20) Schaffer, B.; Grogger, W.; Kothleitner, G.; Hofer, F., Comparison of Eftem and Stem Eels Plasmon Imaging of Gold Nanoparticles in a Monochromated Tem. *Ultramicroscopy* **2010,** *110* (8), 1087-1093.

(21) Schaffer, B.; Hohenester, U.; Trügler, A.; Hofer, F., High-Resolution Surface Plasmon Imaging of Gold Nanoparticles by Energy-Filtered Transmission Electron Microscopy. *Phys. Rev. B* **2009,** *79* (4).

(22) Sigle, W.; Nelayah, J.; Koch, C. T.; van Aken, P. A., Electron Energy Losses in Ag Nanoholes?From Localized Surface Plasmon Resonances to Rings of Fire. *Opt. Lett.* **2009,** *34* (14), 2150-2152.

(23) Hohenester, U.; Ditlbacher, H.; Krenn, J. R., Electron-Energy-Loss Spectra of Plasmonic Nanoparticles. *Phys. Rev. Lett.* **2009,** *103* (10).

(24) Koh, A. L.; Bao, K.; Khan, I.; Smith, W. E.; Kothleitner, G.; Nordlander, P.; Maier, S. A.; McComb, D. W., Electron Energy-Loss Spectroscopy (Eels) of Surface Plasmons in Single Silver Nanoparticles and Dimers: Influence of Beam Damage and Mapping of Dark Modes. *ACS Nano* **2009,** *3* (10), 3015-3022.

(25) Wang, Y.; Eswaramoorthy, S. K.; Sherry, L. J.; Dieringer, J. A.; Camden, J. P.; Schatz, G. C.; Van Duyne, R. P.; Marks, L. D., A Method to Correlate Optical Properties and Structures of Metallic Nanoparticles. *Ultramicroscopy* **2009,** *109* (9), 1110-1113.

(26) Draine, B. T.; Flatau, P. J., Discrete-Dipole Approximation for Periodic Targets: Theory and Tests. *J. Opt. Soc. Am. A:* **2008,** *25* (11), 2693-2703.

(27) Li, S.; Pedano, M. L.; Chang, S.-H.; Mirkin, C. A.; Schatz, G. C., Gap Structure Effects on Surface-Enhanced Raman Scattering Intensities for Gold Gapped Rods. *Nano Lett.* **2010,** *10* (5), 1722-1727.

(28) Zhang, J.; Li, S.; Wu, J.; Schatz, G. C.; Mirkin, C. A., Plasmon-Mediated Synthesis of Silver Triangular Bipyramids. *Angewandte Chemie-International Edition* **2009,** *48* (42), 7787-7791.

(29) Draine, B. T. F., P. J., User Guide for the Discrete Dipole Approximation Code Ddscat 7.1 Http://Arxiv.Org/Abs/0809.0337v5.

(30) Draine, B. T.; Flatau, P. J., Discrete-Dipole Approximation for Scattering Calculations. *J. Opt. Soc. Am. A:* **1994,** *11* (4), 1491-1499.

(31) Lynch, D. W. H., W. R. , *Handbook of Optical Constants of Solids*. Academic Press: New York, 1985.

(32) Keenan, M. R., Exploiting Spatial-Domain Simplicity in Spectral Image Analysis. *Surface and Interface Analysis* **2009,** *41* (2), 79-87.

(33) Kotula, P. G.; Keenan, M. R.; Michael, J. R., Automated Analysis of Sem X-Ray Spectral Images: A Powerful New Microanalysis Tool. *Microscopy and Microanalysis* **2003,** *9* (01), 1-17.

(34) Ohlhausen, J. A. T.; Keenan, M. R.; Kotula, P. G.; Peebles, D. E., Multivariate Statistical Analysis of Time-of-Flight Secondary Ion Mass Spectrometry Images Using Axsia. *Appl. Surf. Sci.* **2004,** *231*, 230-234.

(35) Smentkowski, V. S.; Ostrowski, S. G.; Keenan, M. R., A Comparison of Multivariate Statistical Analysis Protocols for Tof-Sims Spectral Images. *Surface and Interface Analysis* **2009,** *41* (2), 88-96.

(36) Keenan, M. R.; Kotula, P. G., Accounting for Poisson Noise in the Multivariate Analysis of Tof-Sims Spectrum Images. *Surface and Interface Analysis* **2004,** *36* (3), 203-212.

(37) Keenan, M. R.; Kotula, P. G., Optimal Scaling of Tof-Sims Spectrum-Images Prior to Multivariate Statistical Analysis. *Appl. Surf. Sci.* **2004,** *231–232* (0), 240-244.

(38) Payne, E. K.; Shuford, K. L.; Park, S.; Schatz, G. C.; Mirkin, C. A., Multipole Plasmon Resonances in Gold Nanorods. *The Journal of Physical Chemistry B* **2006,** *110* (5), 2150-2154.

Appendix for Chapter I

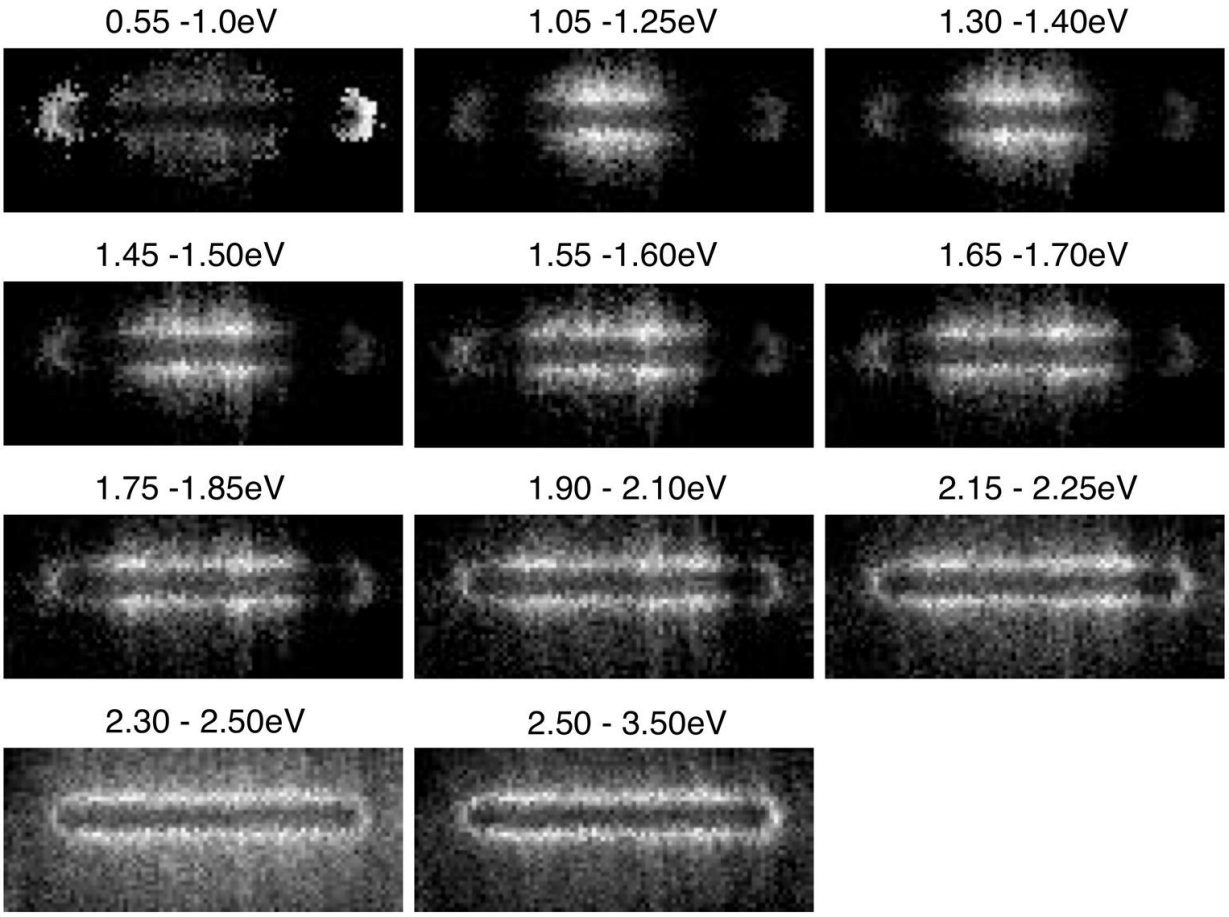

Figure 6. Energy slices from the spectrum image of Rod 1, after centering and ZLP subtraction, but before noise reduction with principal component analysis (PCA).

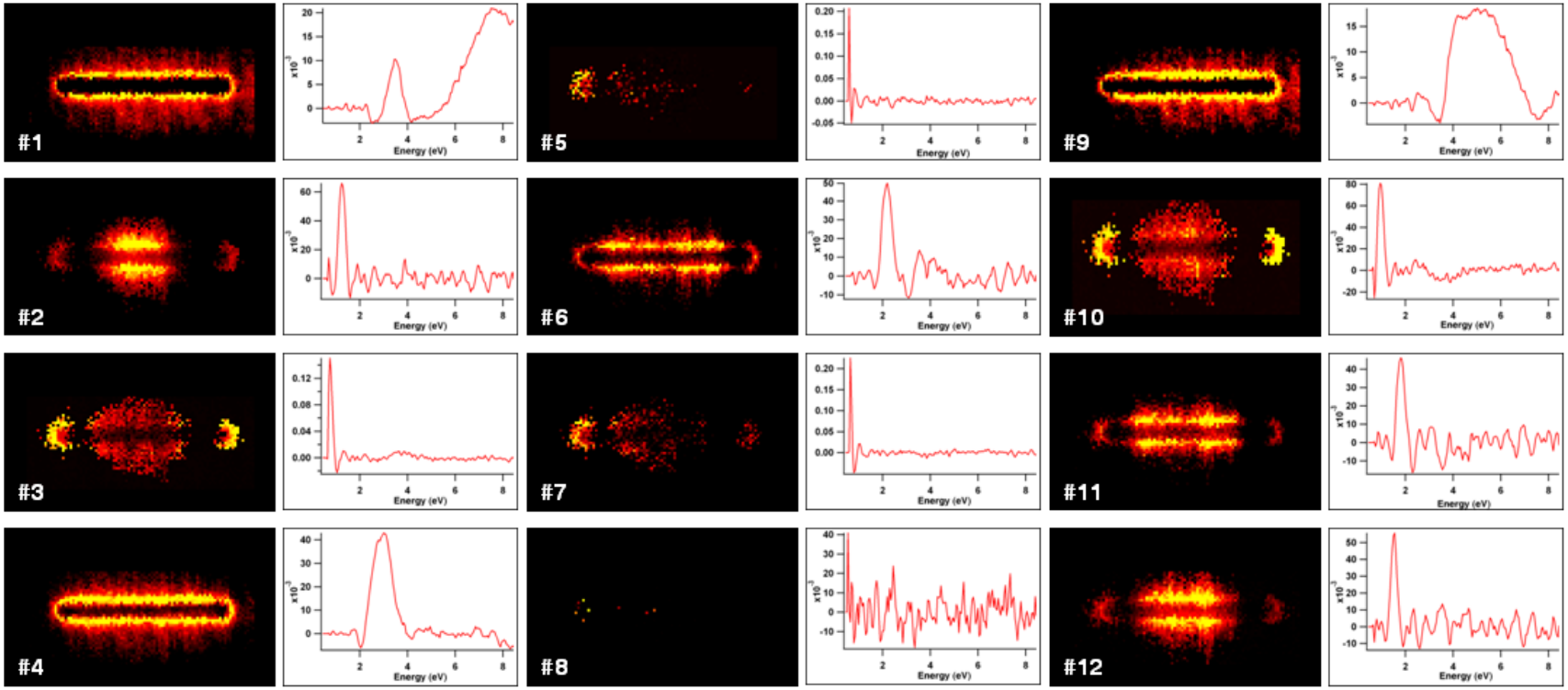

Figure 7. All of the components found by AXSIA for Rod 1, numbered according to their pseudo-rank from the eigenanalysis. Components #3, #5, #7, and #10 were superimposed to form the 0.8 eV component, and components #1 and #4 were superimposed to form the 3.5 eV component, in Figure 2 of the manuscript.

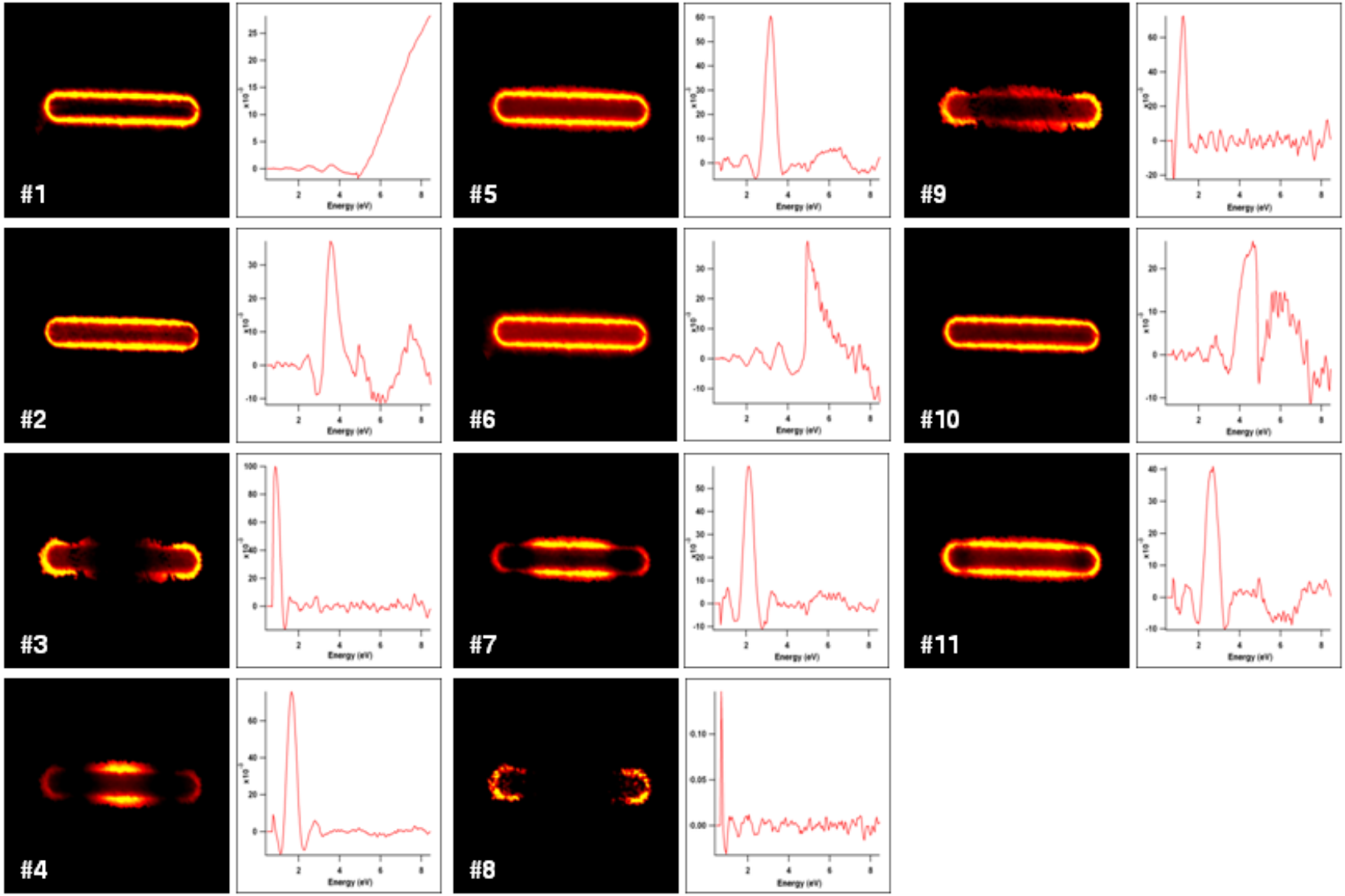

Figure 8. All of the components found by AXSIA for Rod 2, numbered according to their pseudo-rank from the eigenanalysis. Components #3 and #8 were superimposed to form the 0.9 eV component, and components #2 and #5 40 were superimposed to form the 3.2 eV component, in Figure 3 of the manuscript.

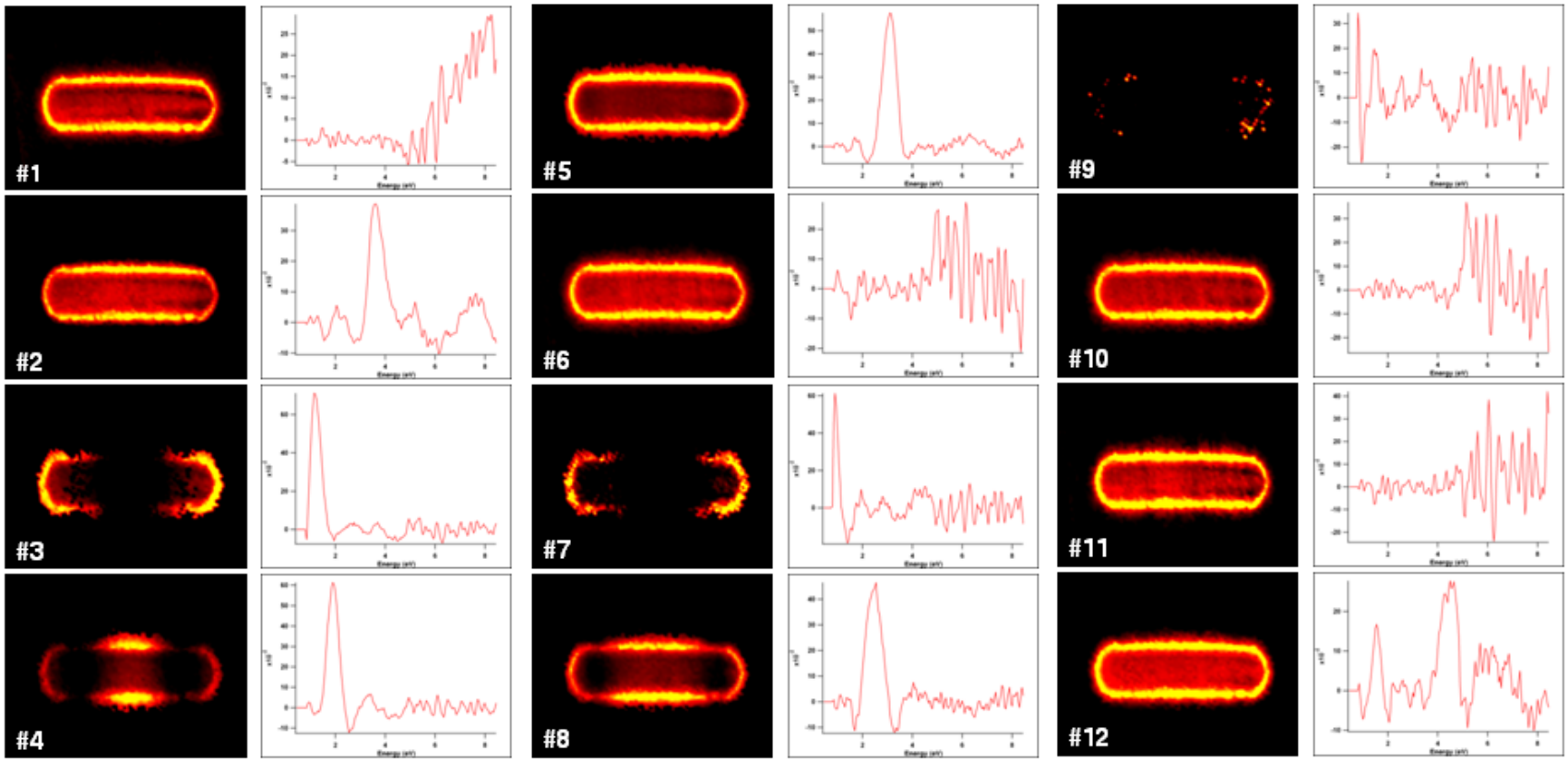

Figure 9. All of the components found by AXSIA for Rod 3, numbered according to their pseudo-rank from the eigenanalysis. Components #3 and #7 were superimposed to form the 1.2 eV component, and components #2 and #5 were superimposed to form the 3.2 eV component, in Figure 4 of the manuscript.

CHAPTER II

SINGLE-MOLECULE SURFACE-ENHANCED RAMAN SCATTERING: CAN STEM/EELS IMAGE ELECTROMAGNETIC HOT SPOTS?

A version of this chapter was originally published by Vighter Iberi, Nasrin Mirsaleh-Kohan, Philip D. Simmons, Jr., Nicholas W. Bigelow, Alex Vaschillo, Meng M. Rowland, Michael D. Best, Stephen J. Pennycook, David J. Masiello, Beth S. Guiton, and Jon P. Camden:

Iberi, V., Mirsaleh-Kohan, N., Simmons, P. D., Bigelow, N. W., Vaschillo, A., Rowland, M. M., Best, M. D., Pennycook, S. J., Masiello, D. J., Guiton, B. S., and Camden, J. P. **Single-Molecule Surface-Enhanced Raman Scattering: Can STEM/EELS Image Electromagnetic Hot Spots?.** *The Journal of Physical Chemistry Letters* (2012), 3, 2303-2309.

The article is represented in the published form, with the exception that the following J. Phys. Chem. Lett. required sections have been removed: Associated Content, Author Information and Acknowledgements. The Methods and Supporting Information sections of the manuscript have been added as an appendix. The dissertation author and N Mirsaleh-Kohan conducted all the experiments, analyzed all the data, designed all the figures and wrote the manuscript with equal contribution. MM Rowland and MD Best synthesized the molecules, while NW Bigelow, A Vaschillo and DJ Masiello performed the theoretical simulations. All authors participated in the discussion of the results and approved the final manuscript.

Abstract

Since the observation of single-molecule surface-enhanced Raman scattering (SMSERS) in 1997, questions regarding the nature of the electromagnetic hot spots responsible for such observations still persist. For the first time, we employ electron-energy-loss spectroscopy (EELS) in a scanning transmission electron microscope (STEM) to obtain maps of the localized surface plasmon modes of SMSERS-active nanostructures, which are resolved in both space and energy. Single-molecule character is confirmed by the bianalyte approach using two isotopologues of Rhodamine 6G. Surprisingly, the STEM/EELS plasmon maps do not show any direct signature of an electromagnetic hot spot in the gaps between the nanoparticles. The origins of this observation are explored using a fully three-dimensional electrodynamics simulation of both the electron-energy-loss probability and the near-electric field enhancements. The calculations suggest that electron beam excitation of the hot spot is possible, but only when the electron beam is located outside of the junction region.

Published Work

Surface-enhanced Raman scattering (SERS),[1-3] discovered more than three decades ago, relies on the localized surface plasmon resonance (LSPR)[4-5] to deliver large Raman enhancement factors (10^6 - 10^{10}) to molecules located close to the surface of plasmonic nanostructures. The SERS effect is so dramatic that, despite the weakness of Raman scattering, the vibrational spectrum of a single molecule can be easily observed.[6-7] The claims of single-molecule SERS (SMSERS) were initially met

with skepticism because of the extraordinary enhancements proposed (~10^{15}), and efforts immediately turned to proving the existence of SMSERS[8-10] and characterizing the nanostructures that gave rise to such massive enhancements.[11-14] More than 15 years later it has become widely accepted that electromagnetic hot spots play a major role in SMSERS. In the electromagnetic mechanism (EM) of SERS, excitation of the LSPR in a plasmonic nanostructured material leads to a significant electric field enhancement (EFE) at the particle surface, and the Raman cross section of molecules in this enhanced field can be increased by several orders of magnitude.[5, 15] Electromagnetic enhancements of 10^{10} - 10^{11} at the junction between two closely spaced metallic particles (hot spots) have been predicted,[14, 16-17] and the maximum achievable enhancements are moderately reduced when quantum effects are taken into account.[18] Also, studies have shown that more modest enhancement factors (on the order of 10^{7}-10^{8}) are sufficient to observe a single molecule in SERS for a resonant molecule such as R6G.[19]

While the idea of electromagnetic hot spots in SERS is well-known,[20-21] Brus and co-workers[22-24] showed using polarization studies that hot spots formed at the junction of two nanoparticles likely play a major role in SMSERS. This claim was further supported by atomic force microscopy showing that SMSERS-active structures are aggregates of Ag nanoparticles. A study correlating high-resolution transmission electron microscopy (HRTEM), SMSERS, and LSPR showed that multiple aggregate nanostructures ~100 nm in size, were suitable for observing SMSERS and continuum electrodynamics calculations on the simplest SMSERS-active aggregates, also

confirmed that the hot spot was located near the interparticle junctions.[25-26] Wustholz et al. [27] demonstrated that the EFE can reach its maximum when two particles are in subnanometer proximity or have coalesced to form crevices. Studies performing high-resolution two dimensional (2D) imaging of SMSERS hot spots, measured the spatial distribution of the SMSERS centroid position and the SERS intensity,[28-29] and these studies were later expanded to include images of the aggregates.[30] A recent theoretical investigation of the spatial, spectral and polarization dependence of the electromagnetic SMSERS-active hot spots showed that high electromagnetic field strength can be produced at multiple *spectral* and *spatial* locations.[26] This study further demonstrated that some hot spots exist due to the collective and phase-uniform excitation of LSPR, while others originate from interfering plasmonic excitations resulting from scattering from gaps and surfaces.

Despite the large body of evidence in favor of electromagnetic hot spots, only now have techniques emerged that can image plasmons with the spatial (<1 nm) and energy resolutions (0.1 - 0.3 eV) necessary to observe the elusive electromagnetic hot spots, which are thought to be essential for SMSERS. One such technique is electron-energy loss spectroscopy (EELS) in a scanning transmission electron microscope (STEM).[31-40] The power of this technique is derived from its ability to experimentally render the photonic local density of states (LDOS). Using a Green's function approach, Garcia de Abajo and Kociak[41] concluded that "the energy loss probability is directly related to the local density of states in arbitrary systems". Numerical simulations support this conclusion and they further emphasize the correspondence between the

projection of the LDOS onto the electron trajectory and the EELS signal.[41] Hohenester, Ditlbacher, and Krenn[42] considered this same question and instead concluded that "there exists no clear-cut relation between EELS and LDOS".[42] They further examined coupled, flat metallic nanostructures and state that EELS can "be blind to the hot spots in the gap region between particles." These theoretical studies focused on structures which are quasi-planar, and it is not clear to what extent the results apply to the complex 3D nanoaggregates encountered in SMSERS, where the imaging of hot spots takes on primary importance. Previous experimental studies have examined (mostly planar) coupled nanoparticle structures,[31-33, 36-37] although none of them were known to be SMSERS-active.

Herein, we present the first STEM/EELS imaging study of plasmon modes in nanostructures *confirmed* to be SMSERS-active. Our STEM/EELS studies do *not* show an enhanced EEL in the gap regions between nanoparticles, where one would expect the electromagnetic hot spots to be located. Further, we support our experimental findings with a fully three-dimensional electrodynamics simulation of both the near-electric field enhancement (hot spot) and EELS loss probability, for the exact nanoparticle geometry obtained from the experiment. The simulations are in full agreement with the experimental results and yield insights into the specific EEL signatures associated with hot spots.

In our experiment, SMSERS active clusters were identified using the bi-analyte approach,[10, 43] which relies on two isotopologues of Rhodamine 6G,[8] R6G-d_0 and R6G-d_4. Briefly, Ag nanoparticles were treated with a low concentration of the mixture of

R6G-d_0 and R6G-d_4 (ca. 10^{-9} M) such that approximately one R6G molecule, either R6G-d_0 or R6G-d_4 was adsorbed per active site according to the Poisson distribution[8] (see Appendix for Chapter II, Figure 14). Many SMSERS active aggregates were analyzed with our correlated STEM/EELS/optical approach to ensure a representative data set. Figure 10 presents correlated annular dark field (ADF) images and optical spectra of two representative nanostructures confirmed to be SMSERS-active. In good agreement with previous HRTEM studies,[25] our structures consist of number of nanoparticles with varying degrees of contact. These contact regions, which we call "junctions", arise from coalesced or closely spaced structures and are thought to support electromagnetic hot spots. Figure 10 also displays the Raman spectra, without baseline or background correction, and the resonance-Rayleigh scattering measurements of the two SMSERS-active particles. As previous studies have indicated, there is no correlation between the SERS enhancement factor and the LSPR maximum.[23, 25]

When preparing SMSERS active nanoclusters via aggregation, only a few percent of the total aggregates are found to be active.[7] This small population of active aggregates is due, in part, to the low analyte concentrations required to ensure single molecule character; however, it is additionally assumed that only "special" aggregates generate an electromagnetic hot spot on resonance with the excitation laser. In this picture, these "special" aggregates lead to the strongest SMSERS signal; although, theoretical studies[26] have cautioned that one aggregate may have multiple hot spots and that the maximum electromagnetic enhancement may be a weak function of the

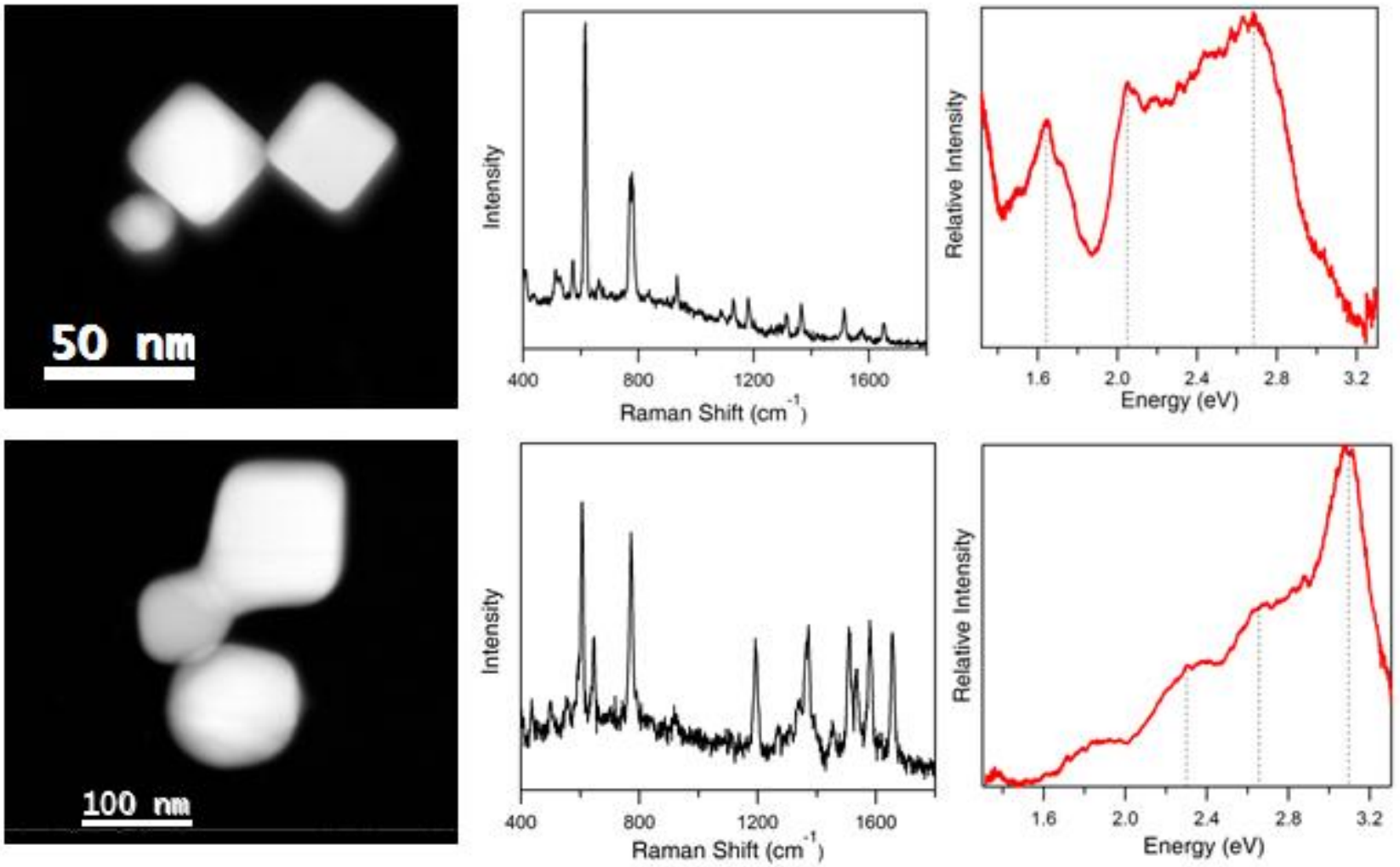

Figure 10. Annular dark field (ADF) images (left), Raman scattering (middle), and resonance-Rayleigh (right) scattering spectra of two SMSERS active trimer structures. Single molecule character was confirmed using the isotopologue method.

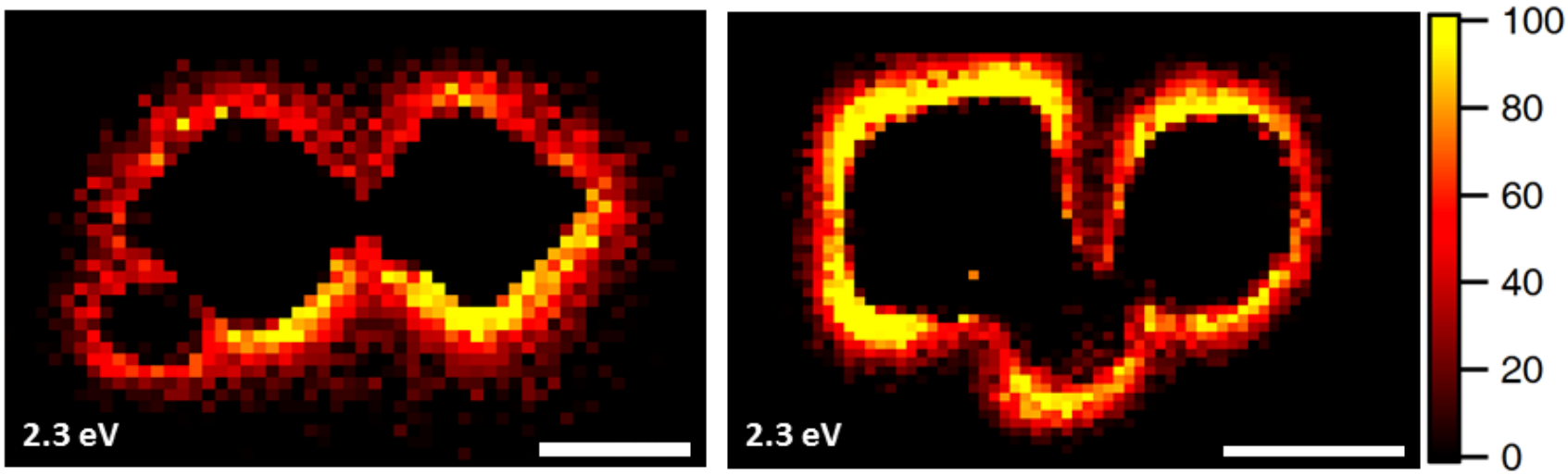

Figure 11. Spatially resolved electron-energy-loss (EEL) maps for a loss energy of 2.3 eV for SMSERS active trimers. Images have been normalized to the zero-loss peak (ZLP). A complete EEL spectrum is obtained for every pixel in the region of interest (defined by the ADF in Figure 10); however, we focus on the loss energy of 2.3 eV as this corresponds to the energy of the Raman laser (532 nm, 2.3 eV) used in the SMSERS experiment. (Images for other loss features are available in the Appendix for Chapter II.) While it is assumed that the largest electromagnetic enhancement is obtained at the gap region, no localization of the EEL intensity is observed in the gaps. Scale bars are 50 nm (left) and 100 nm (right).

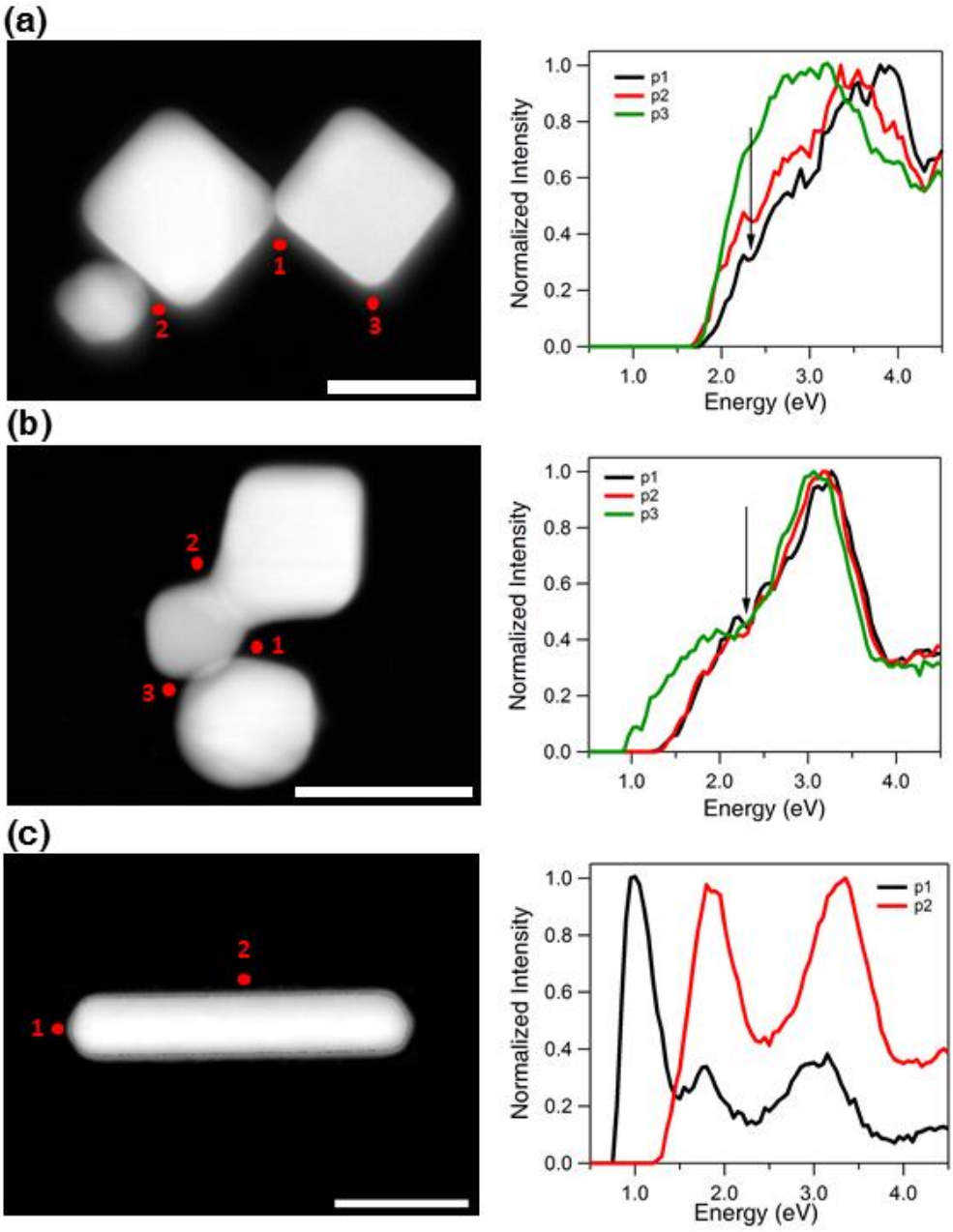

Figure 12. ADF images (left) and electron-energy-loss (EEL) spectra (right) for selected points around the SMSERS active structures (a, b). For comparison the EEL spectra and ADF images of a nanorod are adapted from Reference 35. The energy of the laser line used in our experiment (532 nm≈2.3 eV) is indicated with an arrow in the graphs. The spectra have been normalized so the highest point is 1. Scale bars are 50 nm (a), 100 nm (b), and 50 nm (c).

Figure 13. (a) Comparison of the calculated electric near-field magnitude obtained from plane wave excitation (left) with the EEL probability map for a 100 keV electron beam (right) for the SMSERS active trimer displayed in Figure 1. Simulation of the plane wave excitation is performed via the DDA at a wavelength of 532 nm. The wave vector of the excitation field is directed along the z-axis and is polarized along the x-axis. The two-dimensional slice displayed corresponds to the plane where the electric-field magnitude is maximized. Other polarizations, wave-vector directions, and projection planes were examined and show similar localization of the field in the junction regions. The loss-probability map, computed via the *e*-DDA, is displayed at a corresponding loss-energy of 2.3 eV. In agreement with the experiment, the EEL map does not show an intense loss probability in the junction region. (b) Induced polarization maps (2.3 eV) obtained for two different positions of the electron beam (green bullet). Placement of the electron beam in the junction leads to a net anti-bonding arrangement of dipoles (right), whereas placement of the electron beam on the outside right corner leads to a net bonding arrangement (left). Also shown is the induced polarization (red vectors) and resulting scattered electric field (blue vectors), both normalized to unity to aid visualization. Both panels display two-dimensional slices taken from fully three-dimensional simulations of the trimer. The plane of visualization was chosen to lie at the height of the centroid of the two cubes.

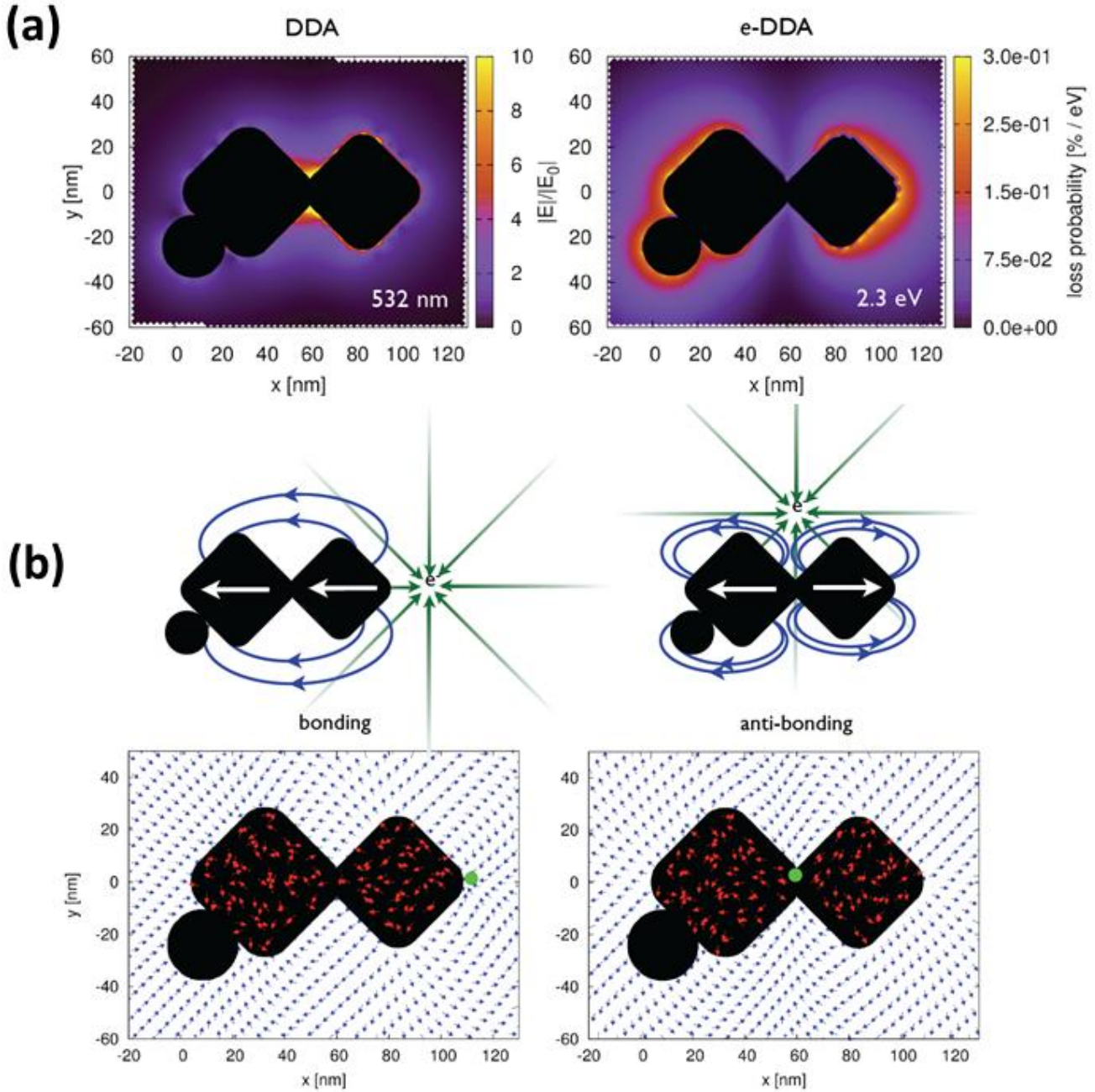
(a)
DDA
e-DDA
532 nm
2.3 eV
y [nm]
x [nm]
|E|/|E0|
loss probability [% / eV]
(b)
e
bonding
anti-bonding

laser excitation energy. To examine the possibility of an electromagnetic hot spot at the energy of our resonance-Raman experiments (532 nm, 2.3 eV) we plot, in Figure 11, the spatially resolved intensity corresponding to an electron-energy-loss of 2.3 eV for the structures shown in Figure 10. We emphasize that the image obtained in Figure 11 is not dependent on the EELS data processing method. Raw energy slices of EEL (spectra after centering, normalizing to the zero loss peak (ZLP), and subtracting the ZLP), and plasmon modes extracted using the Automated eXpert Spectral Image Analysis (AXSIA) program, are similar to those presented in Figure 2 (See Appendix for Chapter II Figures 15b, 16b, 17c, 18b). These results demonstrate that there is no localization of the EEL intensity in the gaps at 2.3 eV, even at the junctions between the particles.

We have also extracted EEL spectra from the gap regions and display them in Figure 12. This allows us to probe resonances occurring at energies *different* from the excitation laser, e.g. an exceptionally bright aggregate may yield SMSERS activity, even when the laser is off resonance from the hot spot. As evident from Figures 12a and b, we do not observe any sharp resonance for either trimer at the points located between the nanoparticles. One might object that the energy resolution of the current experiment (~0.5 eV) is insufficient to resolve some of the modes (e.g. modes corresponding to the gap between the nanoparticles); therefore, for a comparison, we have also included in Figure 12 EELS data for a nanorod adapted from our previously published work.[35] For the nanorod, we observe well-resolved (spatial and spectral) plasmon resonances.

While it is well known that extreme near-electric-field enhancements can be obtained at locations near sharp surface protrusions or in nanogaps,[14, 16-17] our EELS results do not show a clear localization of the EEL intensity at the junction of two nanoparticles. In order to examine this observation in detail we employ a modified version of the discrete dipole approximation (DDA), called *electron-driven DDA* (*e*-DDA),[44] which imposes the electric field of a swift electron,[45-46]

$$\mathbf{E}\ \mathbf{x},\omega\ = \frac{2e\omega}{\upsilon^2\epsilon\gamma}\ e^{i\omega z\ \upsilon}\ \frac{i}{\gamma}K_0\ \frac{\omega b}{\upsilon\gamma}\ \mathbf{v} - K_1\ \frac{\omega b}{\upsilon\gamma}\ \mathbf{b}$$

rather than a plane wave upon a fully three-dimensional target located a distance

$$\mathbf{x}\ =\ \overline{\mathbf{b}^{\ 2} + \mathrm{z}^2}$$

away from the direction of propagation. In this expression $\mathbf{v}$ is the speed of the electron, chosen to propagate along the z axis,

$$\gamma = \frac{1}{\overline{1 - \epsilon\ \frac{\mathrm{v}}{\mathrm{c}}^{\ 2}}}$$

and K_0 and K_1 are modified Bessel functions. As in the DDA, the target is discretized into a finite collection of polarizable points that are each driven by the field of the electron, Eq 1, and by the electric-dipole field of all other target points. Each point is described by a linear polarizability that depends upon the complex-valued and frequency-dependent dielectric function of the bulk material.[47] When the electron beam is positioned near the target, the EEL spectra at each position **b** can be computed from the loss probability per unit frequency,[34, 48]

$$P_{\mathbf{b}}\ \omega\ = \frac{1}{\pi\hbar}\mathrm{Im}\ \ \sum_{j=1}^{N}\mathbf{E}^*\ \mathbf{x}_j,\omega\ \cdot\mathbf{P}_j\ \omega$$

where $\mathbf{P}_j$ is the dipole moment of *j*th target dipole and **E** is the electric field of the swift electron evaluated at position *j*. Further details of the theoretical methods are available in SI and an in depth comparison of e-DDA calculations with experimental STEM/EELS measurements are the subject of a companion manuscript.[44]

Figure 13(a) compares the calculated electric near-field magnitude, obtained from plane wave excitation (DDA), and the energy-loss-probability map, obtained from a 100 keV electron beam (*e*-DDA). The calculation in both cases is performed at an energy of 2.3 eV corresponding to excitation with 532 nm light or a 2.3 eV energy loss from the electron beam.

The calculated loss-probability map (Figure 13a, right panel) compares well with the experiment (Figure 11) although small differences are observed, likely due to the complex nature of the nanoaggregates, imperfect reconstruction of the experimental ADF image to an array of dipoles, and variations in the local environment of the aggregate. Even though this structure is predicted to have an intense electromagnetic hot spot in the junction region under plane wave excitation (Figure 13a, left panel), and is known to be SMSERS active, a strong EEL probability in the junction region at 532 nm is *not* observed in *either* the STEM/EELS experiment or the e-DDA theory. We do, however, observe strong loss features at points *external* to the junctions (Figure 13).

Insight into these features can be explored by computing the polarization induced in the target at 2.3 eV for different electron-beam positions (Figure 13b). Our analysis suggests that the planar model of bonding and anti-bonding dipoles[42] is applicable to the more complex geometries observed in SMSERS. When the electron beam is

positioned in the junction, the calculations show that a net *anti-bonding* arrangement of the target's polarization vectors is induced. This leads to a node of the scattered electric field in the junction and a small loss probability results. When the electron beam is positioned on the right side of the nanoaggregate, a net *bonding* arrangement of the induced polarization vectors is obtained. This underlies a capacitive electric field that is localized in the junction and is characteristic of an electromagnetic hot spot. In fact, we show in a related paper that the electron-induced junction field and the hot spot set up by plane wave excitation are directionally identical.[44]

Both of these arrangements of the target's electronic polarization are due to the forces exerted by the polarization of the electric field of the swift electron. Interestingly, this means that the electromagnetic hot spot can indeed be excited by the electron beam, and that it is in principle possible to induce Raman scattering from the single molecule with the electron beam.

We present, for the first time, plasmon maps of SMSERS-active nanoparticles employing STEM/EELS. Although it is widely accepted that electromagnetic hot spots are responsible for SMSERS activity, and are located between the gaps of nanoparticles, we do *not* see a large EEL intensity in these regions. We have rigorously confirmed that each structure examined indeed gives rise to SMSERS before EELS imaging. Our experimental results are complemented with fully three-dimensional simulation that builds the electron-beam excitation directly into the DDA and utilize shape parameters derived from the experiment. The simulations are in good agreement with the experimental results and yields insights into the specific EEL signatures

associated with hot spots. In other words, the electromagnetic hot spot can be excited when the electron beam is positioned at the periphery of the nanoaggregate. With the rapid emergence of STEM/EELS as a tool for probing the plasmonic properties of nanostructures, we believe the work presented here will impact a wide range of STEM/EELS plasmon imaging experiments going forward.

References for Chapter II

(1) Albrecht, M. G.; Creighton, J. A., Anomalously Intense Raman-Spectra of Pyridine at a Silver Electrode. *J. Am. Chem. Soc.* **1977,** *99* (15), 5215-5217.

(2) Fleischman.M; Hendra, P. J.; McQuilla.Aj, Raman-Spectra of Pyridine Adsorbed at a Silver Electrode. *Chemical Physics Letters* **1974,** *26* (2), 163-166.

(3) Jeanmaire, D. L.; Van Duyne, R. P., Surface Raman Spectroelectrochemistry .1. Heterocyclic, Aromatic, and Aliphatic-Amines Adsorbed on Anodized Silver Electrode. *J. Electroanal. Chem.* **1977,** *84* (1), 1-20.

(4) Maier, S. A.; Brongersma, M. L.; Kik, P. G.; Meltzer, S.; Requicha, A. A. G.; Atwater, H. A., Plasmonics - a Route to Nanoscale Optical Devices. *Adv. Mater.* **2001,** *13* (19), 1501-+.

(5) Moskovits, M., Surface-Ehanced Spectroscopy. *Rev. Mod. Phys.* **1985,** *57* (3), 783-826.

(6) Kneipp, K.; Wang, Y.; Kneipp, H.; Perelman, L. T.; Itzkan, I.; Dasari, R.; Feld, M. S., Single Molecule Detection Using Surface-Enhanced Raman Scattering (Sers). *Phys. Rev. Lett.* **1997,** *78* (9), 1667-1670.

(7) Nie, S. M.; Emery, S. R., Probing Single Molecules and Single Nanoparticles by Surface-Enhanced Raman Scattering. *Science* **1997,** *275* (5303), 1102-1106.

(8) Dieringer, J. A.; Lettan, R. B.; Scheidt, K. A.; Van Duyne, R. P., A Frequency Domain Existence Proof of Single-Molecule Surface-Enhanced Raman Spectroscopy. *J. Am. Chem. Soc.* **2007,** *129* (51), 16249-16256.

(9) Etchegoin, P. G.; Le Ru, E. C., A Perspective on Single Molecule Sers: Current Status and Future Challenges. *Phys. Chem. Chem. Phys.* **2008,** *10* (40), 6079-6089.

(10) Le Ru, E. C.; Meyer, M.; Etchegoin, P. G., Proof of Single-Molecule Sensitivity in Surface Enhanced Raman Scattering (Sers) by Means of a Two-Analyte Technique. *J. Phys. Chem. B* **2006,** *110* (4), 1944-1948.

(11) Fan, M.; Andrade, G. F. S.; Brolo, A. G., A Review on the Fabrication of Substrates for Surface Enhanced Raman Spectroscopy and Their Applications in Analytical Chemistry. *Analytica Chimica Acta* **2011,** *693* (1–2), 7-25.

(12) Jensen, T. R.; Malinsky, M. D.; Haynes, C. L.; Van Duyne, R. P., Nanosphere Lithography: Tunable Localized Surface Plasmon Resonance Spectra of Silver Nanoparticles. *The Journal of Physical Chemistry B* **2000,** *104* (45), 10549-10556.

(13) Petryayeva, E.; Krull, U. J., Localized Surface Plasmon Resonance: Nanostructures, Bioassays and Biosensing—a Review. *Analytica Chimica Acta* **2011,** *706* (1), 8-24.

(14) Xu, H. X.; Aizpurua, J.; Kall, M.; Apell, P., Electromagnetic Contributions to Single-Molecule Sensitivity in Surface-Enhanced Raman Scattering. *Phys. Rev. E* **2000,** *62* (3), 4318-4324.

(15) Schatz, G. C.; Van Duyne, R. P., Electromagnetic Mechanism of Surface-Enhanced Spectroscopy. In *Handbook of Vibrational Spectroscopy*, Chalmers, J. M.; Griffiths, P. R., Eds. John Wiley & Sons Ltd: 2002.

(16) Johansson, P.; Xu, H.; Käll, M., Surface-Enhanced Raman Scattering and Fluorescence near Metal Nanoparticles. *Phys. Rev. B* **2005,** *72* (3), 035427.

(17) Le Ru, E.; Etchegoin, P.; Meyer, M., Enhancement Factor Distribution around a Single Surface-Enhanced Raman Scattering Hot Spot and Its Relation to Single Molecule Detection. *The Journal of chemical physics* **2006,** *125*, 204701.

(18) Marinica, D. C.; Kazansky, A. K.; Nordlander, P.; Aizpurua, J.; Borisov, A. G., Quantum Plasmonics: Nonlinear Effects in the Field Enhancement of a Plasmonic Nanoparticle Dimer. *Nano Lett.* **2012,** *12* (3), 1333-1339.

(19) Le Ru, E. C.; Blackie, E.; Meyer, M.; Etchegoin, P. G., Surface Enhanced Raman Scattering Enhancement Factors: A Comprehensive Study. *J. Phys. Chem. C* **2007,** *111* (37), 13794-13803.

(20) Gersten, J.; Nitzan, A., Electromagnetic Theory of Enhanced Raman-Scattering by Molecules Adsorbed on Rough Surfaces. *J. Chem. Phys.* **1980,** *73* (7), 3023-3037.

(21) Metiu, H., Surface Enhanced Spectroscopy. *Progress in Surface Science* **1984,** *17* (3-4), 153-320.

(22) Maier, S. A., Plasmonics: The Promise of Highly Integrated Optical Devices. *Ieee Journal of Selected Topics in Quantum Electronics* **2006,** *12* (6), 1671-1677.

(23) Michaels, A. M.; Jiang, J.; Brus, L., Ag Nanocrystal Junctions as the Site for Surface-Enhanced Raman Scattering of Single Rhodamine 6g Molecules. *J. Phys. Chem. B* **2000,** *104* (50), 11965-11971.

(24) Michaels, A. M.; Nirmal, M.; Brus, L. E., Surface Enhanced Raman Spectroscopy of Individual Rhodamine 6g Molecules on Large Ag Nanocrystals. *J. Am. Chem. Soc.* **1999,** *121* (43), 9932-9939.

(25) Camden, J. P.; Dieringer, J. A.; Wang, Y. M.; Masiello, D. J.; Marks, L. D.; Schatz, G. C.; Van Duyne, R. P., Probing the Structure of Single-Molecule Surface-Enhanced Raman Scattering Hot Spots. *J. Am. Chem. Soc.* **2008,** *130* (38), 12616-12617.

(26) Litz, J. P.; Camden, J. P.; Masiello, D. J., Spatial, Spectral, and Coherence Mapping of Single-Molecule Sers Active Hot Spots Via the Discrete-Dipole Approximation. *J. Phys. Chem. Lett.* **2011,** *2* (14), 1695-1700.

(27) Wustholz, K. L.; Henry, A.-I.; McMahon, J. M.; Freeman, R. G.; Valley, N.; Piotti, M. E.; Natan, M. J.; Schatz, G. C.; Van Duyne, R. P., Structure-Activity Relationships in Gold Nanoparticle Dimers and Trimers for Surface-Enhanced Raman Spectroscopy. *J. Am. Chem. Soc.* **2010,** *132* (31), 10903-10910.

(28) Cang, H.; Labno, A.; Lu, C. G.; Yin, X. B.; Liu, M.; Gladden, C.; Liu, Y. M.; Zhang, X., Probing the Electromagnetic Field of a 15-Nanometre Hotspot by Single Molecule Imaging. *Nature* **2011,** *469* (7330), 385-389.

(29) Stranahan, S. M.; Willets, K. A., Super-Resolution Optical Imaging of Single-Molecule Sers Hot Spots. *Nano Lett.* **2010,** *10* (9), 3777-3784.

(30) Willets, K. A.; Stranahan, S. M.; Weber, M. L., Shedding Light on Surface-Enhanced Raman Scattering Hot Spots through Single-Molecule Super-Resolution Imaging. *J. Phys. Chem. Lett.* **2012,** *3* (10), 1286-1294.

(31) Bosman, M.; Keast, V. J.; Watanabe, M.; Maaroof, A. I.; Cortie, M. B., Mapping Surface Plasmons at the Nanometre Scale with an Electron Beam. *Nanotechnology* **2007,** *18* (16), 165505.

(32) Chu, M. W.; Myroshnychenko, V.; Chen, C. H.; Deng, J. P.; Mou, C. Y.; de Abajo, F. J. G., Probing Bright and Dark Surface-Plasmon Modes in Individual and Coupled Noble Metal Nanoparticles Using an Electron Beam. *Nano Lett.* **2009,** *9* (1), 399-404.

(33) Duan, H. G.; Fernandez-Dominguez, A. I.; Bosman, M.; Maier, S. A.; Yang, J. K. W., Nanoplasmonics: Classical Down to the Nanometer Scale. *Nano Lett.* **2012,** *12* (3), 1683-1689.

(34) Garcia de Abajo, F. J., Optical Excitations in Electron Microscopy. *Rev. Mod. Phys.* **2010,** *82* (1), 209-275.

(35) Guiton, B. S.; Iberi, V.; Li, S.; Leonard, D. N.; Parish, C. M.; Kotula, P. G.; Varela, M.; Schatz, G. C.; Pennycook, S. J.; Camden, J. P., Correlated Optical Measurements and Plasmon Mapping of Silver Nanorods. *Nano Lett.* **2011,** *11* (8), 3482-3488.

(36) Koh, A. L.; Bao, K.; Khan, I.; Smith, W. E.; Kothleitner, G.; Nordlander, P.; Maier, S. A.; McComb, D. W., Electron Energy-Loss Spectroscopy (Eels) of Surface Plasmons in Single Silver Nanoparticles and Dimers: Influence of Beam Damage and Mapping of Dark Modes. *ACS Nano* **2009,** *3* (10), 3015-3022.

(37) Koh, A. L.; Fernandez-Dominguez, A. I.; McComb, D. W.; Maier, S. A.; Yang, J. K. W., High-Resolution Mapping of Electron-Beam-Excited Plasmon Modes in Lithographically Defined Gold Nanostructures. *Nano Lett.* **2011,** *11* (3), 1323-1330.

(38) Nelayah, J.; Kociak, M.; Stephan, O.; de Abajo, F. J. G.; Tence, M.; Henrard, L.; Taverna, D.; Pastoriza-Santos, I.; Liz-Marzan, L. M.; Colliex, C., Mapping Surface Plasmons on a Single Metallic Nanoparticle. *Nat. Phys.* **2007,** *3* (5), 348-353.

(39) Nicoletti, O.; Wubs, M.; Mortensen, N. A.; Sigle, W.; van Aken, P. A.; Midgley, P. A., Surface Plasmon Modes of a Single Silver Nanorod: An Electron Energy Loss Study. *Opt. Express* **2011,** *19* (16), 15371-15379.

(40) Scholl, J. A.; Koh, A. L.; Dionne, J. A., Quantum Plasmon Resonances of Individual Metallic Nanoparticles. *Nature* **2012,** *483* (7390), 421-U68.

(41) de Abajo, F. J. G.; Kociak, M., Probing the Photonic Local Density of States with Electron Energy Loss Spectroscopy. *Phys. Rev. Lett.* **2008,** *100* (10).

(42) Hohenester, U.; Ditlbacher, H.; Krenn, J. R., Electron-Energy-Loss Spectra of Plasmonic Nanoparticles. *Phys. Rev. Lett.* **2009,** *103* (10).

(43) Etchegoin, P. G.; Meyer, M.; Blackie, E.; Le Ru, E. C., Statistics of Single-Molecule Surface Enhanced Raman Scattering Signals: Fluctuation Analysis with Multiple Analyte Techniques. *Anal. Chem.* **2007,** *79* (21), 8411-8415.

(44) Bigelow, N. W.; Vaschillo, A.; Iberi, V.; Camden, J. P.; Masiello, D. J., Characterization of the Electron- and Photon-Driven Plasmonic Excitations of Metal Nanorods. *ACS Nano* **2012,** *6* (8), 7497-7504.

(45) Ritchie, R. H.; Howie, A., Electron Excitation and the Optical Potential in Electron Microscopy. *Philosophical Magazine* **1977,** *36* (2), 463-481.

(46) Rose, H., Image Formation by Inelastically Scattered Electrons in Electron Microscopy. *Optik* **1976,** *45* (2), 139-158.

(47) Lynch, D. W. H., W. R. , *Handbook of Optical Constants of Solids*. Academic Press: New York, 1985.

(48) Muller, D. A.; Silcox, J., Delocalization in Inelastic Scattering. *Ultramicroscopy* **1995,** *59* (1–4), 195-213.

Appendix for Chapter II

I. Experimental Methods

R6G-d_4 was synthesized according to the procedure described by Blackie and co-workers,[1] with NMR and mass spectrometry data of the resulting compound matching this prior report. Ag nanoparticles were treated with a low concentration of the mixture of R6G-d_0 and R6G-d_4 (ca. 10^{-9} M) such that approximately one R6G molecule, either R6G-d_0 or R6G-d_4 was adsorbed per active site according to the Poisson distribution[2] (Figure 14). Silver nanoparticles were obtained from nanoComposix and used without further purification. In our experiment, no salt was added to the SMSERS solution since previous nanoparticle studies had demonstrated the existence of sufficient aggregations and for the purpose of this study simpler structures with not many overlapping nanostructures are desired. 200 mesh Cu grids coated with holey carbon (SPI supplies #3540C-FA) were used as TEM supports. A 3 µL aliquot of the SMSERS solution was drop-coated directly onto the TEM grid and the solvent was allowed to evaporate. After deposition, the sample was placed on a coverslip, mounted in a custom-designed sample holder and purged with dry nitrogen. For the Raman scattering, the sample was irradiated with 532 nm linearly polarized laser light (Spectra Physics, model J-20) at grazing incidence with a power density of ~0.03 W/cm^2. Optical measurements were carried out on an inverted microscope (Nikon, T*i*-U) equipped with a dark-field condenser (Nikon, NA= 0.95-0.80) and an ultra-steep Raman long-pass edge filter (Semrock) to block the laser Rayleigh line. Raman spectra were collected using a 100X (Nikon, 0.7<NA<1.4, oil immersion) objective and detected on a liquid

nitrogen-cooled back-illuminated charge couple detector (CCD) (Princeton Instruments, PIXIS 100). Resonance-Rayleigh scattering measurements were performed on the SMSERS-active nanoparticles after removing the long-pass edge filter utilizing the unpolarized light output of a tungsten-halogen lamp. A wide-field image of the silver nanoparticles on the TEM grid was also recorded to serve as a map for subsequent characterization in the STEM. This method enabled correlated optical and STEM measurements of the exact same SMSERS-active nanostructures with an average of 15 active clusters per grid.

After identification and optical characterization of active SMSERS nanoparticles, the sample was inserted into an aberration-corrected, cold-field-emission STEM (VG Microscopes HB501UX STEM with Nion aberration corrector and Gatan Enfina EEL spectrometer). The SMSERS-active nanoparticles were found by comparing the dark-field optical map to the pattern of particles visible in the STEM at very low resolution.[3] After identification, a high resolution ADF image and an EEL spectrum image were collected from the ZLP containing region, i.e., an EEL spectrum is recorded at each pixel over the entire region of interest. The spectrometer dispersion was set to 0.05 eV per channel with an exposure time of 0.05 s per spectrum. The pixel size/density (60 × 37 pixels for Figure 2, left and 57 × 76 pixels for Figure 11, right) was chosen to give a total acquisition time of around 11 minutes for a single spectrum image. Shorter acquisition times were used to avoid accumulation of contaminations caused by the electron beam. The energy resolution, determined by the full-width-half-maximum of the ZLP, was ~0.5-0.55 eV. The STEM/EELS data were analyzed using three different

approaches; in the first approach, the raw EELS data were examined after centering the ZLP of each spectrum at 0eV, normalizing to the ZLP, and subtracting the ZLP, leaving only the inelastic contributions to the spectrum image. In the second approach, for a particular pixel of interest, the complete EEL spectra, after centering and subtracting the ZLP, were background subtracted and plotted for different probe positions on the entire structure. In a third and final approach, multivariate statistical analysis employing AXSIA program,[4-5] was applied to the data to extract statistically significant component spectra and maps; details of this analysis have been discussed in our previously published work.[6] The data analysis using AXSIA is presented in SI. Our experimental measurements are also supported by electrodynamics simulations based on the DDA,[7-8] and the details are presented in the SI.

II. Simulation Methods

Discrete Dipole Approximation (DDA) calculations[7-8] were utilized to examine the electromagnetic-field properties of the trimer aggregate shown in the Figure 10a of the manuscript. In the DDA the target is discretized into a collection of polarizable points, each induced by its interaction with an incident plane wave and with fields arising from the other polarizable elements. Structural parameters for the SMSERS-active nanostructures, such as the edge length, corner rounding (radius of curvature), and the gaps between the nanoparticles were obtained from the experimental annular dark field (ADF) image and were used to build the dipole array. These fields are calculated half a grid spacing from the surface, instead of immediately on the surface, in order to avoid

numerical instabilities that arise at the surface. The grid spacing used was 2 nm, the dielectric constants of silver were from Palik,[9] and the effective medium approximation of 1.35 was employed to include the substrate effect implicitly. The effective medium approximation is a well-documented method to include the effects of substrate and the environment of the nanoparticles and defines an average dielectric function to describe the optical response of the entire aggregate.[10] Simulation of the plane wave excitation is performed at a wavelength of 532 nm. The wave vector of the excitation field is directed along the z-axis and is polarized along the x-axis. The two-dimensional slice displayed corresponds to the plane where the electric-field magnitude is maximized. Other polarizations, wave-vector directions, and projection planes were examined and show similar localization of the field in the junction regions. The loss-probability map, computed via the *e*-DDA, is displayed at a corresponding loss-energy of 2.3 eV. In agreement with the experiment, the EEL map does not show an intense loss probability in the junction region.

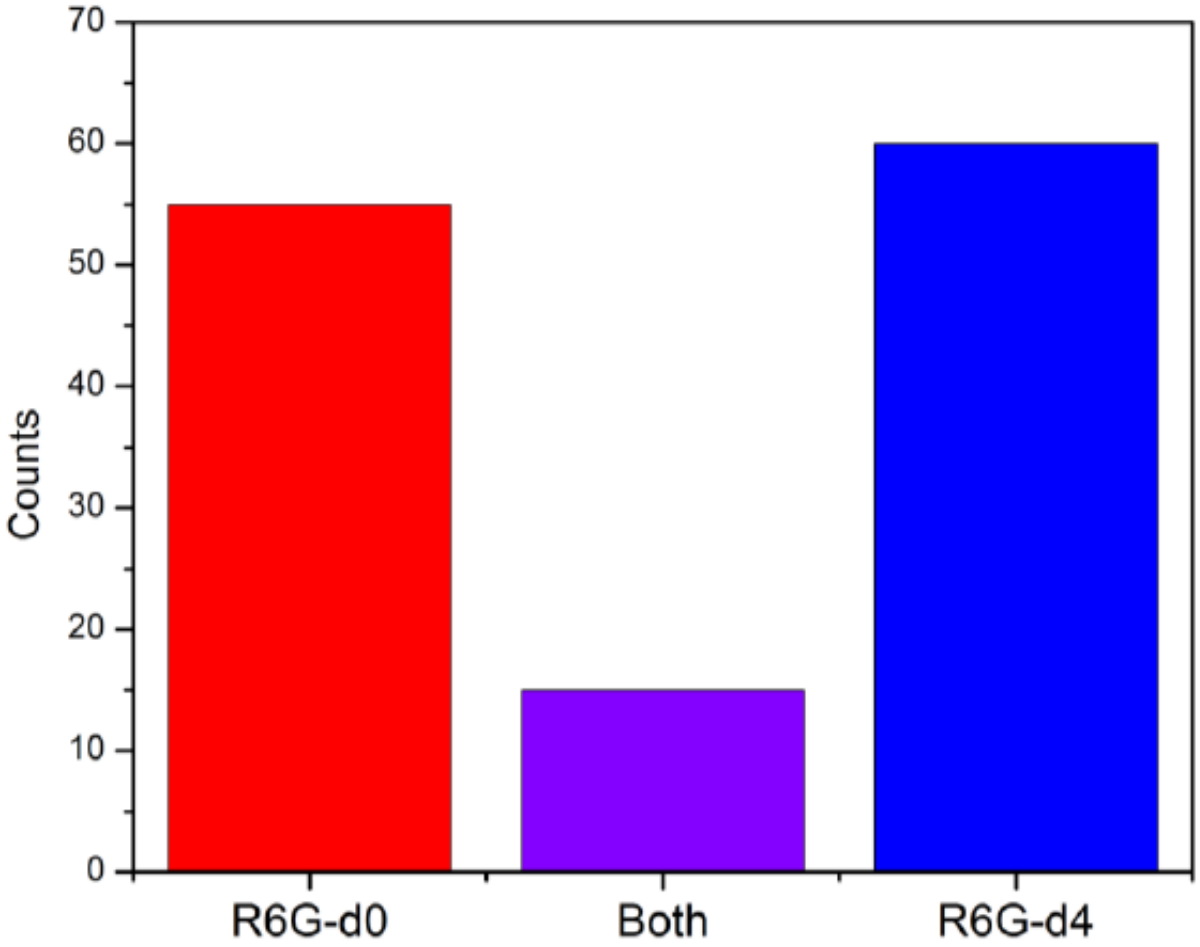

Figure 14. Histogram showing the frequency with which only R6G-d_0 (red), only R6G-d_4 (blue) and both R6G-d_0 and R6G-d_4 (purple) vibrational modes were observed. Nanoparticles were treated with a low concentration of the mixture of R6G-d_0 and R6G-d_4 (ca. 10^{-9} M) such that approximately one R6G molecule, either R6G-d_0 or R6G-d_4 was adsorbed per active site according to the Poisson distribution.

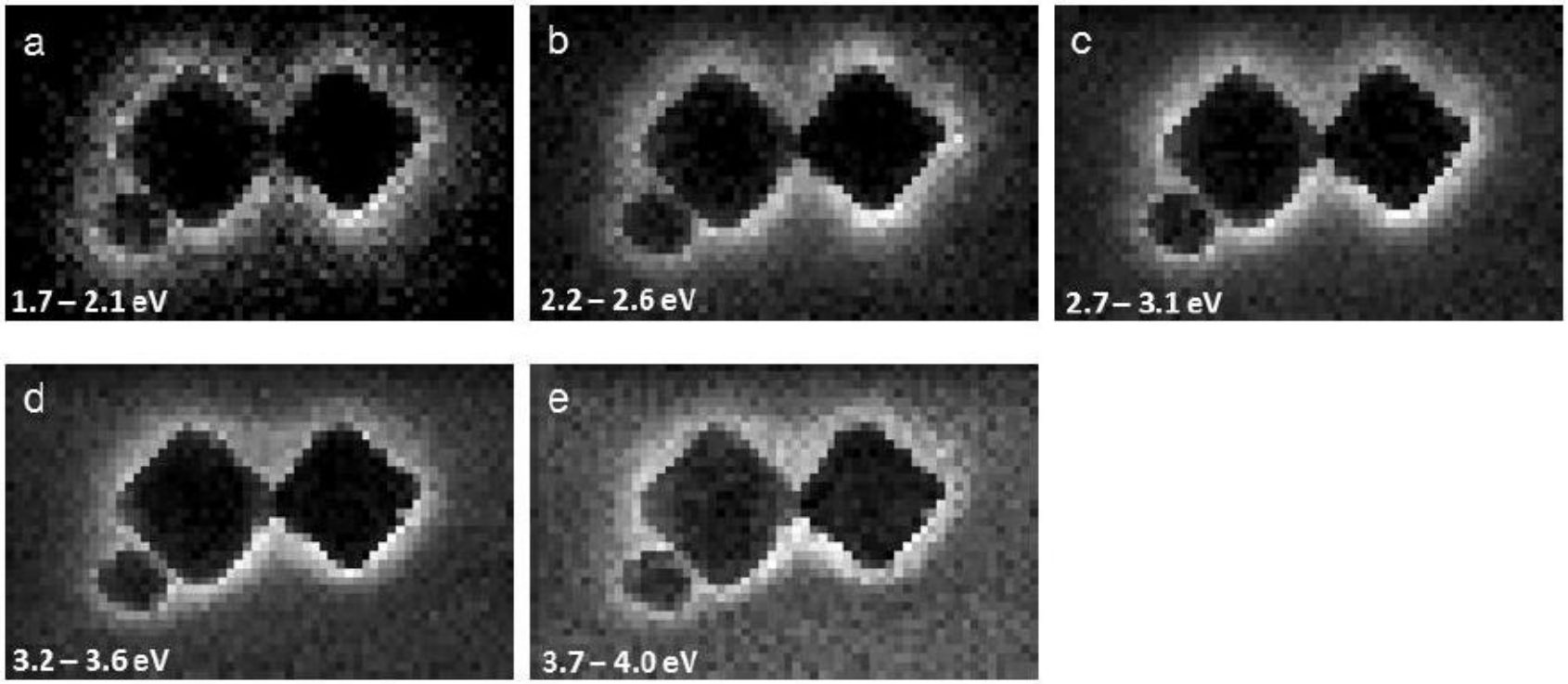

Figure 15. Energy slices from the spectrum image of trimer, *after* centering, normalizing to zero-loss peak (ZLP) and subtracting ZLP, but *before* noise reduction with principal components analysis.

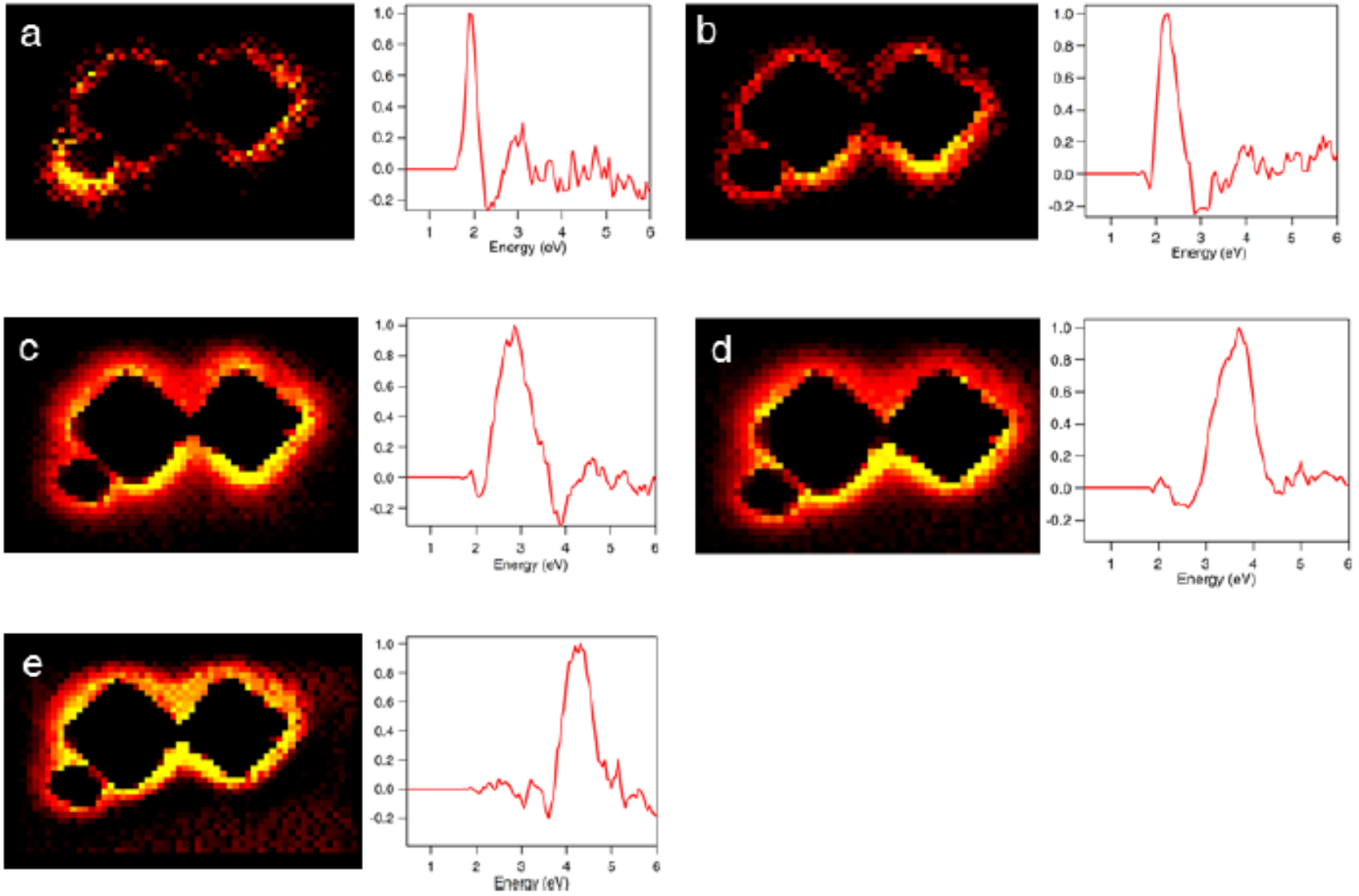

Figure 16. Plasmon maps and loading spectra of SMSERS-active nanostructures using AXSIA. Multivariate statistical analysis (MVSA) employing the AXSIA program, was applied to the data to extract statistically significant component spectra and maps.

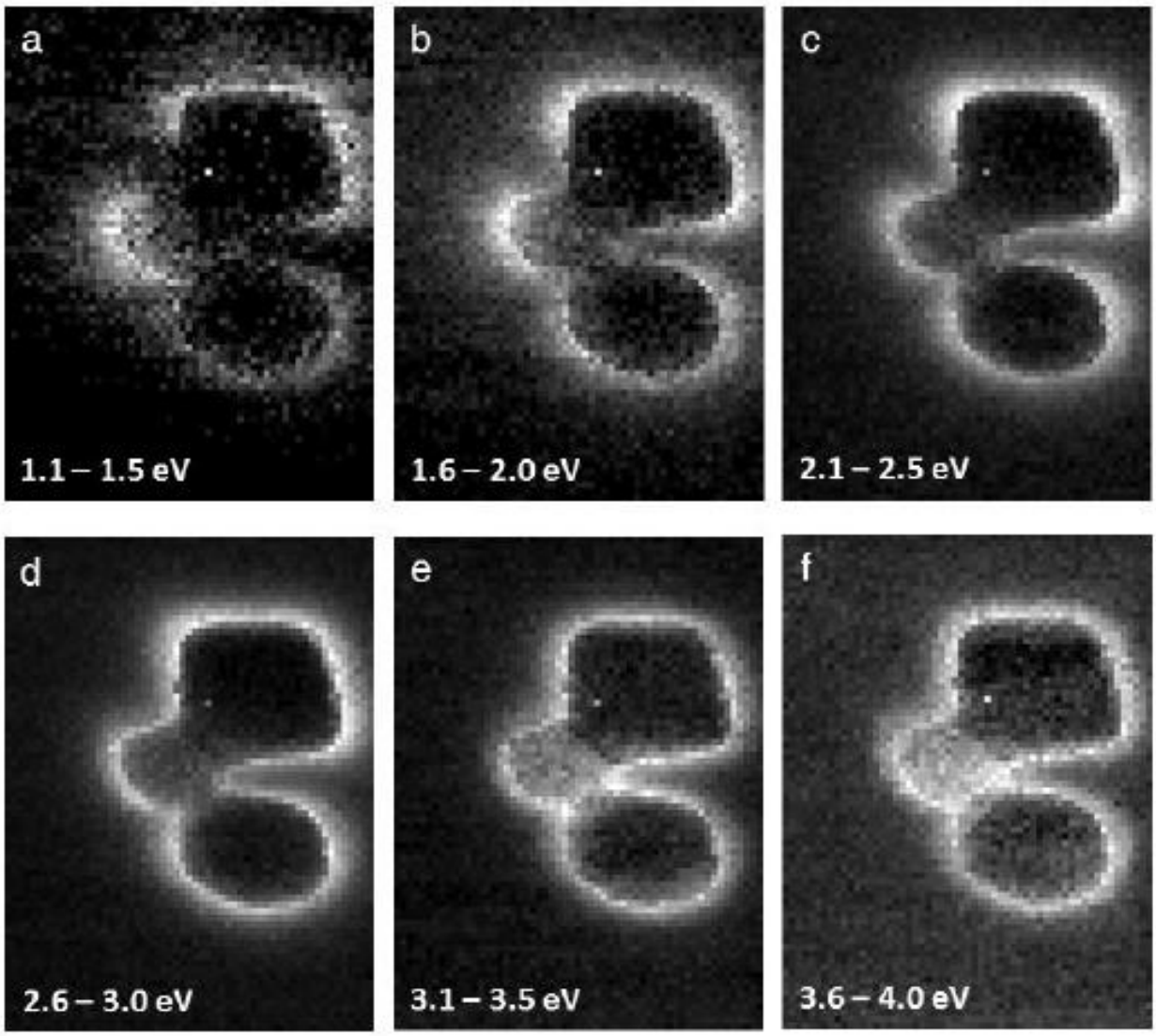

Figure 17. Energy slices from the spectrum image of trimer, *after* centering, normalizing to zero-loss peak (ZLP) and subtracting ZLP, but *before* noise reduction with principal components analysis.

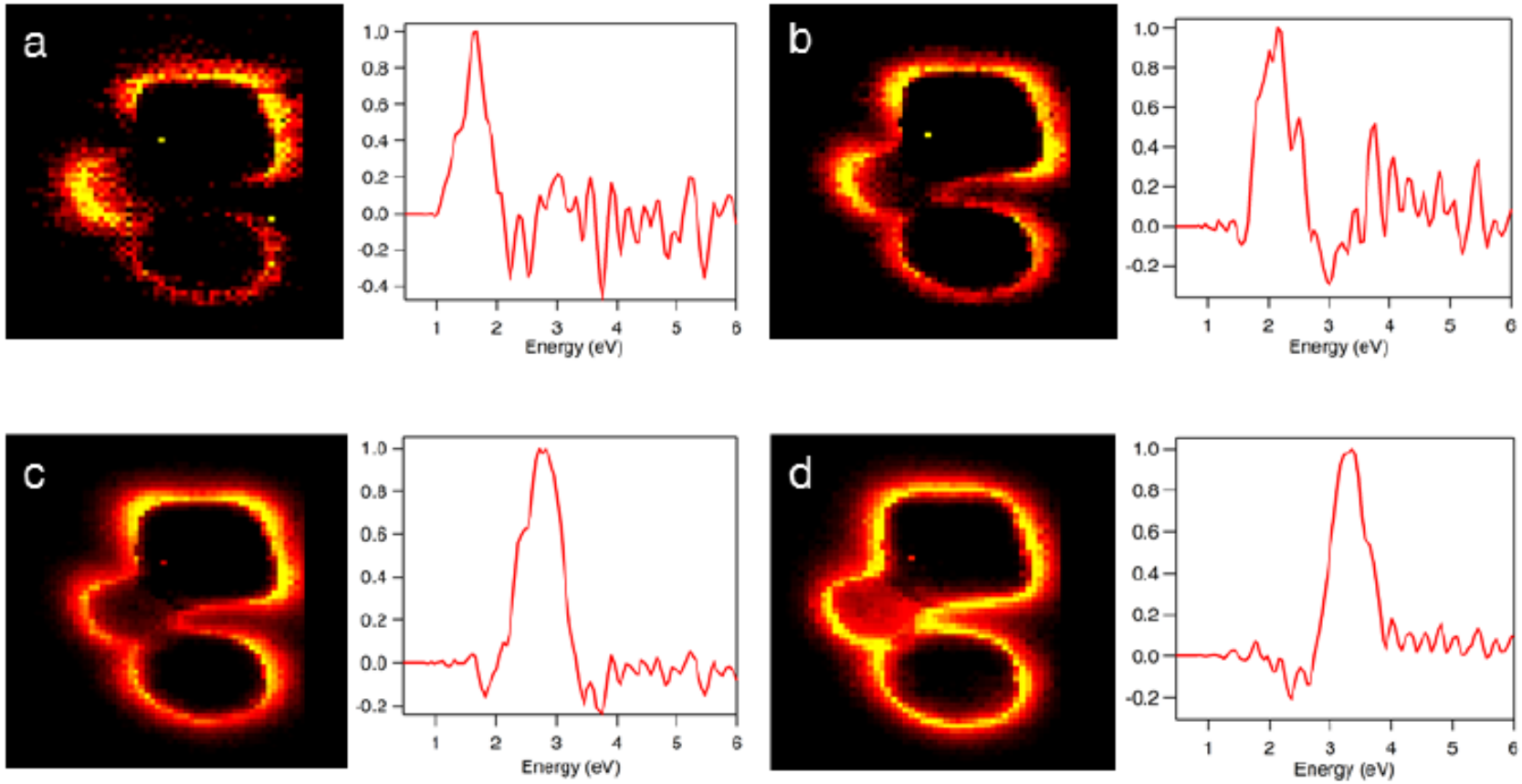

Figure 18. Energy slices from the spectrum image of trimer, *after* centering, normalizing to zero-loss peak (ZLP) and subtracting ZLP, but *before* noise reduction with principal components analysis.

References for Appendix

(1) Blackie, E.; Le Ru, E. C.; Meyer, M.; Timmer, M.; Burkett, B.; Northcote, P.; Etchegoin, P. G., Bi-Analyte Sers with Isotopically Edited Dyes. *Phys. Chem. Chem. Phys.* **2008,** *10* (28), 4147-4153.

(2) Dieringer, J. A.; Lettan, R. B.; Scheidt, K. A.; Van Duyne, R. P., A Frequency Domain Existence Proof of Single-Molecule Surface-Enhanced Raman Spectroscopy. *J. Am. Chem. Soc.* **2007,** *129* (51), 16249-16256.

(3) Wang, Y.; Eswaramoorthy, S. K.; Sherry, L. J.; Dieringer, J. A.; Camden, J. P.; Schatz, G. C.; Van Duyne, R. P.; Marks, L. D., A Method to Correlate Optical Properties and Structures of Metallic Nanoparticles. *Ultramicroscopy* **2009,** *109* (9), 1110-1113.

(4) Keenan, M. R., Exploiting Spatial-Domain Simplicity in Spectral Image Analysis. *Surface and Interface Analysis* **2009,** *41* (2), 79-87.

(5) Kotula, P. G.; Keenan, M. R.; Michael, J. R., Automated Analysis of Sem X-Ray Spectral Images: A Powerful New Microanalysis Tool. *Microscopy and Microanalysis* **2003,** *9* (01), 1-17.

(6) Guiton, B. S.; Iberi, V.; Li, S.; Leonard, D. N.; Parish, C. M.; Kotula, P. G.; Varela, M.; Schatz, G. C.; Pennycook, S. J.; Camden, J. P., Correlated Optical Measurements and Plasmon Mapping of Silver Nanorods. *Nano Lett.* **2011,** *11* (8), 3482-3488.

(7) Draine, B. T.; Flatau, P. J., Discrete-Dipole Approximation for Scattering Calculations. *J. Opt. Soc. Am. A:* **1994,** *11* (4), 1491-1499.

(8) Draine, B. T.; Flatau, P. J., Discrete-Dipole Approximation for Periodic Targets: Theory and Tests. *J. Opt. Soc. Am. A:* **2008,** *25* (11), 2693-2703.

(9) Lynch, D. W. H., W. R. , *Handbook of Optical Constants of Solids*. Academic Press: New York, 1985.

(10) Lazarides, A.; Lance Kelly, K.; Jensen, T.; Schatz, G., Optical Properties of Metal Nanoparticles and Nanoparticle Aggregates Important in Biosensors. *Journal of Molecular Structure: THEOCHEM* **2000,** *529* (1), 59-63.

CHAPTER III

OPTICAL AND ELECTRON ENERGY-LOSS SPECTROSCOPY OF THE NANOCUBE LSPR: PROBING FANO INTERFERENCES AND BEAM DAMAGE WITH STEM/EELS

A version of this chapter was originally written and submitted by Vighter Iberi, Nicholas W. Bigelow, Nasrin Mirsaleh-Kohan, Sarah Griffin, Philip D. Simmons, Jr., Beth S. Guiton, David J. Masiello, and Jon P. Camden:

Iberi, V., Bigelow, N. W., Mirsaleh-Kohan, N., Griffin, S., Simmons, P. D., Masiello, D. J., Guiton, B. S., and Camden, J. P. **Optical and Electron Energy-Loss Spectroscopy of the Nanocube LSPR: Probing Fano Interferences and Beam Damage with STEM/EELS.** *The Journal of Physical Chemistry C. Submitted.*

The article is represented in the submitted form, with the exception that the following J. Phys. Chem. C. required section has been removed: Acknowledgements. The dissertation author conducted all the experiments indicated in the paper, analyzed all the data, designed all the figures and wrote the bulk of the manuscript. The calculations and theoretical simulations indicated in the paper were conducted and written by NW Bigelow and DJ Masiello. All authors participated in the discussion of the results and approved the final manuscript.

Abstract

In this work, the Fano interference phenomenon between localized surface plasmon resonances (LSPRs) of individual silver nanocubes is investigated using dark-field optical microscopy and electron-energy loss spectroscopy (EELS) in a scanning transmission electron microscope (STEM). By computing the polarization induced by

the electron beam, we show that the hybridized modes responsible for this Fano interference are the same as those present in the resonance-Rayleigh scattering spectrum of an individual nanocube on a substrate. We further demonstrate the drastic changes that occur in the LSPR of nanocubes after exposure to the electron beam. Our work demonstrates the importance of using a correlated approach, combining both optical and electron spectroscopies, in probing the unique optical phenomena that are present in plasmonic systems.

Introduction

Metal nanoparticles support collective excitations of their conduction electrons, which are known as localized surface plasmon resonances (LSPRs).[1] LSPRs can be probed by both far- and near-field excitation sources, including laser light and swift electrons, from a scanning transmission electron microscope (STEM).[2-3] The field of plasmonics has experienced rapid growth in the last decade, driven in large part by the ability of metallic nanostructures to manipulate light at subwavelength scales and the high degree of tunability of the LSPRs by modifying the size, shape, and the surrounding dielectric environment of the nanoparticle.[4] When light is concentrated using LSPRs, there is an enhancement in the electric field near the nanoparticle surface, which can be used in various surface-enhanced spectroscopies, chemical catalysis, and other applications.[5-8] Localized surface plasmon resonances are also utilized routinely in other areas including the detection of single molecules,[9-12] optical waveguides,[13-16] photonic circuits,[17-19] non-linear spectroscopy,[20-25] and solar energy harvesting,[26-31] among others.

The recent increase in the diverse applications of LSPRs warrants a fundamental understanding of the optical response of nanostructures based on their geometries and interactions with a local environment, particularly at the single nanoparticle level.[32-33] Numerous studies on noble metal nanoparticles have correlated optical resonance-Rayleigh scattering with particle structure and continuum electrodynamics simulations.[34-42] These reports emphasized the strong dependence of the LSPRs on nanoparticle geometry; however, direct measurements of the near-field optical response of nanostructures were lacking. Similarly, the effect of a surrounding dielectric environment on LSPRs has been investigated with spectral shifts in the LSPRs due to changes in the refractive index of the substrate being reported.[36, 43-46] STEM with electron-energy loss spectroscopy (EELS) offers a method of probing the near-field response and local dielectric environment of metal nanoparticles with sub-nanometer spatial resolution.[2, 47-48] The emergence of STEM with EELS[2, 49-52] or energy-filtered TEM (EFTEM),[53-54] as an unprecedented tool for directly mapping plasmon modes in metal nanostructures with subnanometer resolution, has fostered a deeper understanding of the near- and far-field effects in plasmonic systems.

More recent studies have reported the manifestation of Fano resonances in plasmonic nanostructures when excited by light.[43, 55-57] This phenomenon occurs as a result of the coupling and interference between optically bright and dark modes due to symmetry breaking.[43, 58] The energetically narrow spectral features found in Fano resonances make them attractive in areas such as refractive index[59] and molecular sensing,[57] particularly due to the absence of radiative damping in the subradiant modes.

While most Fano interference studies have involved optical techniques such as dark-field optical microscopy, the observation of this phenomenon in STEM/EELS is still lacking and not well understood. To date, only cathodoluminescence (CL) spectroscopy, in which a focused electron beam is used as an excitation source, has been used to investigate Fano resonance signatures in certain plasmonic systems.[60-61] It has been shown that under electron beam excitation, Fano interferences were not observed in these systems. More recently, however, Masiello and co-workers have predicted the signatures of electron-driven Fano resonances in CL and EELS in symmetry-broken nanorod dimers that are heterogeneous in material composition and asymmetric in length.[62]

In this article, we apply a combination of dark-field optical microscopy and STEM/EELS[63-64] to the investigation of the LSPR properties in individual silver nanocubes. Single nanocubes have been chosen in this study due to their already well-characterized plasmonic and optical Fano resonances.[35-36, 43, 60, 65-67] Our observations are supported with fully three-dimensional continuum electrodynamics simulations using plane wave and electron beam excitations. Our simulations and experiments indicate that Fano interferences are present within the nanocube-substrate configuration and can be excited with EELS. Additionally, the damaging effect of raster-scanning the electron beam over the nanocube on the subsequent optical scattering spectrum is examined.

Experimental Methods

Dark-field Optical Scattering Experiment

Samples were prepared using a method described previously.[63] Briefly, a 3 μL aliquot of silver nanoparticle colloids was drop-coated onto a copper TEM grid coated with 10-20 nm of amorphous carbon (SPI supplies #3520C-CF). Resonance-Rayleigh scattering measurements were performed on a series of individual particles using an inverted microscope (Nikon, T*i*-U) equipped with a dark-field condenser (Nikon, NA=0.95-0.80). The excitation source was unpolarized light from a tungsten-halogen lamp. Scattered light from an individual nanoparticle was collected with a 100X objective (Nikon, 0.7<NA<1.4, oil immersion) and coupled into a dispersive imaging spectrometer (Acton Research, *f*=0.3 m) using a *f*=5.0 cm lens. Light was detected on a liquid nitrogen-cooled back-illuminated charge coupled detector (CCD) (Princeton Instruments, PIXIS 100). The dark-field scattering spectrum of each individual nanocube was obtained using a 150 g/mm grating with a 500 nm blaze. A wide-field image of the silver nanoparticles on the TEM grid was also recorded to serve as a map for subsequent location in the STEM. This method enabled correlated optical and STEM measurements from the same nanostructures.[68]

STEM/EELS Experiment

STEM/EELS experiments were performed on a Carl Zeiss LIBRA® 200MC field emission transmission electron microscope equipped with a monochromator and operating at 200 kV. The electron source was a Schottky emitter and the

monochromator was integrated in the field emission gun to form an omega-type imaging element. This special design of the monochromator eliminated 2nd order chromatic aberrations and also made it suitable for STEM/EELS under the operating conditions. The nanocubes of interest were found by comparing the optical maps to the pattern of particles imaged in the STEM at very low resolution. After correctly identifying each nanocube with an optically measured LSPR spectrum, a high resolution high angle annular dark field (HAADF) image was recorded. EEL spectra were obtained at each pixel over the entire region of interest with a dispersion of 0.05 eV per channel and a dwell time of 0.05 s per pixel. The pixel size density used for collecting each spectrum image (SI) resulted in a total acquisition time of 12 minutes per SI. The energy resolution for each SI, determined by the full width at half maximum (FWHM) of the zero loss peak (ZLP), was 0.19 eV.

Experimental STEM/EELS data from each nanocube were analyzed using DigitalMicrograph imaging software by Gatan Inc. Briefly, a pixel of interest from the SI of the nanocube was selected and the corresponding full energy-loss spectrum was obtained. The ZLP of the EEL spectrum was fit to a Gaussian and Lorentzian and centered at 0 eV, with each EEL spectrum normalized to the ZLP before subtraction. The deconvoluted EEL spectrum was truncated to a region (2.0-4.0 eV) corresponding to the measured Rayleigh scattering spectra of the nanocubes in order to fully compare the resonances from both excitation sources. The Automated eXpert Spectral Image Analysis (AXSIA) program developed by Keenan and co-workers[69] was used in order to extract and interpret the plasmon modes which overlap spectrally and spatially.

Furthermore, the application of multivariate statistical analysis (MVSA) to the experimental EELS data ensured the reduction of non-uniform noise in the spectrum image while the principal component analysis (PCA) in Automated eXpert Spectral Image Analysis (AXSIA) produced the plasmon modes and corresponding spectra. [63]

Theoretical Methods

The coupled-dipole approximation[70] or discrete dipole approximation (DDA)[71] approach is routinely used to study the response of metal nanoparticles subjected to electromagnetic radiation.[4] In this work, plane wave spectra and the associated scattered electric fields and target polarizations were generated with the DDA.[71] Electron energy-loss spectra (EELS), the resulting scattered electric fields, and target polarizations were generated using the recently developed electron-driven discrete dipole approximation (*e*-DDA).[72-73] The structure of the computed cubes was adjusted within the experimental measurement error to best fit the computed far-field scattering spectrum to the experimental results. The corner radii were within the variation of the observed radii for the cube being modeled, and the height of the cube, while not observed directly, was within the observed deviation from cubic of other synthesized cubes in the same batch.

The two lowest energy plasmonic modes of the cube on a substrate are hybrid modes constructed from linear combinations of dipole ($\mathbf{D}^0$) and quadrupole ($\mathbf{Q}^0$) modes of the cube in vacuum.[43] In order to determine the phase and relative magnitude of $\mathbf{D}^0$ and $\mathbf{Q}^0$ across a spectral range spanning the two lowest energy modes, the target

polarizations, $\mathbf{P}\ \omega$, were computed, then projected onto primitive dipolar and quadrupolar normal vectors,

$$\mathrm{d}\ \omega \ = \ \mathbf{n}_{\mathrm{d}}\ \mathbf{P}\ \omega$$

$$\mathrm{q}\ \omega \ = \ \mathbf{n}_{\mathrm{q}}\ \mathbf{P}\ \omega$$

where d is the dipolar amplitude, $\mathbf{n}_d$ is the primitive dipolar normal vector, *q* is the quadrupolar amplitude, and $\mathbf{n}_q$ is the primitive quadrupolar normal vector. For the plane wave, the primitive dipolar normal vector points in the opposite direction of the polarization of the driving electric field. The plane wave driven primitive quadrupolar normal vector points parallel to the polarization of the driving electric field in the upper half of the cube, and antiparallel in the bottom half. For EELS, the primitive dipolar normal vector points radially outward from the line path of the electron. The EELS primitive quadrupolar normal vector points radially outward from the line path of the electron in the upper half of the cube, and radially inward in the lower half. The polarization of the substrate was not explicitly treated by this mode projection analysis, but its effects are implicitly accounted for in all calculations.

Results

A. Correlated studies of individual silver nanocubes

The plasmonic properties of silver nanocubes were characterized using dark-field optical microscopy and STEM/EELS (see Experimental Methods section) although the discussion here will be limited to a single nanocube. Structural parameters for each

cube such as edge lengths and radius of curvature have been obtained from the HAADF images in a STEM. Figure 19 shows the overlaid experimental (red trace) and theoretical (black trace) spectra obtained using plane wave and electron beam excitations, from the *exact same* nanocube whose corresponding HAADF image is shown in the inset. The experimental and theoretical optical scattering spectra (left panel) highlight the characteristic optical response of a silver nanocube on a substrate under plane wave excitation and are in excellent agreement with each other and with previous studies.[35-36, 65] In the optical scattering spectra, the peak at ~2.3 eV is attributed to the hybridized bonding mode, $\mathbf{D}^0 + \mathbf{Q}^0$, between the primitive dipolar ($\mathbf{D}^0$) and quadrupolar ($\mathbf{Q}^0$) modes of the cube in vacuum while the peak at ~2.8 eV corresponds to the hybridized antibonding mode, $\mathbf{D}^0 - \mathbf{Q}^0$. Hybridization between the $\mathbf{D}^0$ and $\mathbf{Q}^0$ modes occurs in the presence of a substrate, as evidenced by the dip at ~2.6 eV in the optical scattering spectra, which *lowers* the symmetry of the plasmonic system and can be interpreted as a substrate-induced Fano resonance.[43] Moreover, the splitting and relative peak intensities in the optical scattering spectrum are known to be strong functions of the spacing between the cube and the substrate.[65] The higher energy modes (3.2 eV and 3.5 eV) present in the theoretical scattering spectrum are beyond the energy range of our spectrometer and hence, are not observed experimentally.

In Figure 19, the experimental EEL spectra (red trace, middle and right panel) are extracted from two different positions (1 and 2 in HAADF image inset) on the nanocube although the STEM/EELS procedure involved raster-scanning the electron

beam over the entire nanocube. This was done in order to investigate the spectral dependence of the plasmon resonance on the position of the electron beam. The EEL probability spectra computed at the two beam positions are indicated by the dotted black trace. In order to best compare to the STEM/EELS experiment, each point in the computed EEL spectra was convoluted with a Gaussian function with a full width at half-maximum (FWHM) of 0.19 eV corresponding to the energy resolution of the ZLP in the STEM/EELS experiment (solid black trace). While the computed and experimental EEL spectra at the corner and edge of the cube are in good agreement, the absence of the large dip in the experimental EEL spectrum at position 1 at ~3.1 eV may be due to an overlap between plasmon modes which is evident by the shoulder at ~3.2 eV in the experimental EEL spectrum.

Utilizing a correlated approach in the study of the LSPR properties of silver nanocubes facilitates the investigation of Fano interferences with STEM/EELS since the optical scattering spectrum provides the essential information on where this interference is likely to occur. In the resonance-Rayleigh scattering spectrum, the dip at 2.6 eV indicated by a black arrow, is due to a Fano interference corresponding to the local minimum at ~2.5 eV in the experimental EEL spectrum at positions 1 and 2. Even without any sophisticated post STEM/EELS experimental data processing, the ability to resolve such a feature highlights the significance of obtaining EEL spectra at high energy resolution.[74-75] In the computed EEL spectra, a similar feature at 2.6 eV (indicated by black arrow) is present at both electron probe positions; however, this feature is more pronounced when the probe is at position 2.

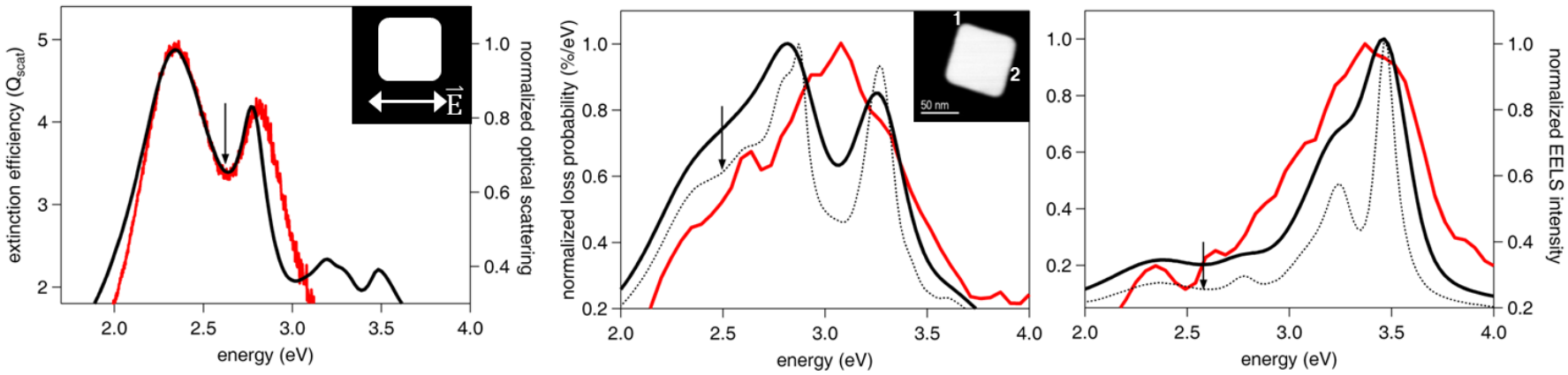

Figure 19. Comparison of the experimental (red trace) and computed (black trace) spectra obtained using plane wave light and electron beam excitation, for a single silver nanocube (HAADF image in inset). Left panel: resonance-Rayleigh scattering spectrum of a silver nanocube (schematic diagram indicating the polarization of the incident electric field in inset). Middle and right panels: electron-energy loss (EEL) spectrum obtained from the corner, (position 1) and edge (position 2) of the same nanocube. Solid black trace in the EEL spectra was obtained by convolving each point in the computed EEL spectra (dotted black trace) with a Gaussian function with a full width at half-maximum of 0.19 eV. Black arrows in the three panels indicate the position at which the $\mathbf{D^0 + Q^0 \rightarrow D^0 - Q^0}$ Fano interference occurs in the simulations.

This suggests that the efficiency of the coupling between the $\mathbf{D}^0$ and $\mathbf{Q}^0$ modes depends on the position of the probe and will be discussed subsequently. A slight energy difference (~0.1 eV) between the computed resonance-Rayleigh Fano dip and the experimental EELS Fano dip observed in position 2 is likely an artifact of either electron beam damage or ZLP removal, and we do not believe it to be of any significance.

B. Investigation of Fano interference in STEM/EELS

Coupling between a bright and dark mode is essential for the observation of Fano resonances. With a STEM electron beam, the selection rules governing the excitation of LSPRs enable the excitation of both bright and dark modes and might hinder the direct observation of this interference. However, the strong spatial dependence of the evanescent electric field of the passing electron suggests the possibility of an interference between a mode excited close to the electron beam and another mode excited outside its influence.[62] While the substrate-mediated interaction between the $\mathbf{D}^0$ and $\mathbf{Q}^0$ modes under plane wave excitation has been shown to be a Fano resonance,[43] no experimental work has of yet shown whether such a resonance will exist under electron-beam excitation.

We can understand the Fano effect in the cube on a substrate by attaching a phase, $\varphi(\omega)$, to the $\mathbf{Q}^0$ mode relative to the $\mathbf{D}^0$ mode as a function of excitation energy so that we may write the contribution from the two fundamental modes as a function of energy as:

$$\mathbf{P} = \mathbf{D^0} + \mathbf{Q^0} e^{i\varphi(\omega)}$$

where **P** is the overall target polarization and $\mathbf{D}^0$ and $\mathbf{Q}^0$ are the full vector-valued representations of the modes they represent. The Fano resonance occurs when φ crosses π/2, where the hybridization switches from a bonding to an antibonding arrangement.

To extract relative phase data from the computed polarizations, we have projected primitive dipole and quadrupole model normal vectors onto the simulated data (see Methods for greater detail). Figure 20 shows the projection coefficients d(ω) and q(ω), for the $\mathbf{D}^0$ and $\mathbf{Q}^0$ modes respectively, as a function of excitation energy for both plane wave and electron beam excitations. The blue and green traces in all three cases correspond to d(ω) and q(ω), respectively. The red trace corresponds to the computed optical scattering and EEL spectra and has been included for comparison. Under plane wave excitation (left panel), a relative phase shift through φ = π/2 in q(ω) occurs around 2.7 eV. A corresponding phase shift through φ = π/2 is seen in the two rightmost panels of Figure 20, indicating the presence of a Fano interference in the EEL spectra as well. Similarly, a corresponding relative phase shift occurs in STEM/EELS close to 2.7 eV, again suggesting a Fano resonance. These results are in excellent agreement with the computed substrate- and vacuum-localized scattered electric fields computed just lower and higher in loss energy from the phase-flip (Figure 22). However, the phase shift is less pronounced in both edge and corner EEL spectra, indicating that the Fano interference, while present, will be much more subtle in the EEL spectrum than in the plane wave spectrum. We believe this to be due to the electron beam's capability to excite both the quadrupole and the dipole, though at different oscillator strengths

depending on the location of the electron beam. By driving both the $\mathbf{D}^0$ and $\mathbf{Q}^0$ modes with the incident electric field to an extent, the phase shift in EELS is reduced compared to plane wave excitation and the Fano effect becomes smaller. It is also worth noting that a Fano effect is enhanced in cubes without rounded corners.[43]

C. Plasmon and EEL probability maps of silver nanocubes

Figure 21 presents the experimental and computed EEL probability maps of the same nanocube. The experimental spectrum images (left panel) and normalized loading spectra (middle panel) were extracted using the MVSA and AXSIA program[69]. This method has been used previously in the extraction and interpretation of plasmon modes with high spectral and spatial overlap.[63-64] The extracted eigenmodes at 2.2 eV, 2.7 eV and 3.1 eV exhibit a similar spatial profile in which the intensity is localized at the corners of the cube while the eigenmode at 3.5 eV has an edge-localized spatial profile. The EEL probability maps (right panel) were computed for energies corresponding to the peaks in the theoretical EEL spectra (Figure 19, middle and right panels) for comparison. Knowledge of the spectral positions of the superradiant (~2.3 eV) and subradiant (~2.8 eV) hybridized plasmon modes obtained from the optical scattering spectrum in Figure 19 enabled us to directly correlate the energies that correspond to the same plasmon eigenmodes in Figure 21 (2.2 eV and 2.7 eV). However, discerning the three-dimensional profile of the hybridized plasmon modes, which have identical spatial profiles when projected onto the plane perpendicular to the motion of the electron beam, was done only by computational means since our STEM/EELS experiment only gathers two-dimensional loss probability information (Figure 22). A

recent report by Nicoletti et al. has demonstrated the ability to obtain three-dimensional plasmon maps in silver nanocubes with electron tomography[76]

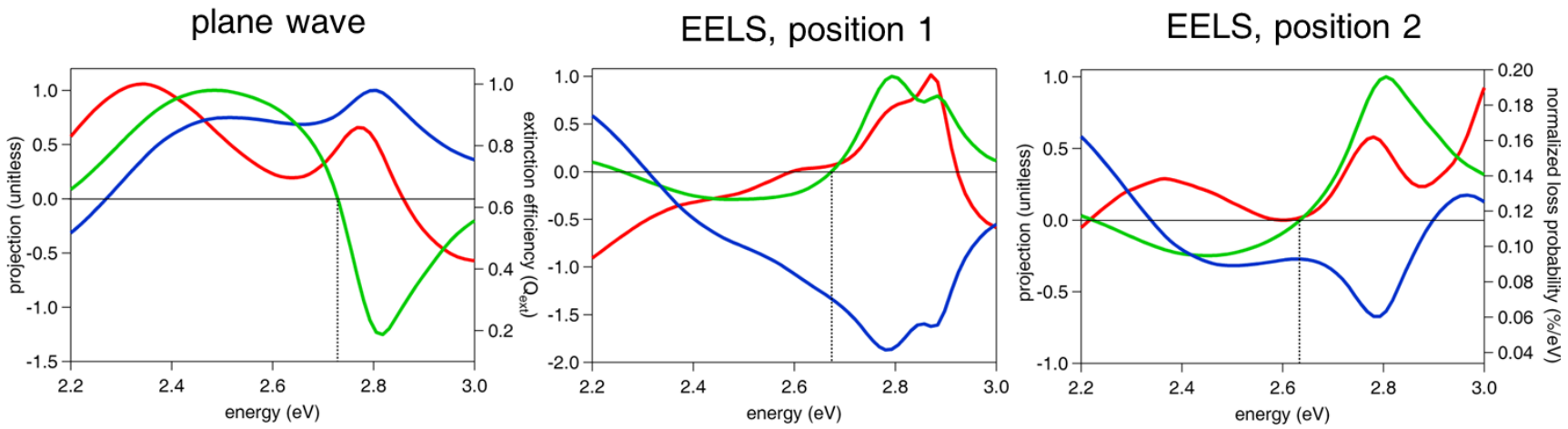

Figure 20. Investigation of Fano interferences using the projection coefficients d( ) (blue trace) and q( ) (green trace) of the $\mathbf{D^0}$ and $\mathbf{Q^0}$ modes under plane wave and electron-beam excitation. Left panel: projection coefficients as a function of excitation energy under plane wave excitation. The Fano interference occurs where the phase of the $\mathbf{Q^0}$ mode crosses $\varphi = \pi/2$ and is indicated by a dotted vertical line at ~2.7 eV. The computed optical scattering spectrum (red trace) has been used to correlate the position where the Fano interference occurs (~2.6 eV). Middle and right panels: projection coefficients with computed EEL spectra obtained at the corner and edge of the nanocube, respectively. Under electron beam excitation, the phase of the $\mathbf{Q^0}$ mode also cross $\varphi = \pi/2$ near 2.7 eV and suggests that the Fano interference mechanism under STEM/EELS excitation is the same as for a plane wave.

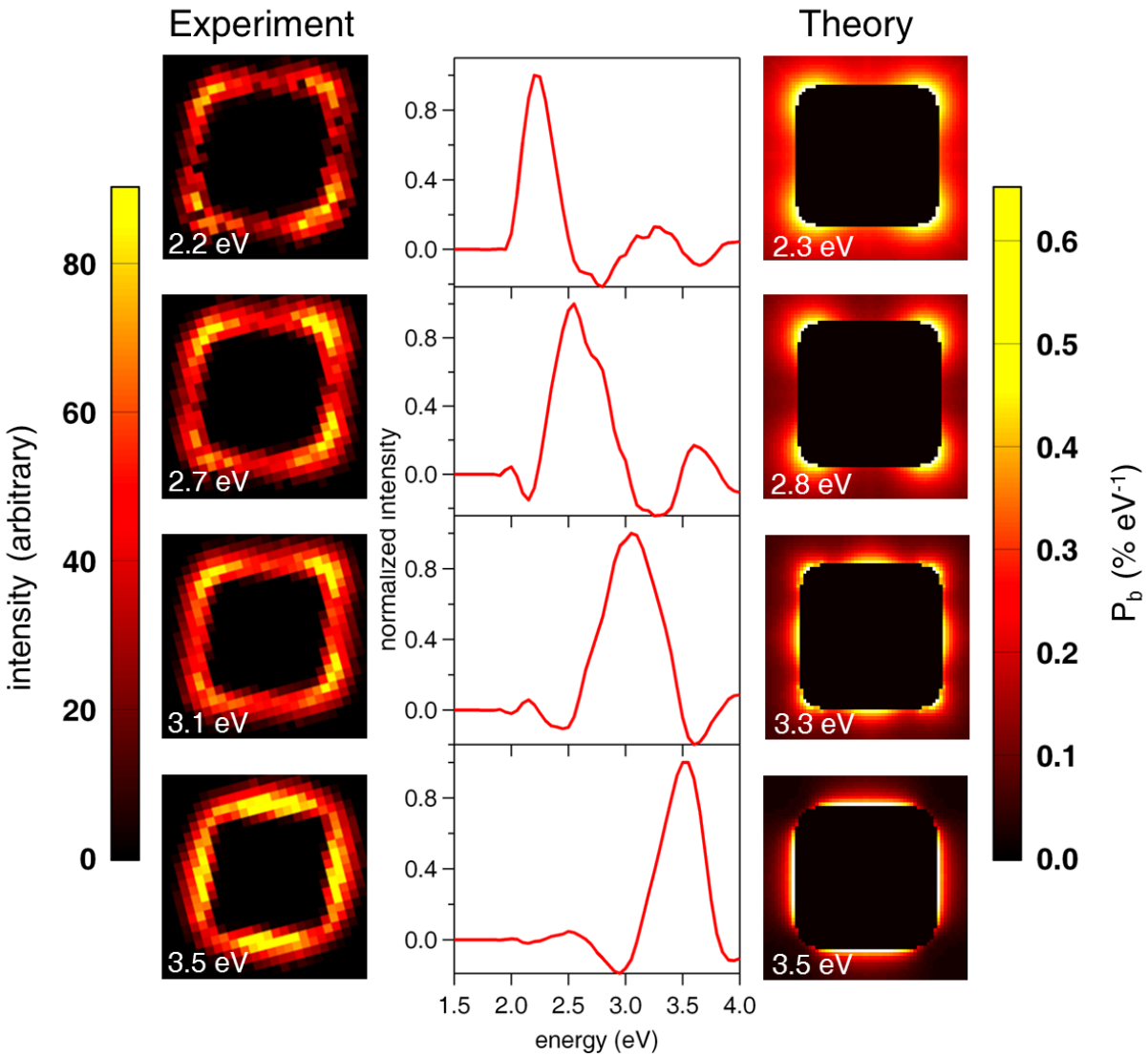

Figure 21. Top-down plasmon maps and computed EEL probability maps of a silver nanocube. Left panel: experimental EEL spectrum image components derived using MVSA and AXSIA. Middle panel: corresponding loading spectra for each spectrum image component, interpreted as the energy of each plasmon mode. Right panel: computed EEL probability maps indicating spatial regions on the nanocube where there is high electron energy loss probability.

D. Identification of Vacuum- and Substrate-Localized Hybridized modes

Figure 22 shows the computed scattered electric fields of the two lowest-energy modes, in which the vacuum- and substrate-localization of the electric fields are investigated for both plane wave and EELS for two different electron-beam positions. Under plane wave excitation, the substrate-localized electric near-field (Figure 22, left panel, top) arises from the hybridized plasmon mode formed from the constructive superposition of the primitive dipolar ($\mathbf{D}^0$) and quadrupolar ($\mathbf{Q}^0$) plasmon modes, $\mathbf{D}^0 + \mathbf{Q}^0$. On the other hand, the vacuum-localized electric near-field (Figure 22, right panel, top) corresponds to the hybridized mode that originates from the destructive superposition of the primitive modes, $\mathbf{D}^0 - \mathbf{Q}^0$.[43]

In the electron-beam excitation scenario (Figure 22, middle and bottom rows), the field maps show two spatial profiles that correspond to the $\mathbf{D}^0 + \mathbf{Q}^0$ and $\mathbf{D}^0 - \mathbf{Q}^0$ hybridized modes at 2.34 eV and 2.8 eV obtained under plane wave excitation. For the $\mathbf{D}^0 + \mathbf{Q}^0$ mode, the spatial profiles of the scattered near-electric-fields show a highly localized intensity at the cube-substrate interface for the two electron-beam positions. While the intensity is localized at the interface, there are small differences in spatial profile of this hybridized mode as the electron beam is moved from the corner to the edge of the cube. This is due to the induced polarizations in the target from the electron beam giving rise to the scattered fields that depend on the position of the electron probe relative to the target. Similarly, the $\mathbf{D}^0 - \mathbf{Q}^0$ hybridized mode shows a highly localized intensity at the top of the cube for both excitation sources. The significant correspondence between these plane wave and EELS hybridized plasmon modes

suggests that a Fano interference that has the exact same mechanism as that of a plane wave is induced by the electron beam.

E. Changes in local dielectric environment

A recent EELS study of silver nanocubes by Mazzucco et al. suggested highly local effects on the LSPR[77]; however, a comparison of the experimental optical scattering spectra for the nanocubes was lacking despite the known strong dependence of the optical spectra on the local dielectric environment. The deposition of contamination by the electron during STEM/EELS imaging warrants a study on how modifications to the local environment affect the optical scattering spectrum. Figure 23 (left and right panels) illustrates the optical scattering spectrum of a single silver nanocubes (ADF in inset), taken before (black trace) and after (red trace) STEM/EELS measurements. The change in the optical LSPRs after STEM/EELS suggests that substrate has been drastically altered by the electron beam. Furthermore, the *stretching* of the LSPRs differs from previous studies on silver nanocubes which reported red shifts both peaks in the LSPRs as the refractive index of the substrate was increased.[36, 43] This effect has been recently highlighted in a perspective article[78] and it also suggests a possible reason for the weak observation of Fano interferences in STEM/EELS.

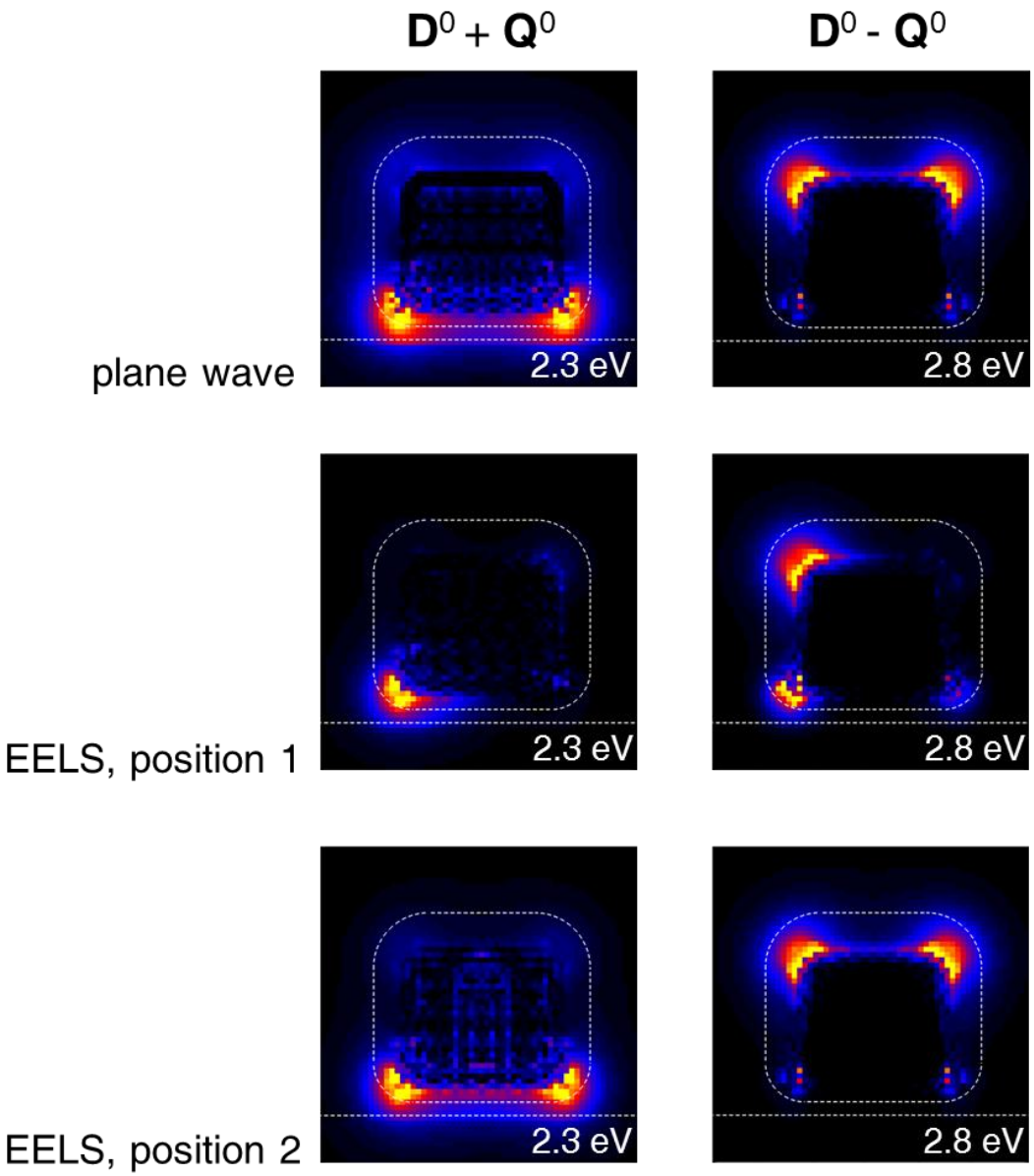

Figure 22. Scattered near-electric fields of hybridized plasmon modes in a silver nanocube on a substrate (dashed line). Left panel: substrate-localized plasmon mode for plane wave (top) and electron-beam excitations (middle and bottom), corresponding to the constructive interference of the hybridized primitive dipolar ($\mathbf{D^0}$) and quadrupolar ($\mathbf{Q^0}$) plasmon modes. Right panel: vacuum-localized plasmon modes corresponding to the destructive interference of the $\mathbf{D^0}$ and $\mathbf{Q^0}$ plasmon modes. The plane in which the electric field is evaluated lies outside the cube by 1 nm, parallel to the front face of the cube, perpendicular to the substrate.

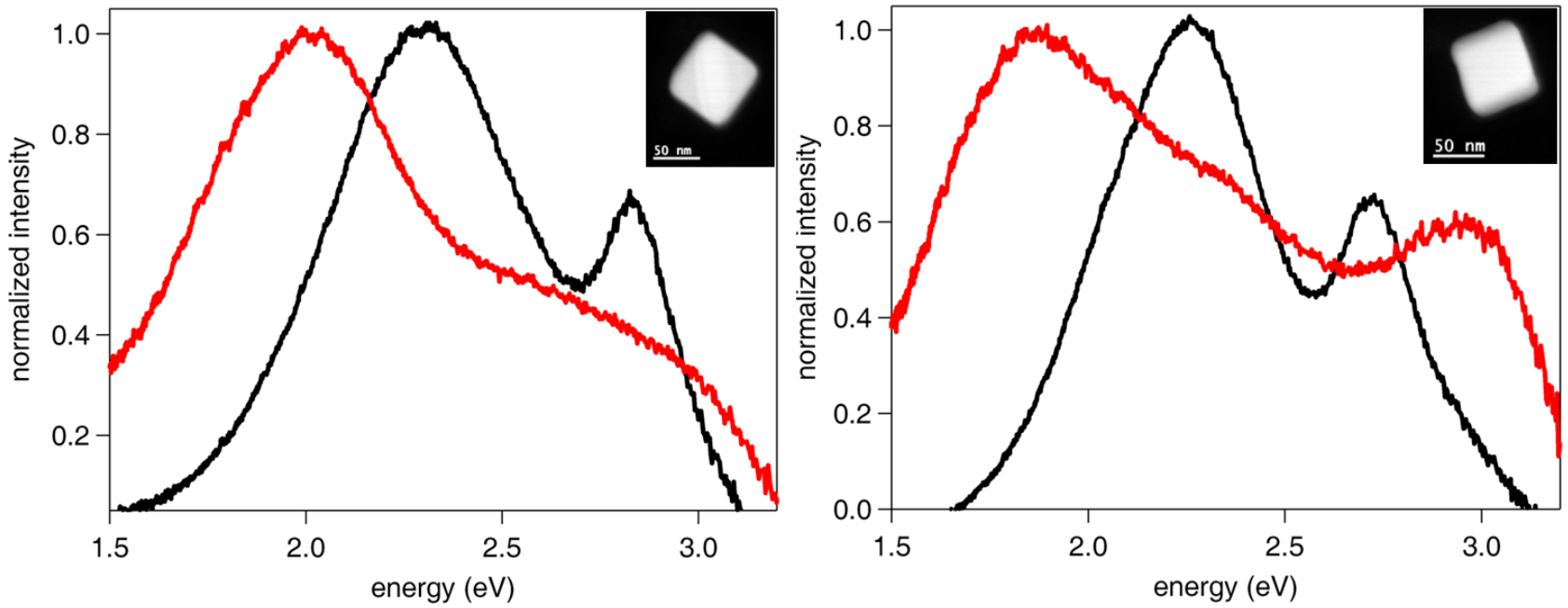

Figure 23. Resonance-Rayleigh scattering spectra of silver nanocubes obtained before (black trace), and after (red trace) exposure to the electron beam in STEM/EELS. The optical scattering spectra of both nanocubes after STEM/EELS strongly suggest a modification of the local dielectric environment by the electron beam.

Conclusion

Through a correlated approach we have predicted and observed for the first time the subtle Fano interference in silver nanocubes with STEM/EELS. The presence of a substrate mediates the hybridization of the primitive dipolar and quadrupolar modes present in the silver nanocube in both optical and STEM/EELS experiments. By computing the polarization phase-flip from a relative phase of 0 to π/2 induced by the electric field of the electron probe, we have shown that the hybridized modes responsible for this interference are the same as those present in optical spectroscopy. Furthermore, we have demonstrated the drastic changes that occur in the optical LSPRs of silver nanocubes after exposure to the electron beam. As efforts to understand the detailed connection between optically-driven and EELS-derived plasmons in complex nanostructures continue, a correlated approach, along with sophisticated data analysis and simulations, will be essential.

References for Chapter III

(1) Maier, S. A., *Plasmonics: Fundamentals and Applications*. 1st ed.; Springer-Verlag: New York, 2007.

(2) Garcia de Abajo, F. J., Optical Excitations in Electron Microscopy. *Rev. Mod. Phys.* **2010,** *82* (1), 209-275.

(3) Ritchie, R. H., Plasmon Losses by Fast Electrons in Thin Films. *Phys. Rev.* **1957,** *106* (5), 874-881.

(4) Kelly, K. L.; Coronado, E.; Zhao, L. L.; Schatz, G. C., The Optical Properties of Metal Nanoparticles: The Influence of Size, Shape, and Dielectric Environment. *J. Phys. Chem. B* **2003,** *107* (3), 668-677.

(5) Albrecht, M. G.; Creighton, J. A., Anomalously Intense Raman-Spectra of Pyridine at a Silver Electrode. *J. Am. Chem. Soc.* **1977,** *99* (15), 5215-5217.

(6) Jeanmaire, D. L.; Van Duyne, R. P., Surface Raman Spectroelectrochemistry .1. Heterocyclic, Aromatic, and Aliphatic-Amines Adsorbed on Anodized Silver Electrode. *J. Electroanal. Chem.* **1977,** *84* (1), 1-20.

(7) Schatz, G. C.; Van Duyne, R. P., Electromagnetic Mechanism of Surface-Enhanced Spectroscopy. In *Handbook of Vibrational Spectroscopy*, Chalmers, J. M.; Griffiths, P. R., Eds. John Wiley & Sons Ltd: 2002.

(8) Ingram, D. B.; Linic, S., Water Splitting on Composite Plasmonic-Metal/Semiconductor Photoelectrodes: Evidence for Selective Plasmon-Induced Formation of Charge Carriers near the Semiconductor Surface. *J. Am. Chem. Soc.* **2011,** *133* (14), 5202-5205.

(9) Kneipp, K.; Wang, Y.; Kneipp, H.; Perelman, L. T.; Itzkan, I.; Dasari, R.; Feld, M. S., Single Molecule Detection Using Surface-Enhanced Raman Scattering (Sers). *Phys. Rev. Lett.* **1997,** *78* (9), 1667-1670.

(10) Nie, S. M.; Emery, S. R., Probing Single Molecules and Single Nanoparticles by Surface-Enhanced Raman Scattering. *Science* **1997,** *275* (5303), 1102-1106.

(11) Michaels, A. M.; Jiang, J.; Brus, L., Ag Nanocrystal Junctions as the Site for Surface-Enhanced Raman Scattering of Single Rhodamine 6g Molecules. *J. Phys. Chem. B* **2000,** *104* (50), 11965-11971.

(12) Camden, J. P.; Dieringer, J. A.; Wang, Y. M.; Masiello, D. J.; Marks, L. D.; Schatz, G. C.; Van Duyne, R. P., Probing the Structure of Single-Molecule Surface-Enhanced Raman Scattering Hot Spots. *J. Am. Chem. Soc.* **2008,** *130* (38), 12616-12617.

(13) Quinten, M.; Leitner, A.; Krenn, J.; Aussenegg, F., Electromagnetic Energy Transport Via Linear Chains of Silver Nanoparticles. *Opt. Lett.* **1998,** *23* (17), 1331-1333.

(14) Maier, S. A.; Kik, P. G.; Atwater, H. A.; Meltzer, S.; Harel, E.; Koel, B. E.; Requicha, A. A. G., Local Detection of Electromagnetic Energy Transport Below the Diffraction Limit in Metal Nanoparticle Plasmon Waveguides. *Nat. Mater.* **2003,** *2* (4), 229-232.

(15) Stockman, M. I., Nanofocusing of Optical Energy in Tapered Plasmonic Waveguides. *Phys. Rev. Lett.* **2004,** *93*, 137404-137404.

(16) Oulton, R. F.; Sorger, V. J.; Genov, D.; Pile, D.; Zhang, X., A Hybrid Plasmonic Waveguide for Subwavelength Confinement and Long-Range Propagation. *Nature Photonics* **2008,** *2* (8), 496-500.

(17) Maier, S. A., Plasmonics: Metal Nanostructures for Subwavelength Photonic Devices. *Ieee Journal of Selected Topics in Quantum Electronics* **2006,** *12* (6), 1214-1220.

(18) Ozbay, E., Plasmonics: Merging Photonics and Electronics at Nanoscale Dimensions. *Science* **2006,** *311* (5758), 189-193.

(19) Ebbesen, T. W.; Genet, C.; Bozhevolnyi, S. I., Surface-Plasmon Circuitry. *Physics Today* **2008,** *61* (5), 44.

(20) Golab, J. T.; Sprague, J. R.; Carron, K. T.; Schatz, G. C.; Van Duyne, R. P., A Surface Enhanced Hyper-Raman Scattering Study of Pyridine Adsorbed onto Silver - Experiment and Theory. *J. Chem. Phys.* **1988,** *88* (12), 7942-7951.

(21) Kneipp, K.; Kneipp, H.; Itzkan, I.; Dasari, R. R.; Feld, M. S., Surface-Enhanced Non-Linear Raman Scattering at the Single-Molecule Level. *Chemical Physics* **1999,** *247* (1), 155-162.

(22) Kneipp, J.; Kneipp, H.; Kneipp, K., Two-Photon Vibrational Spectroscopy for Biosciences Based on Surface-Enhanced Hyper-Raman Scattering. *Proc. Natl. Acad. Sci. U. S. A.* **2006,** *103* (46), 17149-17153.

(23) Maier, S. A., Plasmonic Field Enhancement and Sers in the Effective Mode Volume Picture. *Opt. Express* **2006,** *14* (5), 1957-1964.

(24) Milojevich, C. B.; Silverstein, D. W.; Jensen, L.; Camden, J. P., Probing Two-Photon Properties of Molecules: Large Non-Condon Effects Dominate the Resonance Hyper-Raman Scattering of Rhodamine 6g. *J. Am. Chem. Soc.* **2011,** *133* (37), 14590-14592.

(25) Milojevich, C. B.; Silverstein, D. W.; Jensen, L.; Camden, J. P., Probing One-Photon Inaccessible Electronic States with High Sensitivity: Wavelength Scanned Surface Enhanced Hyper-Raman Scattering. *ChemPhysChem* **2011,** *12* (1), 101-103.

(26) Pillai, S.; Catchpole, K.; Trupke, T.; Green, M., Surface Plasmon Enhanced Silicon Solar Cells. *Journal of applied physics* **2007,** *101*, 093105.

(27) Catchpole, K. R.; Polman, A., Design Principles for Particle Plasmon Enhanced Solar Cells. *Appl. Phys. Lett.* **2008,** *93* (19), 191113.

(28) Morfa, A. J.; Rowlen, K. L.; Reilly, T. H.; Romero, M. J.; van de Lagemaat, J., Plasmon-Enhanced Solar Energy Conversion in Organic Bulk Heterojunction Photovoltaics. *Appl. Phys. Lett.* **2008,** *92* (1).

(29) Kim, S.-S.; Na, S.-I.; Jo, J.; Kim, D.-Y.; Nah, Y.-C., Plasmon Enhanced Performance of Organic Solar Cells Using Electrodeposited Ag Nanoparticles. *Appl. Phys. Lett.* **2008,** *93*, 073307.

(30) Haran, G., Single-Molecule Raman Spectroscopy: A Probe of Surface Dynamics and Plasmonic Fields. *Accounts of Chemical Research* **2010,** *43* (8), 1135-1143.

(31) Atwater, H. A.; Polman, A., Plasmonics for Improved Photovoltaic Devices. *Nat. Mater.* **2010,** *9* (3), 205-213.

(32) Ringe, E.; Sharma, B.; Henry, A.-I.; Marks, L. D.; Van Duyne, R. P., Single Nanoparticle Plasmonics. *Phys. Chem. Chem. Phys.* **2013,** *15* (12), 4110-4129.

(33) Sannomiya, T.; Vörös, J., Single Plasmonic Nanoparticles for Biosensing. *Trends in biotechnology* **2011,** *29* (7), 343-351.

(34) McMahon, J. M.; Gray, S. K.; Schatz, G. C., Nonlocal Optical Response of Metal Nanostructures with Arbitrary Shape. *Phys. Rev. Lett.* **2009,** *103* (9).

(35) Ringe, E.; McMahon, J. M.; Sohn, K.; Cobley, C.; Xia, Y.; Huang, J.; Schatz, G. C.; Marks, L. D.; Van Duyne, R. P., Unraveling the Effects of Size, Composition, and Substrate on the Localized Surface Plasmon Resonance Frequencies of Gold and Silver Nanocubes: A Systematic Single-Particle Approach. *J. Phys. Chem. C* **2010,** *114* (29), 12511-12516.

(36) Sherry, L. J.; Chang, S. H.; Schatz, G. C.; Van Duyne, R. P.; Wiley, B. J.; Xia, Y. N., Localized Surface Plasmon Resonance Spectroscopy of Single Silver Nanocubes. *Nano Lett.* **2005,** *5* (10), 2034-2038.

(37) Schubert, O.; Becker, J.; Carbone, L.; Khalavka, Y.; Provalska, T.; Zins, I.; Sönnichsen, C., Mapping the Polarization Pattern of Plasmon Modes Reveals Nanoparticle Symmetry. *Nano Lett.* **2008,** *8* (8), 2345-2350.

(38) Wei, H.; Reyes-Coronado, A.; Nordlander, P.; Aizpurua, J.; Xu, H., Multipolar Plasmon Resonances in Individual Ag Nanorice. *ACS Nano* **2010,** *4* (5), 2649-2654.

(39) Tcherniak, A.; Ha, J.; Dominguez-Medina, S.; Slaughter, L.; Link, S., Probing a Century Old Prediction One Plasmonic Particle at a Time. *Nano Lett.* **2010,** *10* (4), 1398-1404.

(40) Ringe, E.; Langille, M. R.; Sohn, K.; Zhang, J.; Huang, J.; Mirkin, C. A.; Van Duyne, R. P.; Marks, L. D., Plasmon Length: A Universal Parameter to Describe Size Effects in Gold Nanoparticles. *The Journal of Physical Chemistry Letters* **2012,** *3* (11), 1479-1483.

(41) Wiley, B. J.; Chen, Y.; McLellan, J. M.; Xiong, Y.; Li, Z.-Y.; Ginger, D.; Xia, Y., Synthesis and Optical Properties of Silver Nanobars and Nanorice. *Nano Lett.* **2007,** *7* (4), 1032-1036.

(42) Ringe, E.; Zhang, J.; Langille, M. R.; Mirkin, C. A.; Marks, L. D.; Van Duyne, R. P., Correlating the Structure and Localized Surface Plasmon Resonance of Single Silver Right Bipyramids. *Nanotechnology* **2012,** *23* (44), 444005-444005.

(43) Zhang, S.; Bao, K.; Halas, N. J.; Xu, H.; Nordlander, P., Substrate-Induced Fano Resonances of a Plasmonic: Nanocube: A Route to Increased-Sensitivity Localized Surface Plasmon Resonance Sensors Revealed. *Nano Lett.* **2011,** *11* (4), 1657-1663.

(44) Mock, J. J.; Smith, D. R.; Schultz, S., Local Refractive Index Dependence of Plasmon Resonance Spectra from Individual Nanoparticles. *Nano Lett.* **2003,** *3* (4), 485-491.

(45) Liz-Marzán, L. M., Tailoring Surface Plasmons through the Morphology and Assembly of Metal Nanoparticles. *Langmuir* **2006,** *22* (1), 32-41.

(46) Sherry, L. J.; Jin, R.; Mirkin, C. A.; Schatz, G. C.; Van Duyne, R. P., Localized Surface Plasmon Resonance Spectroscopy of Single Silver Triangular Nanoprisms. *Nano Lett.* **2006,** *6* (9), 2060-2065.

(47) Nellist, P.; Pennycook, S., Subangstrom Resolution by Underfocused Incoherent Transmission Electron Microscopy. *Phys. Rev. Lett.* **1998,** *81* (19), 4156-4159.

(48) Suenaga, K.; Sato, Y.; Liu, Z.; Kataura, H.; Okazaki, T.; Kimoto, K.; Sawada, H.; Sasaki, T.; Omoto, K.; Tomita, T., Visualizing and Identifying Single Atoms Using Electron Energy-Loss Spectroscopy with Low Accelerating Voltage. *Nature chemistry* **2009,** *1* (5), 415-418.

(49) Nelayah, J.; Kociak, M.; Stephan, O.; de Abajo, F. J. G.; Tence, M.; Henrard, L.; Taverna, D.; Pastoriza-Santos, I.; Liz-Marzan, L. M.; Colliex, C., Mapping Surface Plasmons on a Single Metallic Nanoparticle. *Nat. Phys.* **2007,** *3* (5), 348-353.

(50) Chu, M. W.; Myroshnychenko, V.; Chen, C. H.; Deng, J. P.; Mou, C. Y.; de Abajo, F. J. G., Probing Bright and Dark Surface-Plasmon Modes in Individual and Coupled Noble Metal Nanoparticles Using an Electron Beam. *Nano Lett.* **2009,** *9* (1), 399-404.

(51) N'Gom, M.; Li, S. Z.; Schatz, G.; Erni, R.; Agarwal, A.; Kotov, N.; Norris, T. B., Electron-Beam Mapping of Plasmon Resonances in Electromagnetically Interacting Gold Nanorods. *Phys. Rev. B* **2009,** *80* (11).

(52) N'Gom, M.; Ringnalda, J.; Mansfield, J. F.; Agarwal, A.; Kotov, N.; Zaluzec, N. J.; Norris, T. B., Single Particle Plasmon Spectroscopy of Silver Nanowires and Gold Nanorods. *Nano Lett.* **2008,** *8* (10), 3200-3204.

(53) Nelayah, J.; Gu, J.; Sigle, W.; Koch, C. T.; Pastoriza-Santos, I.; Liz-Marzan, L. M.; van Aken, P. A., Direct Imaging of Surface Plasmon Resonances on Single Triangular Silver Nanoprisms at Optical Wavelength Using Low-Loss Eftem Imaging. *Opt. Lett.* **2009,** *34* (7), 1003-1005.

(54) Schaffer, B.; Hohenester, U.; Trügler, A.; Hofer, F., High-Resolution Surface Plasmon Imaging of Gold Nanoparticles by Energy-Filtered Transmission Electron Microscopy. *Phys. Rev. B* **2009,** *79* (4).

(55) Alonso-Gonzalez, P.; Schnell, M.; Sarriugarte, P.; Sobhani, H.; Wu, C.; Arju, N.; Khanikaev, A.; Golmar, F.; Albella, P.; Arzubiaga, L.; Casanova, F.; Hueso, L. E.; Nordlander, P.; Shvets, G.; Hillenbrand, R., Real-Space Mapping of Fano Interference in Plasmonic Metamolecules. *Nano Lett.* **2011,** *11* (9), 3922-3926.

(56) Fang, Z.; Cai, J.; Yan, Z.; Nordlander, P.; Halas, N. J.; Zhu, X., Removing a Wedge from a Metallic Nanodisk Reveals a Fano Resonance. *Nano Lett.* **2011,** *11* (10), 4475-4479.

(57) Ye, J.; Wen, F.; Sobhani, H.; Lassiter, J. B.; Van Dorpe, P.; Nordlander, P.; Halas, N. J., Plasmonic Nanoclusters: Near Field Properties of the Fano Resonance Interrogated with Sers. *Nano Lett.* **2012,** *12* (3), 1660-1667.

(58) Hao, F.; Sonnefraud, Y.; Van Dorpe, P.; Maier, S. A.; Halas, N. J.; Nordlander, P., Symmetry Breaking in Plasmonic Nanocavities: Subradiant Lspr Sensing and a Tunable Fano Resonance. *Nano Lett.* **2008,** *8* (11), 3983-3988.

(59) Verellen, N.; Sonnefraud, Y.; Sobhani, H.; Hao, F.; Moshchalkov, V. V.; Van Dorpe, P.; Nordlander, P.; Maier, S. A., Fano Resonances in Individual Coherent Plasmonic Nanocavities. *Nano Lett.* **2009,** *9* (4), 1663-1667.

(60) Edwards, P. R.; Sleith, D.; Wark, A. W.; Martin, R. W., Mapping Localized Surface Plasmons within Silver Nanocubes Using Cathodoluminescence Hyperspectral Imaging. *J. Phys. Chem. C* **2011,** *115* (29), 14031-14035.

(61) Lassiter, J. B.; Sobhani, H.; Knight, M. W.; Mielczarek, W. S.; Nordlander, P.; Halas, N. J., Designing and Deconstructing the Fano Lineshape in Plasmonic Nanoclusters. *Nano Lett.* **2012,** *12* (2), 1058-1062.

(62) Bigelow, N. W.; Vaschillo, A.; Camden, J. P.; Masiello, D. J., Signatures of Fano Interferences in the Electron Energy-Loss Spectroscopy and Cathodoluminescence of Symmetry-Broken Nanorod Dimers. *ACS Nano* **2013**.

(63) Guiton, B. S.; Iberi, V.; Li, S.; Leonard, D. N.; Parish, C. M.; Kotula, P. G.; Varela, M.; Schatz, G. C.; Pennycook, S. J.; Camden, J. P., Correlated Optical Measurements and Plasmon Mapping of Silver Nanorods. *Nano Lett.* **2011,** *11* (8), 3482-3488.

(64) Mirsaleh-Kohan, N.; Iberi, V.; Simmons, P. D.; Bigelow, N. W.; Vaschillo, A.; Rowland, M. M.; Best, M. D.; Pennycook, S. J.; Masiello, D. J.; Guiton, B. S., et al., Single-Molecule Surface-Enhanced Raman Scattering: Can Stem/Eels Image Electromagnetic Hot Spots? *J. Phys. Chem. Lett.* **2012,** *3* (16), 2303-2309.

(65) McMahon, J. M.; Wang, Y.; Sherry, L. J.; Van Duyne, R. P.; Marks, L. D.; Gray, S. K.; Schatz, G. C., Correlating the Structure, Optical Spectra, and Electrodynamics of Single Silver Nanocubes. *J. Phys. Chem. C* **2009,** *113* (7), 2731-2735.

(66) Rycenga, M.; Xia, X.; Moran, C. H.; Zhou, F.; Qin, D.; Li, Z.-Y.; Xia, Y., Generation of Hot Spots with Silver Nanocubes for Single-Molecule Detection by Surface-Enhanced Raman Scattering. *Angewandte Chemie International Edition* **2011,** *50* (24), 5473-5477.

(67) Kim, D.-S.; Heo, J.; Ahn, S.-H.; Han, S. W.; Yun, W. S.; Kim, Z. H., Real-Space Mapping of the Strongly Coupled Plasmons of Nanoparticle Dimers. *Nano Lett.* **2009,** *9* (10), 3619-3625.

(68) Guo, S. J.; Li, J.; Dong, S. J.; Wang, E. K., Three-Dimensional Pt-on-Au Bimetallic Dendritic Nanoparticle: One-Step, High-Yield Synthesis and Its Bifunctional Plasmonic and Catalytic Properties. *J. Phys. Chem. C* **2010,** *114* (36), 15337-15342.

(69) Keenan, M. R., Exploiting Spatial-Domain Simplicity in Spectral Image Analysis. *Surface and Interface Analysis* **2009,** *41* (2), 79-87.

(70) Purcell, E. M.; Pennypac.Cr, Scattering and Absorption of Light by Nonspherical Dielectric Grains. *Astrophysical Journal* **1973,** *186* (2), 705-714.

(71) Draine, B. T.; Flatau, P. J., Discrete-Dipole Approximation for Scattering Calculations. *J. Opt. Soc. Am. A:* **1994,** *11* (4), 1491-1499.

(72) Bigelow, N. W.; Vaschillo, A.; Iberi, V.; Camden, J. P.; Masiello, D. J., Characterization of the Electron- and Photon-Driven Plasmonic Excitations of Metal Nanorods. *ACS Nano* **2012,** *6* (8), 7497-7504.

(73) Masiello, D. J. http://faculty.washington.edu/masiello/Masiello_Group_Website/e-DDA.html.

(74) Bogner, A.; Jouneau, P. H.; Thollet, G.; Basset, D.; Gauthier, C., A History of Scanning Electron Microscopy Developments: Towards "Wet-Stem" Imaging. *Micron* **2007,** *38* (4), 390-401.

(75) Krivanek, O. L.; Ursin, J. P.; Bacon, N. J.; Corbin, G. J.; Dellby, N.; Hrncirik, P.; Murfitt, M. F.; Own, C. S.; Szilagyi, Z. S., High-Energy-Resolution Monochromator for

Aberration-Corrected Scanning Transmission Electron Microscopy/Electron Energy-Loss Spectroscopy. *Philos. Trans. R. Soc. A-Math. Phys. Eng. Sci.* **2009,** *367* (1903), 3683-3697.

(76) Nicoletti, O.; de la Pena, F.; Leary, R. K.; Holland, D. J.; Ducati, C.; Midgley, P. A., Three-Dimensional Imaging of Localized Surface Plasmon Resonances of Metal Nanoparticles. *Nature* **2013,** *502* (7469), 80-+.

(77) Mazzucco, S.; Geuquet, N.; Ye, J.; Stéphan, O.; Van Roy, W.; Van Dorpe, P.; Henrard, L.; Kociak, M., Ultralocal Modification of Surface Plasmons Properties in Silver Nanocubes. *Nano Lett.* **2012**, 1288-1294.

(78) Iberi, V.; Mirsaleh-Kohan, N.; Camden, J. P., Understanding Plasmonic Properties in Metallic Nanostructures by Correlating Photonic and Electronic Excitations. *J. Phys. Chem. Lett.* **2013,** *4* (7), 1070-1078.

CONCLUSION

Correlated optical spectroscopy when combined with STEM/EELS and theoretical simulations, provide a means of understanding the fundamental connection between electron- and photon-driven plasmonic processes. The progress that has been made in understanding this fundamental connection in metallic nanostructures at the single-particle level has been demonstrated. Furthermore, the application of STEM/EELS to single-molecule SERS in order to fully explore the nature of electromagnetic hot spots has been investigated. The extraordinary ability of STEM/EELS to characterize plasmon resonances with the appropriate spatial and energy resolution, and its complementarity to all-optical techniques, suggests it will play an essential role in fundamental and applied studies of plasmonics going forward.

VITA

Vighter Ozezinimize Iberi was born in Lagos, Nigeria. He moved to the United States of America in 2005 and graduated with a B.S. degree from Campbellsville University in 2008. In the fall of 2009, he began his graduate studies in Physical Chemistry at the University of Tennessee Knoxville under the tutelage of Prof. Jon Camden. His research focused on understanding plasmonics in metallic nanostructures with a combination of dark-field optical microscopy and electron microscopy.